Imperial College London
Department of Earth Science and Engineering

Geostatistical Facies Modelling of Cyclicity and Rhythmicity in Shallow-Marine Reservoirs

Thomas Le Blévec

Submitted in part fulfilment of the requirements for the degree of
Doctor of Philosophy in Geostatistics of Imperial College, London June 2018

Abstract

This work presents a new geostatistical approach aimed at incorporating more accurate geological input into existing Earth modelling tools. These tools play a key role in petroleum reservoir and mining deposit modelling workflows as they are the basis for the estimation of resource recovery and its associated uncertainty. Conventional geostatistics generate facies successions that are statistically identical along one direction or its opposite. This impedes the modelling of facies ordering, also called facies cyclicity, which is often characterized in shallow-marine carbonate and siliciclastic reservoirs by shallowing upward facies cycles. Cyclicity is often coupled with another geological characteristic of sedimentary sequences, which is that facies usually appear repeatedly at almost constant stratigraphic intervals, a feature called facies rhythmicity. The principal result of this thesis is a new method that can quantify and simultaneously model facies cyclicity and rhythmicity. Cyclicity is quantified using transition probability analysis, while rhythmicity is quantified using two point statistical tools such as transiograms. The new method is an extension of the approach known as Pluri-Gaussian Simulations, which is significantly improved by developing new periodic covariances and a co-regionalization model with spatial asymmetry. The method was tested on case studies of shallow marine deposits such as the Latemar carbonate platform in Italy and the Blackhawk Formation siliciclastic shoreface deposits in the Book Cliffs, USA. The choice of case studies was dictated by the desire to model a range of geological patterns including different styles of diagenesis, the presence of erosional surfaces, and non-stationarity. This was also an opportunity to evaluate the method in relation with established geological concepts such as sequence stratigraphy or Walther's Law. By generating more realistic three-dimensional geological Earth models, the method has the potential to significantly improve the quality of hydrocarbon and mining resource estimates and the quantification of their associated uncertainty.

Copyright Declaration

Acknowledgements

I would like to express my deepest gratitude to:

- My main supervisor Olivier Dubrule, for his work, constant involvement in the project and support for the past three years. My two supervisors Gary Hampson and Cédric M. John for their major contribution to the project. The Department of Earth Science and Engineering of Imperial College for providing the scholarship.

- Jacques Rivoirard and Howard Johnson for examining this thesis. Peter King for assessing the project milestones. Guillaume Caumon, Alexandre Boucher and Hervé Gross for introducing me to geostatistics. Claire Veillard, Carl Jacquemyn and Lukas Mosser for contributing ideas to this project.

- My dear flatmates Alexander Ogilvie-Graham, Saoirse Herbert, Jessica Verschoyle for brightening up my life and of course Tinamay Ogilvie-Graham who made all this possible. My close friend Clément Joulin for this wonderful experience we shared together, my spiritual teachers Karuna and Nitima Priya for their psychological guidance and loving-kindness, and Jeff Franklin for believing in me. Last but not least all my family for their unconditional love.

Dedication

I dedicate this thesis to my parents Geneviève and Dominique,

‘It is better to be kind than right.’

Sridhar Rana Rinpoche

Contents

List of Tables

List of Figures

Chapter 1

Introduction

1.1 Motivation and Objectives

The exploitation of subsurface resources such as hydrocarbons, mineral deposits or aquifers requires digital Earth models on which the production process can be simulated, allowing prediction of the resource recovery and associated uncertainties. In the petroleum industry, geologists and engineers have usually at their disposal only sparse or low resolution data, such as well and seismic data. It is thus necessary to develop tools able to create three-dimensional Earth models from wells or geological sections. This is possible with geostatistics, which can be used to simulate realisations of subsurface properties in three dimensions from such datasets (Chiles and Delfiner, 2012). More specifically, indicator geostatistics focus on discrete properties such as geological facies or petrophysical rock-types, and can be used to build Earth models of the subsurface representing possible facies architectures (Pyrcz and Deutsch, 2014).

Earth facies models should incorporate accurate geological concepts in order to be predictive. This is a challenging task, because reservoirs can be very heterogeneous. Carbonate reservoirs often present more complexity than siliciclastic reservoirs, because their formation is controlled by complex biological and chemical processes, in addition to physical processes and prevalence of diagenetic overprinting (Tucker and Wright, 2009). It is thus important to understand the main patterns observed in carbonate facies successions in order to propose an appropriate

geostatistical method.

Two stratigraphic features are often associated with carbonate successions: facies cyclicity and rhythmicity (both of which can also be observed in siliciclastic reservoirs). Cyclicity is an ordering of facies (Wilkinson et al., 1997; Burgess, 2016), which is often characterized by shallowing upward facies cycles (Strasser, 1988; Goldhammer et al., 1990; Lindsay et al., 2006). Rhythmicity is the observation of rhythms in the geological record (De Boer and Wonders, 1984; House, 1985), so that facies appear repeatedly at stratigraphic intervals of similar thicknesses.

Another characteristic of most carbonate successions is diagenesis. Diagenesis corresponds to the different transformations that the rock undergoes after deposition (Bathurst, 1972), and is key for predicting reservoir quality, because it can considerably modify petrophysical properties (e.g., Bartok et al., 1981; Moore, 2001). Diagenesis is extensive in carbonates and is spatially distributed in very diverse styles. It can be either conformable to depositional facies (e.g., Ginsburg, 1957; Egenhoff et al., 1999; Peterhänsel and Egenhoff, 2008; Rameil, 2008), or it can cut across depositional facies along fractures, faults, and karsts (e.g., Sharp et al., 2010; Vandeginste et al., 2013; Jacquemyn et al., 2014; Beckert et al., 2015). This variety of patterns should also be reproduced by the geostatistical methods.

It seems, however, that geostatistical methods have difficulty reproducing the geological patterns mentioned above. Although the two concepts of facies cyclicity and rhythmicity are key in geology, they are not part of the vocabulary of geostatisticians. For example, the indicator variogram is a geostatistical tool widely used in Earth modelling software (Pyrcz and Deutsch, 2014) but a variogram computed in a vertical facies succession would be the same in the upward direction as in the downward direction (Carle and Fogg, 1996). Therefore, variograms cannot quantify cyclicity, which is a facies ordering in a specific direction. Other geostatistical methods such as object-based methods (Deutsch and Tran, 2002), or Multi-Point Statistics (Strebelle, 2002) have not yet been specifically applied to the modelling of cyclic facies successions.

However some methods seem able to model facies cyclicity. Although Carle and Fogg (1996) did not explicitly mention the word cyclicity, their method based on Markov Chains uses transiograms, which are asymmetric. In their basic version, Pluri-Gaussian Simulations (PGS)

are not able to model facies asymmetry (Armstrong et al., 2011), although some studies suggest they can be modified to do so (e.g., Langlais et al., 2008). PGS and transiogram-based methods could therefore provide a good starting point for modelling facies cyclicity.

Rhythmicity is known to be related to variograms with hole-effects (pseudo-oscillations) (Ma and Jones, 2001), but the exact relation between the two is not explicit, and existing geostatistical methods have trouble reproducing hole-effects for indicator variables (Dubrule, 2017). New indicator variogram models should thus be built to render rhythmicity.

Most geostatistical methods focus more on modelling of depositional facies than on modelling of diagenetic effects and this is an obvious limitation in the case of carbonate reservoirs. The method of Renard et al. (2008), based on PGS, is the only one that stands out as seeming well-suited to represent diagenesis. However, the method is not implemented in the context of depositional facies cyclicity and rhythmicity.

The difficulty of modelling cyclicity, rhythmicity and diagenesis may be explained by the fact that most geostatistical methods have been mainly designed for modelling siliciclastic reservoirs and have been applied to model carbonates to a lesser extent. See for instance the number of methods developed for modelling channel deposits (Strebelle, 2002; Deutsch and Tran, 2002), which are characteristic of siliciclastic reservoirs, but much less prominent in carbonates (Tucker and Wright, 2009). Even Carle and Fogg (1996) who pioneered the use of transiograms, applied their method to siliciclastic deposits. By contrast, many applications of PGS are found in carbonate deposits (e.g., Galli et al., 2006; Armstrong et al., 2011; Doligez et al., 2011; Hamon et al., 2016).

This thesis is thus concerned with developing a novel geostatistical method that can account for the geological heterogeneities listed above. More precisely, I will here investigate whether facies cyclicity and rhythmicity can be modelled together with diagenesis, by improving one of the existing mainstream geostatistical methods. The flexibility of PGS makes it a good candidate for modelling carbonate deposits, but further analysis of the geostatistical literature is necessary to understand whether other methods would be suitable alternatives.

1.2 Contributions

The papers published during the PhD are under the names of myself, Thomas Le Blévec, and my supervisors, Olivier Dubrule, Cédric M. John and Gary Hampson. Being the first author, I have done all the research, which includes mathematical developments, the implementation of such developments in the coding language R (the main part of the code has been published at `https://github.com/tleblevecIMP`), and their application to case studies. I had weekly meetings with my supervisors, who provided me with guidance and ideas on the project. I also had more frequent exchanges with my main supervisor Olivier Dubrule. The papers were first written by myself, and then proofread by the supervisors in order to improve the content, structure, clarity and language.

Three peer-reviewed papers have been submitted respectively to the book Geostatistics Valencia 2016 (Le Blévec et al., 2017b, Chapter 4 of this thesis), to the journal Mathematical Geosciences (Le Blévec et al., 2018, Chapter 5 of this thesis), and to the journal American Association of Petroleum Geologists (AAPG) Bulletin (Le Blévec et al., in review, Chapter 6 of this thesis). The first two of these papers have now been published. I also attended conferences at which aspects of my work were presented: Geostats Valencia 2016, EAGE Paris 2017, les Journées de la Géostatistique 2017, AAPG London 2017, EAGE Copenhagen 2018 and IAMG 2018. At each of these conferences, I gave a presentation of my latest results.

1.3 Statement of Originality

The work contained in this thesis has not been previously submitted for a degree or diploma at any other higher education institution. To the best of my knowledge and belief, the thesis contains no material previously published or written by another person except where due references are made.

1.4 Thesis Outline

The main chapters of this thesis are published papers, and are not modified from the published versions. This structure creates some repetition in the text as aspects of the method are explained several times, with minor differences in the nomenclature between chapters. These repetitions can be useful as reminders for the reader, and are noteworthy in their own right as the papers were adapted to different audiences. For instance the Valencia and Mathematical Geosciences papers were targeted towards geostatisticians, whilst the AAPG Bulletin paper was targeted towards geologists. The different chapters also present a gradual progression, because each new paper is an extension of the method.

In chapter 2, I provide a literature review presenting how geostatistical tools have been applied in the past to carbonate reservoirs. Chapter 3 presents an outline of the research conducted during the PhD study in more detail. Chapter 4 (Le Blévec et al., 2017b) provides a novel method based on PGS to model facies asymmetry in the vertical direction. Chapter 5 (Le Blévec et al., 2018) extends the method to jointly model facies cyclicity and facies rhythmicity in three dimensions. Chapter 6 (Le Blévec et al., in review) extends the method to model diagenesis using novel three dimensional truncation rules. Then, a general discussion of the proposed method is provided in Chapter 7. Chapter 8 presents the overall conclusions of the PhD thesis.

Chapter 2

Geostatistical Facies Modelling of Carbonates, a Review

2.1 Introduction

Although geostatistics has provided sophisticated tools to model shallow-marine reservoirs (Pyrcz and Deutsch, 2014), most of these tools were designed and applied to siliciclastic deposits rather than carbonates (e.g., Deutsch and Tran, 2002; Strebelle, 2002). However, carbonates differ from siliciclastic deposits in their grain types, aspects of depositional configuration, and their diagenetic potential. It is estimated that more than 60 percent of the world's oil and 40 percent of the world's gas reserves are held in carbonate reservoirs (Schlumberger, 2018), which means that geostatistical methods should be adapted to model them. Contrary to siliciclastics, carbonates are formed in situ by living organisms and their spatial distribution is thus controlled by external parameters (light, temperature, environmental conditions) as well as by the extent to which sediments are reworked by physical processes (e.g. waves, tides) (Tucker and Wright, 2009). Therefore, grain sizes and sediment textures in carbonates are not only controlled by the energy of the environment, which adds additional complexity compared to siliciclastic facies architectures. In addition, geometries are more varied in carbonates due to early cementation and the ability of reef builders to create build-ups (Wilson, 2012). Calcium

carbonate is chemically more reactive than silica, and therefore diagenesis is more extensive in carbonates (Moore, 2001). Finally, the nature of carbonate deposits changes through geological time (Wilson, 2012). For these reasons, it is harder to apply current facies geostatistical methods to model carbonates.

There are two basic approaches in geostatistical facies modelling. The first approach, called "object-based", models geobodies, for example channels in fluvial siliciclastic deposits (Deutsch and Tran, 2002; Ruiu et al., 2016; Parquer et al., 2017). This approach has been extended by Aigner et al. (2007) and Adams et al. (2005) to the modelling of carbonate geobodies such as shoals and reefs. In the case where the three-dimensional geometry of facies is poorly defined, it may be preferable to use a geostatistical approach that is less geometrically-constrained and focuses more on spatial correlations between facies occurrences at different locations (Carle and Fogg, 1996; Strebelle, 2002; Armstrong et al., 2011). This is the second category of approaches, also called "pixel-based" (this term is derived from the widespread practice of building geostatistical models on a grid composed of grid cells or "pixels", although that is not a requirement for the application of such methods in reservoir modelling), which can either be applied to a facies classification based on environments of deposition, or on petrophysical rock-types. Pixel-based methods may be preferred for carbonates, especially if the facies classification is complex and if, as frequently occurs, the geometry of the different facies is poorly constrained.

This literature review first investigates object-based methods (Deutsch and Tran, 2002) and then focuses on pixel-based methods. This part of the review starts with SIS (Alabert, 1989), which distributes facies independently from each other. Then, the review considers pixel-based methods that are able to reproduce inter-facies relationships: cross-variograms modelled with co-SIS (but no applications to carbonates are found in the literature), transiogram-based (Carle and Fogg, 1996), Pluri-Gaussian Simulations (Armstrong et al., 2011) and Multi-Point Statistics (Strebelle, 2002). Several previously published case studies are discussed, focusing on the facies classification used, the modelling of non-stationarity, the nature of inputs and outputs, and the advantages and limitations of each method. Then, I discuss how to improve these geostatistical methods for modelling carbonates.

2.2 Object-Based Approach

Introduction

Object-based stochastic approaches model individual facies as simple geometrical shapes controlled by randomly selected values of parameters defined by the geologist (Pyrcz and Deutsch, 2014). The probability density functions (pdfs) of key geometrical parameters are usually derived from analogues (usually seismic data or outcrops). Facies heterogeneities thus conform to the geologist's conceptual knowledge. However, most existing object-based methods do not quantify inter-facies relationships. Four case studies in which carbonate facies have been modelled with object-based methods are described below and summarised in Table 2.1.

Datasets

Qi et al. (2007) use ten cores from the St. Louis Limestone reservoir of Kansas (which has produced so far 300 million bbl from fields in the Hugoton embayment) to assess the distribution of oolitic deposits in Big Bow and Sand Arroyo Creek fields. Aigner et al. (2007) model an outcrop analogue of carbonate shoals in the Triassic Upper Muschelkalk, in Germany (Braun, 2003), which provides a cross-section covering an area of 30 x 10 km laterally and 15 m vertically, described by 21 logs. Adams et al. (2005) use outcrop data to construct a model with an area of 1.6 x 2.8 km laterally and 104 m vertically, of Proterozoic strata, Namibia, containing thrombolite-stromatolite reefs. Doligez et al. (2011) model an outcrop with an area of 2 x 2 km (thickness is not mentioned) in the Alveolina Formation, Early Eocene (Pyrenees).

Table 2.1: Different case studies of carbonate deposits modelled with object-based methods

Authors	Type	No. of facies	Geo-object
Qi et al. (2007)	Oolitic reservoir	6	Ellipses, baffles
Aigner et al. (2007)	Shoal outcrop analogue	3	Elliptic shoals
Adams et al. (2005)	Reefal outcrop analogue	3	Circular reefs
Doligez et al. (2011)	Silici-carbonate outcrop analogue	5	Channels

Facies Classification and Geo-objects

Outcrop studies are often used to derive facies geometries. For example, Adams et al. (2005) define thrombolite-stromatolite reef geometries as dome structures, measured on 2D outcrop cross-sections by width and height. They do not observe lateral anisotropy, so the reefs are assumed to be circular. Aigner et al. (2007) model shoal facies association, shoal transition facies association and offshoal (fore- and back-shoal) facies association, which are composed internally of 15 lithofacies (Braun, 2003), and they choose elliptical geometries to represent them based on previous mapping (Ruf and Aigner, 2004).

In case there are no available analogues or other sources of information on facies geometries, authors use simple shapes to represent geobodies. For example Qi et al. (2007) simulate oolitic complexes, tidal flats and eolianite deposits as elliptical objects defined by width, height, thickness and azimuth, based on published satellite images of modern depositional environments (Harris, 1994). Doligez et al. (2011) model channel deposits with their characteristic elongated shape.

Input Parameters

Input parameters of object-based methods are pdfs of the different geometrical parameters. Adams et al. (2005) fit the experimental distributions with splines which are then transformed into pdfs by normalizing them. Disappointingly, the other studies do not describe the pdf models constraining the geo-objects. They give nonetheless the parameters of the statistical distributions. For example, Qi et al. (2007) choose the facies geometrical parameters for the ooid shoals based on published satellite images of modern analogues (Harris, 1994), which have approximately a thickness of 1 m, length of 3 km and width of 2 km. Aigner et al. (2007) use outcrop mapping of the Muschelkalk by Ruf and Aigner (2004) to model the shoals with a width of 11-13 km, length of 14-18 km, and thickness of decimetre scale.

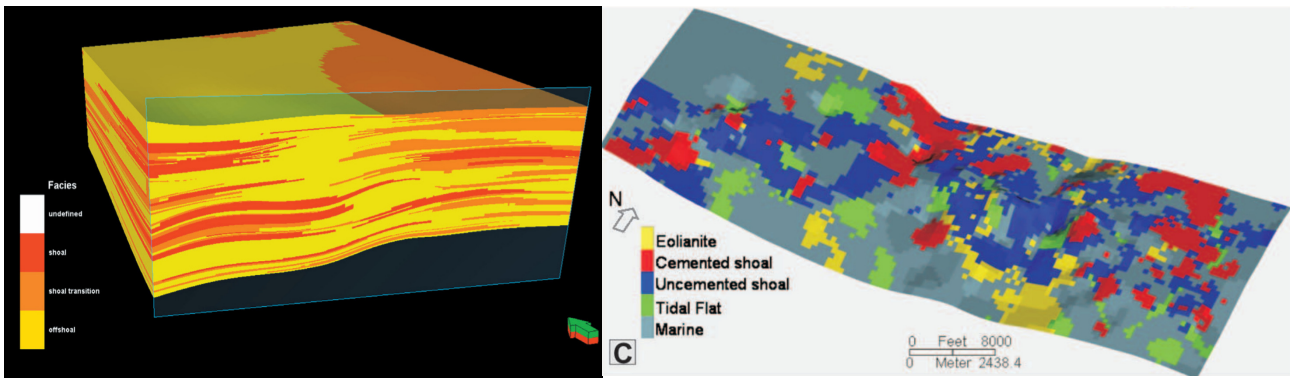

Figure 2.1: Two object-based realisations of carbonate environments, Aigner et al. (2007) in Upper Muschelkalk, Germany (left) and Qi et al. (2007) in St. Louis Limestone (right).

Simulation Result

Figure 2.1 displays two models simulated by object-based methods from Aigner et al. (2007) and Qi et al. (2007). One can observe the elliptical geometries of the shoals (Fig. 2.1, left) and of the eolianite, cemented shoals, uncemented shoals, and tidal flats (Fig. 2.1, right). In the different case studies, the realizations are inspected visually to assess the geological robustness of the modelling methods and input data, but there is no quantitative validation.

Discussion

Object-based methods are useful to represent geobodies with geometries that can be measured in modern analogues observed by satellite pictures (e.g., Harris, 1994) or outcrop pictures (Adams et al., 2005). Such information were used here for the modelling reefs (Adams et al., 2005) and tidal flats (Qi et al., 2007). It is noteworthy that the pictures are two-dimensional while the Earth models are three-dimensional, which requires an assumption for the facies shape in three dimensions. For example, Adams et al. (2005) do not have access to lateral information of reef geometries and assume a circular shape, which could be false.

If no simple geometries can be observed in analogues, then a simple and convenient geometry can be chosen (e.g., an ellipse, which defines the length of the geobodies in three principal directions). However, such simple and convenient geometries may be a wrong approximation. Object-based methods are thus limited if no information on geobody geometries are available.

This is likely to be the case if the facies classification is complex and contains a large number of facies.

Some authors (Aigner et al., 2007) record metre-scale vertical facies cycles that they do not reproduce in the Earth model. Object-based methods are not good at modelling spatial relationships and hence at representing cyclicity. In addition, object-based methods model geobodies randomly in space, or according to facies proportion curves, but they cannot fix intervals between facies and thus do not model rhythmicity.

2.3 Sequential Indicator Simulation (SIS)

Introduction

SIS was one of the first methods designed for facies modelling (Alabert, 1989) and it is still widely used in Earth modelling software. From vertical facies successions, the method derives experimental indicator variograms, from which variogram models are calibrated and simulated (Pyrcz and Deutsch, 2014), which ensures that facies properties such as proportions and thicknesses are accurately reproduced. An advantage of SIS is that each facies is modelled with one variogram model, which means that different facies can be modelled with different characteristics (thicknesses for example). However, facies relationships are lost as each facies is modelled independently from the others.

A variogram model is defined by its type (exponential or Gaussian, for example) and a scale parameter or scale factor (Chiles and Delfiner, 2012). Earth modellers also describe variograms with the range, which is the distance at the which the variogram reaches its sill (Chiles and Delfiner, 2012). If the variogram reaches its sill only asymptotically, the practical range is defined as the distance at which the variogram reaches 95 % of its sill. For an indicator variogram, the sill is related to the proportion of the corresponding facies. The facies variogram tangent at the origin is directly related to the mean facies length in the corresponding direction (Carle and Fogg, 1996). Variograms can also incorporate discontinuities at the origin, called

Table 2.2: Different case studies of carbonate deposits modelled with SIS

Authors	Type	No. of facies	Variogram models
Qi et al. (2007)	Oolitic reservoir	6	Stable
Koehrer et al. (2010)	Dolomitized outcrop analogue	11	Spherical
Lakzaie et al. (2009)	reservoir	4	?
Janson and Madriz (2012)	Mound outcrop analogue	2	?
Aigner et al. (2007)	Shoal outcrop analogue	3	Gaussian
Amour et al. (2012)	Ramp outcrop analogue	10	?

nugget effects, which quantify geological variations at a smaller scale than the data spacing. Nugget effects allow modellers to account for measurement errors at data location as they equal to the variance of the measurement error (Chiles and Delfiner, 2012).

Most variogram models representing continuous variables are not valid for modelling facies (Dubrule, 2017) because they are not associated with a random set (Emery, 2010). For example, a facies variogram should be concave at the origin (Matérn, 1986), which is not the case for the Gaussian variogram. In spite of this, such variogram models are still widely used in the literature (cubic and Gaussian variograms, for example) to generate facies Earth models with SIS as shown in the several case studies in carbonate environments reported in Table 2.2.

Datasets

The datasets used by Qi et al. (2007) and Aigner et al. (2007) are described in Section 2.2. Koehrer et al. (2010) combine four outcrops and two cores in the Upper Muschelkalk in Germany, to build an Earth model with an area of 25 x 15 km and thickness of 20 m. Lakzaie et al. (2009) model an Iranian gas reservoir with areal dimensions of 45 x 11 km with 6 wells at unknown locations with no further information. Janson and Madriz (2012) model an outcrop 4300 m long, 2430 m wide and 25 m thick, based on twenty one stratigraphic sections, containing Late Carboniferous algal mounds in the Sacramento Mountains, New Mexico, USA. Amour et al. (2012) model Jurassic ramp deposits exposed in the Amellago Canyon in the High Atlas Mountains, Morocco. The outcrop is 320 m long, 190 m wide and 20 m thick and exhibits

metre-scale facies and diagenetic heterogeneities.

Facies Classification

Two main types of facies classification have been applied in the case studies, based on either rock-types, or on environments of deposition. Koehrer et al. (2010) and Amour et al. (2012) model facies based on the Dunham classification (Dunham, 1962) and Lakzaie et al. (2009) classify the facies into good, fair and poor from their petrophysical properties, mainly determined by the degree of cementation. Qi et al. (2007) combine rock-types with depositional environments. On the other hand, Aigner et al. (2007) use SIS to directly model facies associations related to environments of deposition: shoal, shoal transition, and offshoal. In another study, Janson and Madriz (2012) model only two facies based on environments of deposition, the core and flanking debris of carbonate mounds.

SIS is sometimes also used in the context of a nested approach at different scales. Koehrer et al. (2010) first model five facies associations deterministically: limestones, dolomitic limestone, dolomite, marlstone, and dolomitic marlstone, which vary at the regional scale. Then, eleven facies are modelled within these facies associations such as bioturbated mudstone or massive amalgamated skeletal packstone, which vary at the scale of 100s m. This procedure allows modellers to represent in the same Earth model heterogeneities at different scales.

Input Parameters

As explained above, SIS uses individual facies variograms as inputs, which are characterized by a model type, a sill and scale factors in three main directions. There is a great variety of models used in the case studies (Table 2.2). Koehrer et al. (2010) use a spherical model, Qi et al. (2007) use a stable model, and Aigner et al. (2007) use a Gaussian model (Table. 2.2). The three other case studies do not mention which type of variogram model is used (Table. 2.2).

In order to derive the vertical range of the variogram, a fitting procedure is usually performed between the experimental variograms computed on the vertical facies successions and the vari-

ogram model. Here, none of the case studies give the details of the fitting procedure. Koehrer et al. (2010) derive the variogram lateral range from geological cross-sections (Braun, 2003), and the variogram lateral range varies from 10 m for amalgamated lime-packstones to 5000 m for microbially laminated dolo-mudstones. Similarly, Aigner et al. (2007) approximate that the shoals are 10-20 km wide from interpreted geological cross-sections and ensure that the variogram range is of the same order as that interpreted for the shoals. Sedimentary features are usually more heterogeneous vertically than laterally, resulting in a high lateral-to-vertical ratio in variogram range. The anisotropy ratio tends to be particularly high with carbonate deposits. For example, Koehrer et al. (2010) model a microbially laminated dolo-mudstone with a variogram that has a vertical range of 0.3 m and a lateral one of 5000 m. Most authors do not discuss anisotropy in the lateral plane except for one study, for which Lakzaie et al. (2009) construct a horizontal variogram map using acoustic impedance in seismic data. Authors also use nugget effects (Lakzaie et al., 2009; Koehrer et al., 2010) with a maximum value of 0.7 (Lakzaie et al., 2009).

Algorithm Detail and Additional Data

SIS is performed by using kriging, which is usually employed in the form of simple kriging (Qi et al., 2007). However, Qi et al. (2007) also use Bayesian kriging (Omre, 1987), which allows the Earth modeller to incorporate uncertainty in the variogram model. The other authors do not mention which type of kriging is used.

Additional constraints are also introduced to some of the case studies in the form of proportion curves (Qi et al., 2007; Lakzaie et al., 2009; Janson and Madriz, 2012; Amour et al., 2012), which are used to model the variation of facies proportions in space. This is important as many geological facies distributions are non-stationary. For instance, Qi et al. (2007) model oolitic complexes with the help of a 2D lateral trend and vertical proportion curves derived from well data.

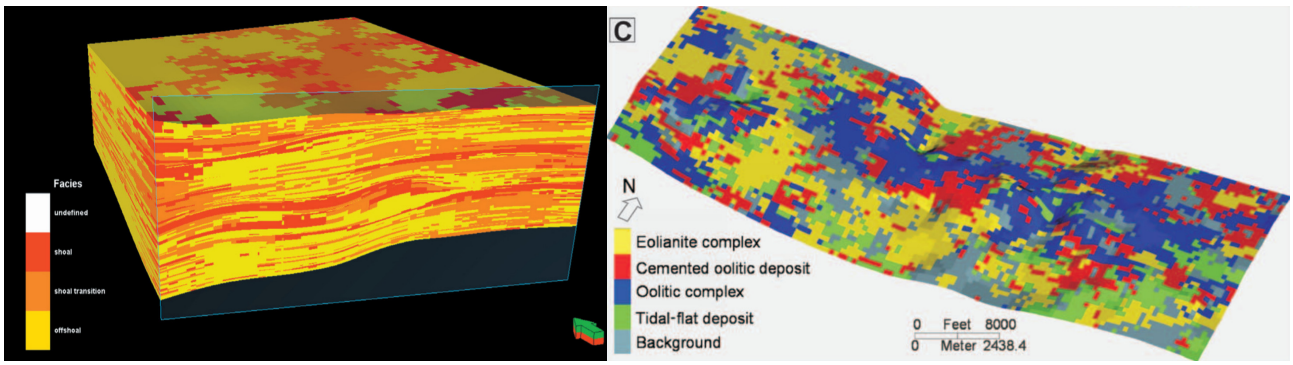

Figure 2.2: Two realizations of carbonate environments modelled with SIS, Aigner et al. (2007) in Upper Muschelkalk, Germany (left) and Qi et al. (2007) in St. Louis Limestone (right).

Simulation Results

Most authors neither provide much comment on the quality of their simulation results nor quality control the realisations. The realizations are inspected visually (Amour et al., 2012), and often identified qualitatively to be patchy (Koehrer et al., 2010) and not representative of the original connectivity of the geobodies (Qi et al., 2007). Qi et al. (2007) observe that using Bayesian kriging allows them to build facies models with more reasonable geometries, as reflected in higher facies connectivity, but this is not confirmed quantitavely. The only quantitative assessment was performed by Amour et al. (2012), who checked whether the facies proportion curves were accurately reproduced. Some realizations are shown in Fig. 2.2. Facies are indeed distributed with patchy geometries, and all facies are in contact with each other, a characteristic feature of SIS.

Discussion

SIS is often criticized by geologists because it does not reproduce pre-conceived facies geometries. However, this is not an issue when facies geometries are poorly defined such as for most facies classifications used here. Some authors also model environments of deposition such as mounds with SIS (Janson and Madriz, 2012). In their case, the overall geometries of the mounds are controlled by a surface modelled with a random Gaussian function, and the facies within the geometries are modelled with SIS and proportion curves. It is thus interesting to see that some of the potential problems in using SIS may be addressed by combining SIS with other

geostatistical methods. This is also the case for Koehrer et al. (2010), who model facies within environment of depositions.

Another issue with modelling environments of deposition is that SIS is not able to model spatial relationships between facies. In the case of Janson and Madriz (2012), this is not an issue because there are only two facies. For Aigner et al. (2007), who model shoals, shoal transitions and offshoals, the three facies associations are in contact in the interpreted cross-sections, which is compatible with SIS. However, it may be possible to perform more quantification of the inter-facies relationships and to use a more sophisticated method to model them. For example, Koehrer et al. (2010) observe facies cycles of about 0.2-5 m thickness, some of which are shallowing upward (massive bioturbated mudstones to oolitic grainstones), but they were unable to model these facies cycles with SIS.

Some misuses of SIS parameters are also noted in the different case studies. For example, Aigner et al. (2007) use a Gaussian variogram model, which is known to be invalid for facies variables (Matheron, 1989; Armstrong, 1992; Dubrule, 2017). Another example is the nugget effect of 0.7 defined by Lakzaie et al. (2009). As they do not explain how they chose this value, it is hard to assess its practical feasibility, but theoretically the maximum value for a nugget effect on an indicator variogram is 0.25 (if the facies proportion is 0.5, and less otherwise). Thus, a nugget effect of 0.7 amounts to assuming a pure nugget effect (facies extents are smaller than the grid cell). There is also a tendency to derive the variogram range from the expected size of the geobody (Aigner et al., 2007), although such a relation is false (Carle and Fogg, 1996) as mentioned earlier. It is rather the tangent at the origin of the variogram, which defines the mean length of facies in the corresponding direction (Carle and Fogg, 1996). These misuses reflect the frequent gap of understanding existing between geology and geostatistics.

Most case studies do not show the match between experimental variogram and variogram model. Therefore, the reader cannot check whether the facies Earth model is representative of the vertical facies successions. This is a significant shortcoming. Moreover, showing experimental variograms derived from vertical successions in carbonate successions would help to understand which variogram models are most suitable for modelling carbonates. For example, it is known

that hole-effects can be observed in facies variograms (Ma and Jones, 2001), which might have been appropriate for one or more of the case studies.

2.4 Building Co-Regionalization Models With Transiograms

Introduction

In order to model spatial relationships between facies, it seems natural to use cross-covariances or cross-variograms between facies. The cross-covariances or cross-variograms can be reproduced in an Earth model by using a generalization of SIS, called co-SIS, which uses co-kriging (Pyrcz and Deutsch, 2014). The challenge is to find valid indicator cross-variograms or cross-covariances for the simulation. For continuous variables, a co-regionalization model based on auto- and cross-covariances between the variables is valid only if it is positive semidefinite (Chiles and Delfiner, 2012). However, for indicator variables, or facies, there is no sufficient and necessary known condition for the indicator covariances to be valid (Dubrule, 2017). For this reason, it is not easy to build valid facies Earth models directly from two-point statistics such as variograms.

Carle and Fogg (1996) use Markov Chain theory to build valid co-regionalization models based on a new tool, the transiogram. Markov chains have been used for many decades in geology as a quantitative tool to test whether interpreted facies cyclicity is statistically valid (Gingerich, 1969; Hattori, 1976; Wilkinson et al., 1997; Burgess, 2016), but also in geophysics, for lithology and fluid predictions (e.g., Larsen et al., 2006). The transiogram is the generalization of transition probabilities for any continuous distance, and is equivalent to an indicator covariance divided by a facies proportion. More precisely, it is the probability that a facies B is present at a vector h from a given facies A. By using the Markovian assumption, Carle and Fogg (1996) are able to build valid auto- and cross-transiogram models in one dimension, which are then interpolated in three dimensions. Their method has the advantage of being able to model asymmetry, because the transiogram is different in upward and downward directions. However, the Markovian assumption limits the possible transiogram models (Dubrule, 2017).

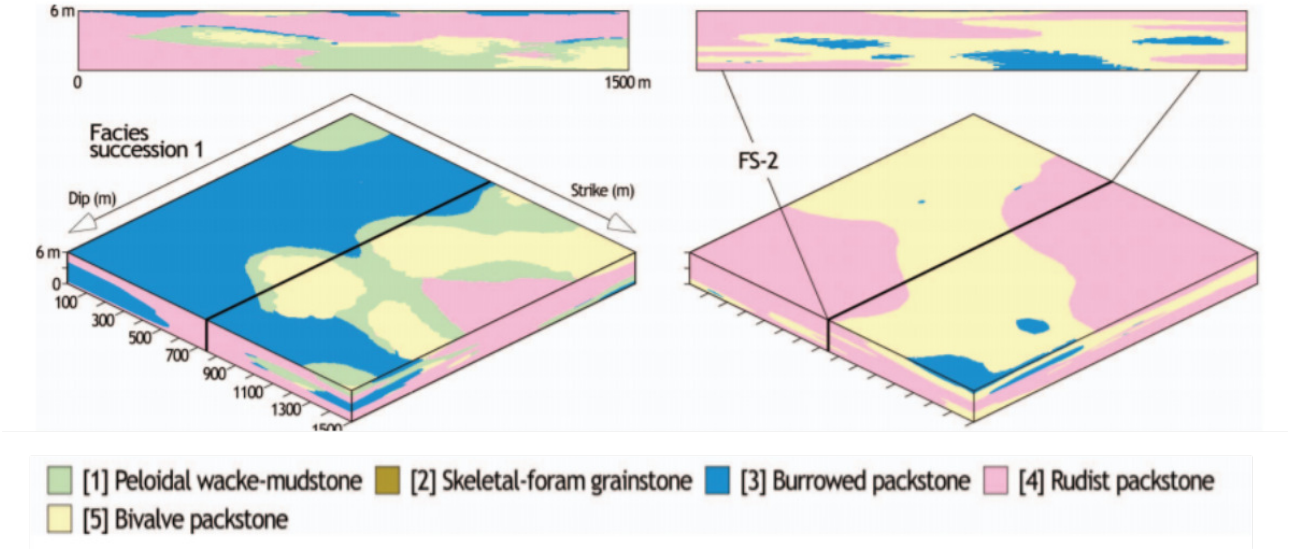

Figure 2.3: Two regions of the Lewis Canyon dataset modelled with Markov Chains transiograms (Purkis et al., 2012) with corresponding cross-sections.

The simulation of the Earth model is then performed by using co-SIS and simulated quenching (Carle and Fogg, 1996), or other methods are used, such as simulated annealing (Parks et al., 2000). The only case study of this method published for carbonate environments is provided by Purkis et al. (2012).

Case Study

Purkis et al. (2012) model the Lewis Canyon (Texas), which is a carbonate ramp intra-shelf basin system of the Upper Cretaceous containing rudist reef buildups, studied using a cross section of 30 m thick and of area approximately 1 x 1 km. Eleven facies based on the Dunham classification are described and then grouped into five facies associations for the modelling: mudstone, grainstone, burrowed packstone, rudist packstone and bivalve packstone. The reservoir is divided into 5 zones that are modelled independently, because of their different characteristics. Facies asymmetry is not observed in the facies successions within each zone, and no hole-effect is observed in the experimental transiograms, which can be accurately fitted by the transiogram model. Visually, the outcrop and the simulation results show tabular facies beds, as shown by Fig 2.3. The quality of the simulation is checked by picking random vertical successions and testing that they honour the input statistics.

Discussion

There is only one published case study of transiogram-based simulations in carbonate deposits. The case study shows that the method is able to accurately reproduce the facies auto- and cross-transiograms. In this case study, no facies asymmetry was observed, but the method is capable of successfully modelling carbonate reservoirs that contain such asymmetry as shown by Carle and Fogg (1996) on an alluvial fan siliciclastic example. This suggests that this method is appropriate to model carbonates.

However, transiogram models derived from Markov Chains have two major disadvantages, the first being that transition rates between facies in the lateral and vertical directions are statistically equivalent (Purkis et al., 2012). This means that facies tend to have the same transitions in the lateral and vertical directions. Such Markov Chains transiogram Earth models are not strictly Waltherian, because the simulation also incorporates statistical noise, which means that in the corresponding realisations, a facies occurrence can transition to a different facies in the vertical and lateral direction. This allows Earth modellers to account for erosional features between facies. However, it means that averaging transition probabilities between facies over a realization would lead to similar values in the lateral and vertical directions. Such three-dimensional Markov Chains transiogram models are thus said to honour Walther's law in a loose way (Doveton, 1994; Purkis et al., 2012). For this reason, Purkis et al. (2012) verify that lateral and vertical transition rates are statistically similar in the outcrop before simulating the Earth model with three dimensional Markov Chains. However, in some carbonate contexts, and depending on the volume of rock sampled, authors have observed that facies transitions are statistically not similar laterally and vertically (e.g., Hönig and John, 2015), such that even a loose Walther's law would not be valid. For instance, the transition between two facies might be possible laterally but not vertically, which cannot be modelled with this method.

The second disadvantage of Markov Chains transiogram models is that they cannot properly represent hole-effects (Dubrule, 2017). Although this does not seem to be a problem for the case study of Purkis et al. (2012) because the experimental transiograms do not show hole-effects, it is expected to be a problem in carbonate reservoirs where rhythmicity is present, as explained

by Jones and Ma (2001).

2.5 Pluri-Gaussian Approach

Introduction

Pluri-Gaussian Simulations (PGS) simulate facies by truncating Gaussian random functions. The method is derived from Truncated Gaussian Simulations (TGS) (Armstrong et al., 2011), which use only one Gaussian random function while PGS use several Gaussian random functions. The truncation rule applied to the Gaussian random functions directly controls the proportions of facies and contacts between facies. The truncation rule, together with the latent variograms, control the geometries of the facies. Therefore, PGS can represent both facies geometries and spatial relationships between facies.

An improvement of the method, called bi-PGS, has been proposed specifically for modelling diagenesis (Renard et al., 2008). It jointly simulates two facies fields, representing respectively depositional and diagenetic facies, each of them constrained by a different truncation rule. Depositional and diagenetic facies are modelled with several Gaussian random functions, which the Earth modeller may choose to correlate to each other. The first simulation is used as secondary data to constrain the proportions of the second simulation. Several case studies using PGS to model carbonate deposits are summarized in Table 2.3, of which two use bi-PGS.

Table 2.3: Different case studies of carbonate deposits modelled with PGS

Authors	No. of depositional facies	No. of diagenetic facies	bi-PGS
Hamon et al. (2016)	10	5	Yes
Doligez et al. (2011)	9	5	Yes
Doligez et al. (2011)	9	7	No
Galli et al. (2006)	9	0	No
Amour et al. (2012)	10	0	No

Datasets

The datasets used by Amour et al. (2012) and Doligez et al. (2011) were presented previously in Sections 2.2 and 2.3. Hamon et al. (2016) model an outcrop of a mixed siliciclastic-carbonate ramp system, in the Early Eocene Alveolina Formation (Spain), from ten sedimentary sections of about 100 m thickness. Doligez et al. (2011) also built an Earth model that is 50 km long, 50 km wide and 340 m thick, based on two outcrops of a carbonate ramp in the Mississipian Madison Formation (Wyoming, Utah) studied in detail by Barbier et al. (2012) and two wells of the Madison reservoir (in an unspecified field). Galli et al. (2006) model algal mound deposits in the Paradox Basin (Utah) using an outcrop covering an area of several square kilometres and is 30 m thickness.

Facies Classification

The different case studies model facies using the Dunham classification and/or facies associations interpreted as environments of deposition. Galli et al. (2006) and Amour et al. (2012) model facies mainly based on the Dunham classification such as sponge mudstone facies and black laminated mudstones. Similarly, Doligez et al. (2011) model nine lithofacies defined by texture and fossil content in both of their studied datasets. Hamon et al. (2016) model ten facies associations interpreted as environments of deposition, which are based on groupings of sixteen textural facies.

Diagenetic facies are usually modelled separately, either with a nested approach (Doligez et al., 2011, Wyoming) or with bi-PGS (Hamon et al., 2016), which allows to model all the observed diagenetic facies and their appropriate geometries. For example, Doligez et al. (2011, Spain) describe five types of calcite cement, which can overprint different depositional facies and cut across their boundaries.

Input Parameters

There are two inputs of PGS, the truncation rule defining facies contacts and proportions, and the variograms of the latent Gaussian random functions, defining facies geometries. The studies considered here mainly discuss the truncation rule, which can be quite elaborate (except for Amour et al., 2012, who do not give the truncation rule). Galli et al. (2006) define two truncation rules for two different zones, which have different transitions according to their conceptual geological model. The conceptual geological model is normally used to define the truncation rule. For instance, Doligez et al. (2011) assume that the wackestone facies should not be in contact with the sandstone facies. Hamon et al. (2016) use a two-dimensional truncation rule for depositional facies and a one dimensional truncation rule for diagenetic facies. The case studies also use non-stationary facies proportions (Doligez et al., 2011; Amour et al., 2012; Hamon et al., 2016), in the form of facies proportion curves and a facies proportion matrix.

The studies do not provide much discussion of the choice of the variogram model and do not check that the resulting facies variograms or transiograms are well constrained by input data. Doligez et al. (2011) and Hamon et al. (2016) explain that they chose Gaussian variograms so that facies have smooth boundaries, and the variogram range is defined as the maximum extent of the facies in the direction of interest. For example, Hamon et al. (2016) chose lateral ranges of 100 m and 5 km but do not explicitly mention to which Gaussian random function or to which direction they refer.

Results

The authors do not a posteriori examine the two-point statistics of the corresponding simulations as a check of whether the input data have been honoured. Amour et al. (2012) observe that the facies proportion curves inputed in the model are honoured in the realisations and that facies have the right lateral extent compared to the outcrop. Amour et al. (2012) also observe that facies are more ordered with PGS than by using SIS. Hamon et al. (2016) also observe that the realisations reproduce accordingly the conceptual model of the outcrop. For instance,

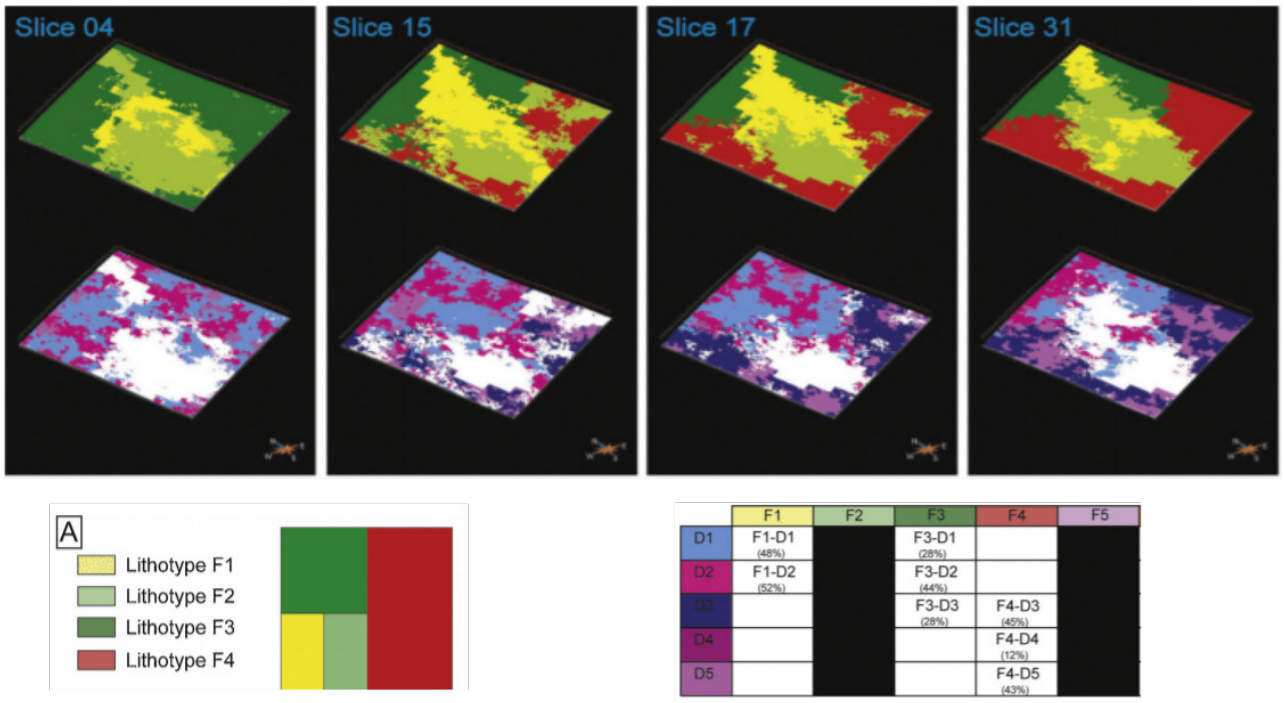

Figure 2.4: Earth models of the Alveolina Formation simulated with bi-PGS (Hamon et al., 2016). The realizations show depositional facies (top row) and diagenetic facies (bottom row). The truncation rule for the depositional facies is also displayed, along with a table explaining how diagenetic facies overprint depositional facies.

they check that patch reefs and channels have the right geometries, which are controlled by the facies proportions curves.

Authors also inspect visually the realisations to confirm that the truncation rules are honoured. For example, Fig. 2.4 shows a bi-PGS simulation with the associated truncation rule and relationships between depositional and diagenetic facies (Hamon et al., 2016). The contacts between facies are defined by the truncation rule and the distribution of the different depositional facies controls the distribution of the diagenetic facies. For example, depositional facies 2 (light green) is not overprinted by diagenesis as defined in the table (Fig. 2.4), which is reproduced in the realisation (Fig. 2.4). Similarly, depositional facies 1 (yellow) is only overprinted by diagenetic facies 1 and 2 (blue and pink) in the realisation, as defined in the table (Fig. 2.4).

Discussion

Authors have developed very sophisticated truncation rules to accurately model facies contacts. This shows that PGS can be readily adapted when facies contacts are a key constraint in the modelling. The work of Renard et al. (2008) extends this ability to the modelling of specific contacts between depositional and diagenetic facies, which is not conducted with other geostatistical methods. However, not much work has been carried out on the impact of the latent variables variograms, and Gaussian variograms are mostly used. It would be possible to use other types of variograms, for example containing hole-effects, and to study their impact on simulated facies architectures (as in Beucher and Renard, 2016). This would allow PGS to control spatial relationships between facies in addition to constraining facies contacts.

In none of the case studies were the two-point statistics of the facies distributions computed on the data, in order to choose the variogram models of the latent Gaussian random functions and their scale factors. Therefore, there are no guarantees that the Earth models are appropriately constrained and that the facies architectures have the right properties. Some automatic approaches have been developed to define the variogram model from two-point statistics (Desassis et al., 2015), and could be applied to case studies such as those described above.

2.6 Multi-Point Statistics Simulation

Introduction

Multi-Point Statistics (MPS) model facies distributions using a so-called "training image" as a model parameter (Strebelle, 2002). Instead of simply reproducing two-point statistics between facies like SIS, MPS reproduces high-order statistics between different facies. The resulting models display complex facies architectures, such as those of fluvial channel deposits, with accurate connectivity (Strebelle, 2002). However, building a facies Earth model in three dimensions requires a training image in three dimensions. Such a training image is not obtained easily, especially for carbonate deposits. One of the challenges of using MPS for carbonate

Table 2.4: Different case studies of carbonate deposits modelled with MPS

Authors	heterogeneities	Training image
Carrillat et al. (2010)	Bars	TGS
Janson and Madriz (2012)	Algal-mounds	Surface-based
Jung and Aigner (2012)	Rudist reef mound	object-based
Jung et al. (2012)	Shoal bodies	Hand-drawn

facies modelling is thus to create or to obtain (seismic, outcrop analogues, satellite images) an appropriate training image. Table 2.4 reports case studies of carbonate facies modelling with MPS along with the method used to create the training image.

Datasets

The dataset used by Janson and Madriz (2012) was described previously in Section 2.3. Carrillat et al. (2010) modelled a carbonate reservoir from well data, with no further information about the geological context. Jung and Aigner (2012) built an Earth model that is approximately 8 km long and 4 km wide (no thickness given) from outcrops of a Cenomanian carbonate platform in southern France, studied by Philip (1993) and Gari (2008). Jung et al. (2012) built an Earth model that is 36 km long, 25 km wide and 70 m thick from outcrop data at 49 locations collected by Palermo et al. (2010) in Germany in the Muschelkalk and containing shoal bodies.

Facies Classification and Training Image

Table 2.4 shows a great diversity of methods to create the training images. In most of the case studies, authors use a geostatistical method to create the training image itself. For example, Carrillat et al. (2010) create a three-dimensional training image with Truncated Gaussian Simulation. The facies are simply shale, poor, medium and good reservoir lithologies. Janson and Madriz (2012) create their training image based on a surface-based simulation constrained by a Gaussian random function. The Gaussian random function is mathematically transformed in order to render the desired mound geometries, and the result is then used as a training image.

Similarly, Jung and Aigner (2012) create a training image of rudist patch reefs with an object-based method from a conceptual model in the open platform zone of the outcrop dataset. The conceptual model shows two facies with an asymmetrical contact: the reef-flank facies overlying the reef-core facies. In the training image this asymmetrical contact is not preserved. Other training images are used in the other zones of the outcrop dataset. For more details on the generation of the training image, these authors refer to a tool called TiGenerator (Maharaja, 2008).

In another case study, Jung et al. (2012) hand-draw a training image in two dimensions from a conceptual model. Some of the facies have an asymmetrical contact, for example oncoidal wackestone to packstone facies are overlain by cross-bedded oolitic grainstone facies. However the training image remains two-dimensional when it should be three-dimensional.

Simulation Results

Authors mainly comment on the Earth models based on visual inspection and do not provide a quantitative assessment of the resulting realizations. Figure 2.5 shows two simulations with MPS from Jung and Aigner (2012) (left) and Jung et al. (2012) (right). The Earth model of Jung and Aigner (2012) is subdivided into three zones that transition laterally into each other (Fig. 2.5, left), and was built using a different training image for each zone. The enlarged image showing orange and yellow facies is from the zone with the reef-core and reef-flank facies (Fig. 2.5, left). The reef-flank facies surrounds the reef-core facies but is not specifically overlying it, as it should according to the conceptual geological model (Jung and Aigner, 2012). It is difficult to check if the simulation of Jung et al. (2012) (Fig. 2.5, right) resulting from the hand-drawn training image preserved the asymmetrical contact between oncoidal wackestone to packstone facies and cross-bedded oolitic grainstone facies.

Janson and Madriz (2012) observe that mound debris overlies the mound cores, as observed in the training image. Carrillat et al. (2010) observe that facies are all in contact in the Earth model simulated with MPS, while they are not in the Earth model simulated with Truncated Gaussian Simulations (TGS).

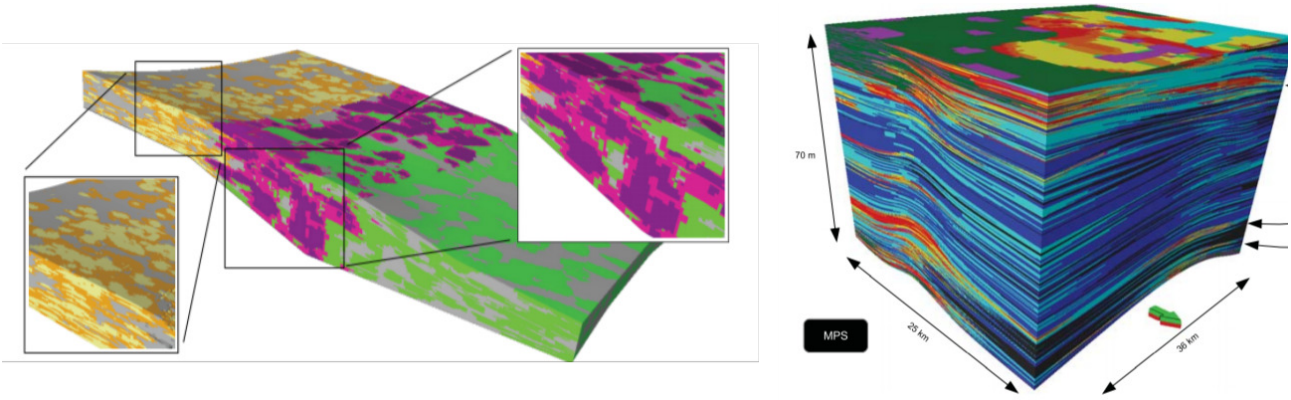

Figure 2.5: Two realizations of Earth models simulated with MPS, from Jung and Aigner (2012) (left) and Jung et al. (2012) (right). Jung and Aigner (2012) subdivide the Earth model into three lateral zones: open platform, slope and basin, and use different training images in each of these zones.

Discussion

Using MPS could be powerful for carbonate reservoirs because of MPS' ability to capture complex geometries and spatial relationships between facies. There is a great variety of empirical methods to build three-dimensional training images, although it appears sometimes self-contradictory to combine MPS with other geostatistical methods. For instance, Carrillat et al. (2010) combine MPS with TGS. While the characteristic of TGS is to constrain facies contacts in their Earth models, MPS does not necessarily honour the contacts observed in the training image, as the authors noted (Carrillat et al., 2010). It would be simpler to only use SIS or PGS rather than MPS combined with TGS if an Earth modeller wanted all facies to be in contact.

Generally, the case studies lack rigour in the creation of the training images. For instance, variograms could have been calculated on the training images to check whether they are representative of the case study datasets. In several examples the inter-facies relationships of the conceptual model were not honoured in the resulting Earth model, for example when the training image is built with an object-based method that does not reproduce spatial relationships between facies (Jung and Aigner, 2012).

2.7 Summary

Which is the Optimal Method for Facies Modelling of Carbonate Reservoirs?

All of the geostatistical techniques used in facies modelling of siliciclastic reservoirs have also been tested on carbonate reservoirs, although to a lesser extent for Markov Chains transiogram-based methods. This is surprising because Markov Chains transiograms can accurately represent spatial relationships between facies, which can be crucial for carbonate strata.

The optimal method obviously depends on the geology to be modelled and on the geologist's conceptual model. If the facies geometries are well-defined and the facies classification relatively simple, object-based simulations might be optimal. If this is not the case, it might then be better to use a pixel-based approach such as SIS, which gives more flexibility in facies geometries. However, SIS is unable to model spatial relationships between facies, which are commonly key to defining facies architecture in reservoirs. MPS is potentially able to model inter-facies relationships, but these are difficult to incorporate in the three-dimensional training image. My recommendation is rather to use transiogram-based methods or PGS, which both seem capable of capturing the required inter-facies relationships.

Cyclicity and Rhythmicity

In the Introduction of this thesis (Chapter 1), cyclicity and rhythmicity were defined respectively as facies ordering and repetition of facies at stratigraphic intervals of constant thickness. It is noteworthy that none of the case studies described in this chapter model these features, even though these concepts are characteristic aspects of many carbonate facies successions (Strasser, 1988; Goldhammer et al., 1990; Lindsay et al., 2006; De Boer and Wonders, 1984; House, 1985). For example, Amour et al. (2012), Koehrer et al. (2010) and Aigner et al. (2007) observe some metre-scale cycles, but do not attempt to model them.

In the case study by Jung et al. (2012), the training image shows a facies ordering, but it is not clear if the resulting Earth model retains this ordering, and it is not discussed by the authors.

Theoretically, MPS should be able to model facies cyclicity but the challenge remains to build cyclic three-dimensional training images. It is difficult to assess if rhythmicity is present in the case studies because the experimental variograms are not shown, but SIS and PGS should be able to model hole-effects.

Diagenesis

The bi-PGS method seems the most promising approach to model diagenesis. It is the only method that is capable of using a separate classification for depositional and diagenetic facies and jointly simulating the two corresponding facies fields. It allows the Earth modeller to define specific diagenetic facies that can be correlated to depositional facies. In other applications not based on bi-PGS, authors either combine depositional and diagenetic observations into a single facies classification, or use a nested approach to simulate diagenesis within depositional facies. These two approaches are limited because they do not allow diagenetic facies to cut across boundaries between depositional facies in a consistent manner. Therefore, it seems logical to recommend the use of bi-PGS for modelling diagenesis.

Chapter 3

Research Overview

This chapter gives a brief overview of the research that I conducted in the past three years. It also serves as a logical link between the different chapters that have been submitted for publication as separate peer-reviewed papers.

3.1 First Year, Modelling Facies Asymmetry

The starting point of this thesis was the work of Carle and Fogg (1996), who developed the transiogram as a tool to quantify transition probabilities between facies as a function of distance. Crucially, as compared to the variogram, the transiogram can quantify asymmetry between facies transitions along one direction or its opposite. One may wonder why mathematical geologists have not addressed this limitation of the variogram earlier, given that facies asymmetry characterizes (for example) shallowing upward facies cycles, a feature extensively observed in shallow-marine carbonate and siliciclastic reservoirs (e.g., Lindsay et al., 2006). I found the existence of facies asymmetry by studying papers on the Latemar carbonate platform (Egenhoff et al., 1999) and the method of Carle and Fogg (1996) appeared as a good candidate to model such a dataset.

However, the method of Carle and Fogg (1996) is based on Markov Chains, which restrict the use of hole-effects (pseudo-oscillations) in transiograms (Dubrule, 2017). Such oscillations

are common in data such as those from the Latemar carbonate platform (Egenhoff et al., 1999). Hole-effects were observed in the associated experimental transiograms and could not be reproduced. The development of another method was thus needed.

Meanwhile, I found that hole-effect models could be generated by Pluri-Gaussian Simulations (PGS) (see an example in Mosser et al. (2018)). Moreover, a few studies suggested that PGS could also be adapted to model facies asymmetry (e.g., Langlais et al., 2008). This narrowed down my research goal for the first year: to develop PGS based-methods in order to include facies asymmetry and hole-effect transiograms, and to test the new method to model data from the Latemar carbonate platform.

After reading the book of Armstrong et al. (2011), I developed a PGS method with an asymmetric shifted co-regionalization model, which successfully modelled vertical successions of asymmetric facies successions. The method generated new transiogram models that could be calculated by numerical integration (Genz, 1992), and which represent the asymmetry observed in the Latemar platform dataset. Unfortunately the observed hole-effects could not be modelled with traditional covariance models (Renard et al., 2015). This is explained further in Chapter 4 (Le Blévec et al., 2017b) and Le Blévec et al. (2016). The next research step would have to be the extension of PGS in order to properly model hole-effects in the Latemar platform dataset.

3.2 Second Year, Modelling Facies Cyclicity and Rhythmicity

First, I showed the necessity of modelling hole-effects by studying their impact on the probability distribution function (pdf) of facies thicknesses. Using the work of Matheron (1968) on renewal processes, I was able to calculate transiogram models associated with various facies thicknesses pdfs. From that, I found that facies thicknesses modelled with Gamma pdf of high order could be used to characterize hole-effects transiograms (Appendix A). This was also observed experimentally in some case studies (Le Blévec et al., 2017a). It was thus understood

that the presence of hole-effects was often linked to a low variability in the thickness of facies cycles (Appendix A).

This finding helped in characterizing rhythmicity, defined as a repetition of facies at stratigraphic intervals of more or less constant thickness, while cyclicity is defined as an ordering in the succession of facies. Although sometimes not clearly distinguished in the literature, these two definitions could clearly be differentiated by transiograms. Rhythmicity is characterized by transiogram oscillations at given distances, while cyclicity is expressed in the tangent at the origin of the transiograms (different in opposite directions). In the next step of my research, I developed a method based on transiograms for jointly modelling rhythmicity and cyclicity, as shown in the paper Le Blévec et al. (2018, Chapter 5).

The shifted PGS approach could readily model cyclicity (Le Blévec et al., 2016, 2017b, Chapter 4). I reasoned that the same method could probably be improved to model vertical (and horizontal) rhythmicity, by adding a covariance model with hole-effect. For that, I defined a covariance in the vertical direction as a product between a Gaussian covariance and the cosine function (Ma and Jones, 2001). The cosine function could provide flexibility in the covariance periodic oscillations. In lateral directions, the covariance was simply chosen to follow a Gaussian or stable model (Chiles and Delfiner, 2012). By truncation of the Gaussian random function, the covariance successfully resulted in hole-effect transiograms.

This new covariance model was not available in geostatistical packages such as RGeostats (Renard et al., 2015). Thus, I implemented a method simulating Gaussian random functions with such covariance using spectral simulations (Shinozuka, 1971). The simulations were conditioned to data via the use of Gibbs sampling and simple kriging. This last step, often time-consuming in applications, was significantly improved thanks to the screening property of separable covariances.

The method was applied to data from the Latemar carbonate platform (Peterhänsel and Egenhoff, 2008) and successfully captured the observed cyclicity and rhythmicity. However, the facies classification was simplified to only three facies although the data from the Latemar carbonate platform have previously been interpreted to contain the deposits of four depositional

environments and at least two overprinting diagenetic facies (Peterhänsel and Egenhoff, 2008). The method was thus adapted to model more facies and to represent diagenesis.

3.3 Third Year, Method Extensions

The work done in the third year of the project, and briefly summarised here, is captured in Chapter 6 (Le Blévec et al., in review). First, I extended the method for more diverse truncation rules, with a larger number of facies, and checked whether this would impede facies cyclicity and rhythmicity. By applying the method on the Latemar carbonate platform dataset (Peterhänsel and Egenhoff, 2008) with the four original depositional facies, I used a new truncation rule and the method satisfactorily modelled both facies cyclicity and rhythmicity.

Next, I was aware that Renard et al. (2008) developed a method based on PGS to model diagenesis. It seemed natural to use it for the project because it could represent diagenesis as a second superimposed facies field with much flexibility. However, it did not model facies asymmetry and so I improved it by applying the shifted linear model of co-regionalization to three instead of just two Gaussian random functions. Therefore, depositional and diagenetic facies could be ordered with respect to each other, which is appropriate in some cases such as for some syn-depositional diagenesis. This approach was successfully applied to the Latemar platform dataset (Le Blévec et al., in review, Chapter 6). Moreover, the method was calibrated by fitting cross-transiograms between the depositional and diagenetic facies fields.

Another extension of the method was to add lateral components to the shift. This allowed lateral facies asymmetry in the interior of the modern Bermuda carbonate platform to be modelled from a satellite image. Thanks to the introduction of the lateral shift, both vertical and lateral facies asymmetry was obtained, which resulted in 3D geometries in the model similar to progradational facies belts and satisfying Walther's law. The method was also applied to data from siliciclastic shoreface deposits in the Blackhawk Formation, Book Cliffs, Utah, which display non-stationary facies proportions. The dataset was quantified with embedded transition probabilities instead of transiograms to best capture the non-stationarity in facies proportions,

which was then reproduced thanks to an adaptive truncation rule.

The research conducted for this thesis thus successfully incorporated new geological constraints to facies Earth modelling. The novel method models facies cyclicity and rhythmicity but also different styles of diagenesis, and can model non stationary facies distributions in 3D.

Chapter 4

Modelling Asymmetrical Facies Successions Using Pluri-Gaussian Simulations

4.1 Abstract

An approach to model spatial asymmetrical relations between indicators is presented in a pluri-Gaussian framework. The underlying Gaussian random functions are modelled using the linear model of co-regionalization, and a spatial shift is applied to them. Analytical relationships between the two underlying Gaussian variograms and the indicator covariances are developed for a truncation rule with three facies and cut-off at zero. The application of this truncation rule demonstrates that the spatial shift on the underlying Gaussian functions produces asymmetries in the modelled one dimensional facies sequences. For a general truncation rule, the indicator covariances can be computed numerically, and a sensitivity study shows that the spatial shift and the correlation coefficient between the Gaussian functions provide flexibility to model the asymmetry between facies. Finally, a case study is presented of a Triassic vertical facies succession in the Latemar carbonate platform (Dolomites, Northern Italy) composed of shallowing-upward cycles. The model is flexible enough to capture the different transition

probabilities between the environments of deposition and to generate realistic facies successions.

4.2 Introduction

Variogram-based indicator simulation aims to distribute facies in space using first- and second-order spatial statistics as a constraint. It is widely used for modelling heterogeneous subsurface rock volumes such as hydrocarbon reservoirs and groundwater aquifers, in which data are usually sparse and deterministic methods are not appropriate. In standard oil industry practice, the facies represent regions of the reservoir where petrophysical properties such as porosity and permeability can be assumed to have statistically homogeneous distributions. Therefore, the spatial distribution of facies has a great impact on the reservoir model predictions.

While it is easy to constrain the models with the proportion and auto-covariance of each facies (Alabert, 1989; Armstrong et al., 2011), it is more complex to model the cross-indicator covariances between facies. For instance, SIS (Sequential Indicator Simulation) by modelling every facies independently (Alabert, 1989) does not reproduce cross-covariances between different facies, possibly resulting in non-realistic geological models.

With the aim of modelling spatial relationships between different facies, Carle and Fogg (1996) constrain cross-covariances using the parameters of a continuous-time Markov chain. An important outcome of their method is the possibility to model spatial asymmetry between the indicator variables. The probability of facies A to be on top of facies B can be different from that of facies A being under B. Such asymmetrical vertical stacking patterns of facies are common in the stratigraphic record as sedimentological processes tend to create and preserve shallowing-upward facies successions which are asymmetrical (Tucker, 1985; Grotzinger, 1986a; Strasser, 1988; Burgess et al., 2001). However, the model used by Carle and Fogg (1996) is memoryless and so prevents from using a hole-effect covariance and reproducing rhythmicity, which is another common feature of vertical facies successions (Fisher, 1964; Grotzinger, 1986a; Goldhammer et al., 1990; Masetti et al., 1991; Burgess et al., 2001). Another approach uses non-parametric indicator variograms for bivariate probabilities to simulate facies with asymmetrical

patterns (D'Or et al., 2008; Allard et al., 2011). The approach presented in the current paper aims to use parametric auto- and cross-covariance models that are realizable, that is associated with valid random set models (Chiles and Delfiner, 2012).

Pluri-Gaussian simulations (PGS) can handle facies interactions thanks to the use of underlying continuous Gaussian variables and truncation rules defining facies ordering and geometries (Armstrong et al., 2011). Moreover, by construction, the PGS formalism leads to a general cross-covariance model between facies that is realizable (Chiles and Delfiner, 2012). Developing a flexible multivariate Gaussian framework allows to increase the range of facies patterns. For instance, the original linear model of co-regionalization (Wackernagel, 2003), applied to the underlying Gaussian functions, provides flexibility in the resulting facies thicknesses and distributions. However, the cross-correlations between the underlying Gaussian functions are symmetrical and so are the facies relations.

To overcome this limitation, some authors have proposed to use spatial shifts to transform the cross-covariances between Gaussian functions (Oliver, 2003; Apanasovich and Genton, 2010; Li and Zhang, 2011). Armstrong et al. (2011) proposed to use a similar approach when defining the linear model of co-regionalization of the underlying Gaussian variables. Although it is natural to expect that an asymmetrical cross-correlation between the Gaussian functions should lead to asymmetrical relations between facies, this approach has not yet, to our knowledge, been fully developed and tested. Moreover, the relation between the spatial shift, the correlation and the facies asymmetry has not been studied explicitly.

In this paper, we expand on the previous work described above to demonstrate that a spatial shift applied to the underlying Gaussian functions can be used to create asymmetries in the vertical stacking of facies. The sensitivity of vertical facies stacking patterns to selected parameters is then investigated. Synthetic examples are produced, and the usefulness of this method is demonstrated by modelling a real facies succession from the Triassic Latemar carbonate platform (Dolomites, Northern Italy).

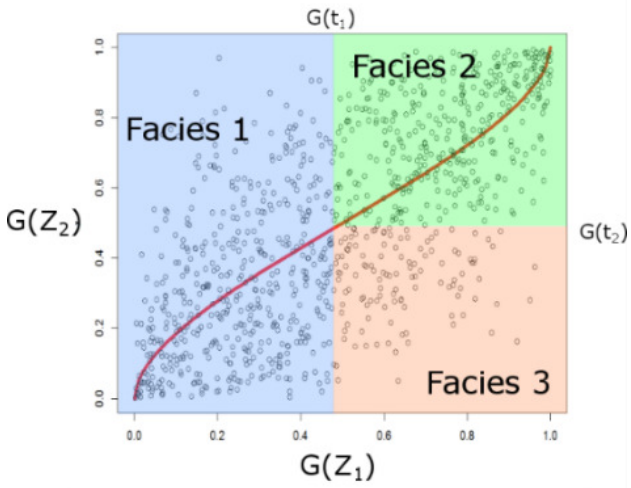

Figure 4.1: Truncation rule defining 3 facies with two Gaussian random functions Z_1 and Z_2. t_1 and t_2 are the truncations associated to each Gaussian functions and G is the Gaussian cumulative function. The red curve is defined by equation 4, with the correlation $\rho = 0.7$. 1000 random generations with a correlation $\rho = 0.7$ are performed thanks to the R package MASS (Venables and Ripley, 2013) and displayed.

4.3 Methodology

4.3.1 Context and Notations

We focus here on a simple example with three facies. The truncation rule that defines the contacts between facies and their proportion, relative to their area, can be drawn as in Fig. 4.1.

If I_1, I_2 and I_3 are the indicators of the three facies, the truncation rule defines them as follows for every location x on a vertical section

$$I_1(x) = 1, \quad I_2(x) = 0, \quad I_3(x) = 0 \text{ if } \quad Z_1(x) < q_1, \tag{4.1a}$$

$$I_1(x) = 0, \quad I_2(x) = 1, \quad I_3(x) = 0 \text{ if } \quad Z_1(x) \geq q_1, \quad Z_2(x) > q_2, \tag{4.1b}$$

$$I_1(x) = 0, \quad I_2(x) = 0, \quad I_3(x) = 1 \text{ if } \quad Z_1(x) \geq q_1, \quad Z_2(x) \leq q_2. \tag{4.1c}$$

When the indicator of a facies equals one, the corresponding facies is present at the location x. The marginal Gaussian cumulative function G applied to each Gaussian function Z_1 and Z_2 allows to have a truncation rule on which the area of a facies equals its proportion. However,

if there is a correlation between the two functions, it affects the proportion as the points tend to be located along the transformation of the correlation line ρ (Fig. 4.1) which is plotted in the axes $(G(Z_1), G(Z_2))$ and thus has for equation

$$Y = G[\rho\ G^{-1}[X]]. \tag{4.2}$$

In the example of Fig. 4.1, a positive correlation increases the proportion of facies 2 over facies 3 as shown by the larger number of points generated in the domain of facies 2. With a negative correlation, it would be the opposite. A uniform truncation rule could be obtained by applying the bi-normal Gaussian cumulative function with correlation ρ on Z_1 and Z_2, but its analytical expression is not known.

The truncation rule does not contain spatial information and so does not control asymmetries. As the aim of this study is to model asymmetrical relations, the transition probability from one facies i to another j should be different in opposite directions h and $-h$

$$t_{ij}(h) = \frac{Pr\{I_j(x+h) = 1, I_i(x) = 1\}}{Pr\{I_i(x) = 1\}} \neq t_{ij}(-h). \tag{4.3}$$

Under the stationary hypothesis, the transition probability is independent of location. This transition probability results from the Gaussian function parameters: correlation ρ, thresholds t_1 and t_2, Gaussian correlation models $\rho_{Z_1}(h)$ and $\rho_{Z_2}(h)$ and the cross-correlation $\rho_{Z_1 Z_2}(h)$ that can be asymmetric.

4.3.2 Relation Between the Indicators and Gaussian Functions

Understanding the link between the facies transition probabilities and the parameters of the underlying bi-Gaussian function would help in inferring a pluri-Gaussian model resulting in the correct asymmetrical transition probabilities. Armstrong et al. (2011) show that the covariance of the facies indicator can be expressed as a multi-variable integral of the underlying bi-Gaussian density. For instance, the non-centered cross-covariance, between facies 2 and 3, $C_{23}(h)$, is

defined as

$$C_{23}(h) = E[I_2(x)\ I_3(x+h)] = Pr\{I_2(x) = 1, I_3(x+h) = 1\}. \tag{4.4}$$

According to Eqs. (4.1), we have

$$C_{23}(h) = Pr\{Z_1(x) > q_1, Z_2(x) > q_2, Z_1(x+h) > q_1, Z_2(x+h) < q_2\}. \tag{4.5}$$

This is the joint probability of four Gaussian events with their dependence described by the correlation matrix

$$\Sigma(h) = \begin{bmatrix} 1 & \rho & \rho_{Z_1}(h) & \rho_{Z_1Z_2}(h) \\ \rho & 1 & \rho_{Z_1Z_2}(-h) & \rho_{Z_2}(h) \\ \rho_{Z_1}(h) & \rho_{Z_1Z_2}(-h) & 1 & \rho \\ \rho_{Z_1Z_2}(h) & \rho_{Z_2}(h) & \rho & 1 \end{bmatrix}. \tag{4.6}$$

$C_{23}(h)$ can then be expressed as an integral of the quadri-variate Gaussian density $g_\Sigma(h)(u, v, w, z)$ with the covariance matrix previously described

$$C_{23}(h) = \int_{q_1}^{\infty}\int_{q_2}^{\infty}\int_{q_1}^{\infty}\int_{-\infty}^{q_2} g_\Sigma(h)(u, v, w, z)\ du\ dv\ dw\ dz. \tag{4.7}$$

As we work with three facies (Fig. 4.1), the covariance between facies 1 and facies 2 is expressed by a triple integral, while a double integral defines the auto-covariance of facies 1.

4.3.3 The Spatial Shift Applied to the Linear Model of Co-regionalization

The linear model of co-regionalization presented by Wackernagel (2003) is a flexible model for p-multivariate simulations and is chosen here. We also incorporate a shift on the covariance matrix C as proposed by Li and Zhang (2011). (Armstrong et al., 2011) propose a way to simulate such a multivariate field from two independent Gaussian functions Y_1 and Y_2 with covariances $\rho_{Y_1}(h)$ and $\rho_{Y_2}(h)$

$$Z_1(x) = Y_1(x), \tag{4.8a}$$

$$Z_2(x) = \frac{\rho}{\rho_{Y_1}(\alpha)}\, Y_1(x+\alpha) + \sqrt{1 - \frac{\rho^2}{\rho_{Y_1}(\alpha)^2}}\, Y_2(x). \tag{4.8b}$$

The spatial shift, α, is the distance at which the correlation between the two Gaussian functions Z_1 and Z_2 is maximal, and ρ is the correlation between the two simulated Gaussian functions Z_1 and Z_2 at the same location. We can directly deduce from the square root term in Eq. (4.8b) the condition of validity of the model

$$-\rho_{Y_1}(\alpha) < \rho < \rho_{Y_1}(\alpha) \tag{4.9}$$

This condition originally results from the fact that the variance of the Gaussian functions Z_1 and Z_2 is one. It is now possible to relate the covariances ρ_{Z_1} and ρ_{Z_2} of the Gaussian random functions Z_1 and Z_2 to the covariances of Y_1 and Y_2

$$\rho_{Z_1}(h) = \rho_{Y_1}(h), \tag{4.10a}$$

$$\rho_{Z_2}(h) = \frac{\rho^2}{\rho_{Y_1}(\alpha)^2}\, \rho_{Y_1}(h) + [1 - \frac{\rho^2}{\rho_{Y_1}(\alpha)^2}]\, \rho_{Y_2}(h), \tag{4.10b}$$

and the cross-correlations between Z_1 and Z_2, which are asymmetric

$$\rho_{Z_1Z_2}(h,\alpha) = \rho\, \frac{\rho_{Z_1}(|h+\alpha|)}{\rho_{Z_1}(\alpha)}, \tag{4.11a}$$

$$\rho_{Z_1Z_2}(-h,\alpha) = \rho\, \frac{\rho_{Z_1}(|h-\alpha|)}{\rho_{Z_1}(\alpha)}. \tag{4.11b}$$

It is also interesting to see that

$$\rho_{Z_1Z_2}(-h,-\alpha) = \rho_{Z_1Z_2}(h,\alpha). \tag{4.12}$$

The different parameters of the model are summarized in Tab. 4.1.

Table 4.1: Symbols of the different parameters of the shifted pluri-Gaussian model

Parameter	Signification
Z_1	First Gaussian field
Z_2	Second delayed Gaussian field
$t_{ij}(h)$	Upward transition probability from facies i to facies j as a function of distance h
p_i	Proportion of facies i
$\rho_{Z_1}(h)$	Covariance function of Z_1
$\rho_{Z_2}(h)$	Covariance function of Z_2
ρ	Correlation coefficient between Z_1 and Z_2
$\rho_{Z_1Z_2}(h)$	Cross-correlation between Z_1 and Z_2 at distance h
α	Shift in the cross-correlation between Z_1 and Z_2
a_1	Range of the first Gaussian function with a Gaussian variogram, practical range $a_1\sqrt{3}$
a_2	Range of the first Gaussian function with a Gaussian variogram, practical range $a_2\sqrt{3}$

4.4 Result

In this section, we study the indicator transiograms derived from the shifted linear model of co-regionalization applied with PGS and with the truncation rule in Fig. 4.1. We first express the analytical expressions for a special case and then develop a sensitivity study in the general case thanks to numerical Gaussian integrations. Gaussian variograms for the Gaussian functions are used in order to have a linear behaviour at the origin on the indicator transiograms.

4.4.1 Analytical Study of the Asymmetry

We focus here on the special case where $q_1 = q_2 = 0$ as some analytical expressions can be found between the Gaussian functions and the transition probabilities.

Behaviour of the Asymmetrical Transition Probability

With the truncation rule used in Fig. 4.1, the transition probability between facies 1 and 2 can be written as a triple integral. Its analytical expression, developed in the appendix (Eqs. 4.22 and 4.23), is the following

$$t_{12}(h) = -\frac{1}{4} + \frac{1}{2\pi}\Big[\arccos\Big(\rho\,\frac{\rho_{Z_1}(|h+\alpha)}{\rho_{Z_1}(\alpha)}\Big) + \arccos(\rho_{Z_1}(h)) + \arcsin(\rho)\Big]. \tag{4.13}$$

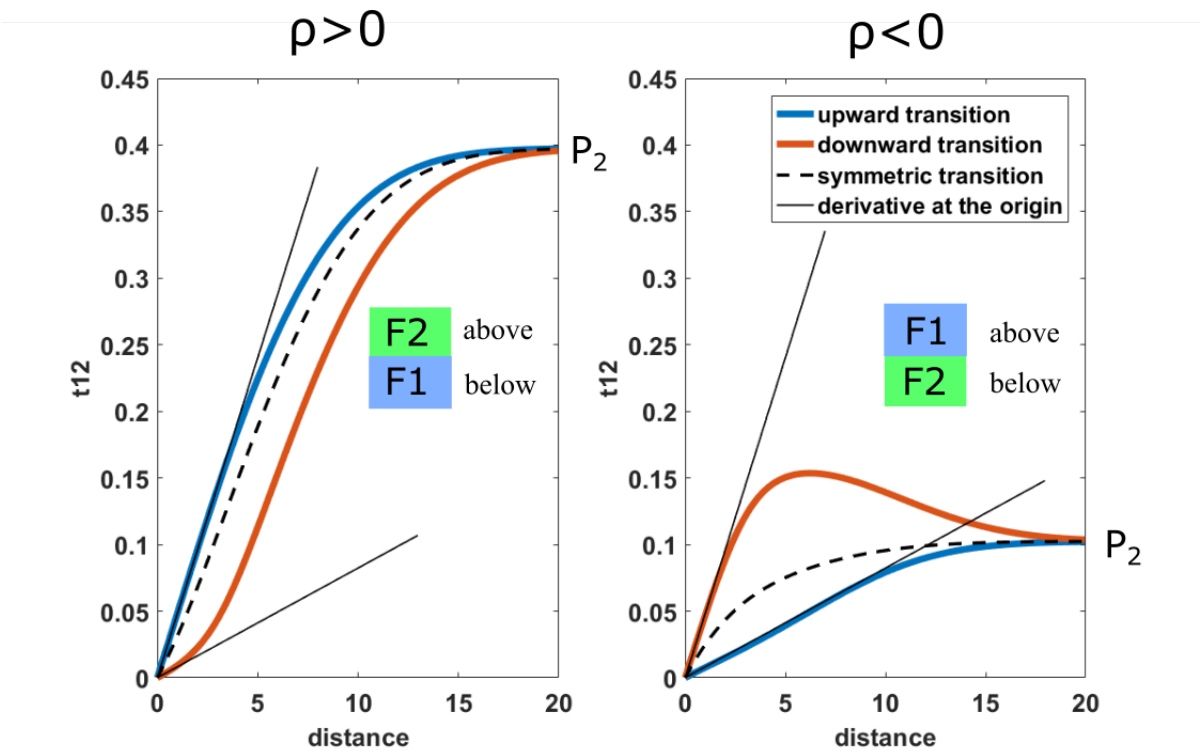

Figure 4.2: Influence of a positive shift on the transition probabilities from facies 1 to facies 2 with different values of the proportion p_2 of facies 2. The coefficient ρ is either 0.8 or -0.8. The Gaussian function has a Gaussian variogram with range 8 (practical range =13.85) and the shift is 3. The upward and downward transitions are deduced from Eq. 4.13, such as the dotted line obtained with a shift equal to 0, and the black tangents are obtained from Eqs 4.17 4.18.

Therefore, the shift α and the correlation ρ must be non-zero to bring asymmetry (Fig. 4.2). We can also deduce the relation

$$t_{12}(-h, -\alpha) = t_{12}(h, \alpha), \tag{4.14}$$

which means that changing the sign of the shift allows the asymmetry between the two facies to be switched.

We can see that if the correlation and shift are positive, and the transition probability tends towards a facies with low proportions, the curve has a very high concavity with a maximum before the range (Fig. 4.2, right). If the correlation is negative and the transition probability tends towards a facies with high proportion, the curve has an inflexion point (Fig. 4.2, left). In the opposite direction, the behaviour is always different, highlighting the asymmetry. If there is no shift, there is no asymmetry (Fig. 4.2).

Asymmetry in facies contacts

The frequency of contacts between two given facies can be derived from the derivative of the cross-transition probability at the origin, which is the rate of transition from one facies to the other per unit length. We can express the rate of transition upward T_{12}^{+} and downward T_{12}^{-} in the case of a Gaussian variogram by differentiating Eq. (4.13)

$$T_{12}^{+}(\alpha,\rho,a_1) = \frac{1}{2\pi}\Big[\frac{\sqrt{2}}{a_1} + \alpha\frac{2\rho}{a_1^2\sqrt{1-\rho^2}}\Big] \tag{4.15a}$$

$$T_{12}^{-}(\alpha,\rho,a_1) = \frac{1}{2\pi}\Big[\frac{\sqrt{2}}{a_1} - \alpha\frac{2\rho}{a_1^2\sqrt{1-\rho^2}}\Big] \tag{4.15b}$$

From these equations, it is clear that if the correlation ρ and the shift α are positive, the probability of having facies 2 on top of facies 1 is higher than of having facies 1 on top of facies 2. It can be interesting to see for which shift the transition rate is maximal. Lets take

$$\alpha_{lim} = a_1\frac{\sqrt{2(1-\rho^2)}}{2\rho} \tag{4.16}$$

In that case, we have

$$T_{12}^{+}(\alpha_{lim},\rho,a_1) = \frac{\sqrt{2}}{a_1\ \pi} \tag{4.17a}$$

$$T_{12}^{-}(\alpha_{lim},\rho,a_1) = 0 \tag{4.17b}$$

With this shift, facies 1 cannot make a transition to facies 2 going downwards as the transition rate is 0. For the upward transition, it can be noticed that the expression of the transition rate is the inverse of the mean length of facies 1 (Lantuéjoul, 2002). This implies that the upward transition rate from facies 1 to facies 3 is zero with the closing relations of the transition rate matrix Q

$$Q = \begin{bmatrix} -1/L_1 & 1/L_1 & 0 \\ 0 & -1/L_2 & 1/L_2 \\ 1/L_3 & 0 & -1/L_3 \end{bmatrix}, \tag{4.18}$$

with L_i as the mean lengths of the different facies. Therefore, this shift gives the maximum of asymmetry and allows to build perfect geologic asymmetrical sequences. However, the shift is

also bounded by Eq. (4.9), and consequently Eqs. (4.16, 4.17, 4.18) are not possible. As the transition rates increase linearly with the shift, the maximum of asymmetry is obtained for the higher shift which is the following according to Eq. (4.9)

$$\alpha_{max} = a_1 \sqrt{-\log \rho}. \tag{4.19}$$

It can be noted that the expressions of α_{lim} and α_{max} converge to each other when ρ tends to one. Thus, for a correlation that tends to one, α_{max} gives upward and downward transition rates that tend, respectively, to $1/L_i$ and 0, allowing to create perfect asymmetrical sequences (Eq. 4.18). This limit case can also be obtained by simulating only one Gaussian function and use the shifted equivalent as the second Gaussian function.

The expressions of the multi-Gaussian integrals have allowed asymmetries for a truncation rule with cut-off at 0 to be analytically expressed. Lantuéjoul (2002) gives a solution for a general truncation rule when the correlation tends to 1. This might allow development of more general expressions with thresholds.

4.4.2 Sensitivity Analysis for a General Truncation Rule

The Gaussian integral cannot be computed analytically in the general case with cut-offs different from 0. However, it can be computed numerically (Genz, 1992) using a code available on R (Genz et al., 2019; Renard et al., 2015). Consequently, we have access to all the transition probabilities, and the correlation ρ can be changed while keeping the proportions constant which is not possible analytically.

This is carried out by minimizing an objective function quantifying the difference between the targeted and simulated proportions computed with the Gaussian numerical integral (Genz, 1992). It can also be done with a maximum likelihood estimation of the target proportions by generating random correlated Gaussian values. Understanding the impacts of the correlation and the shift at constant proportions is important for manually fitting transition probabilities (Fig. 4.3).

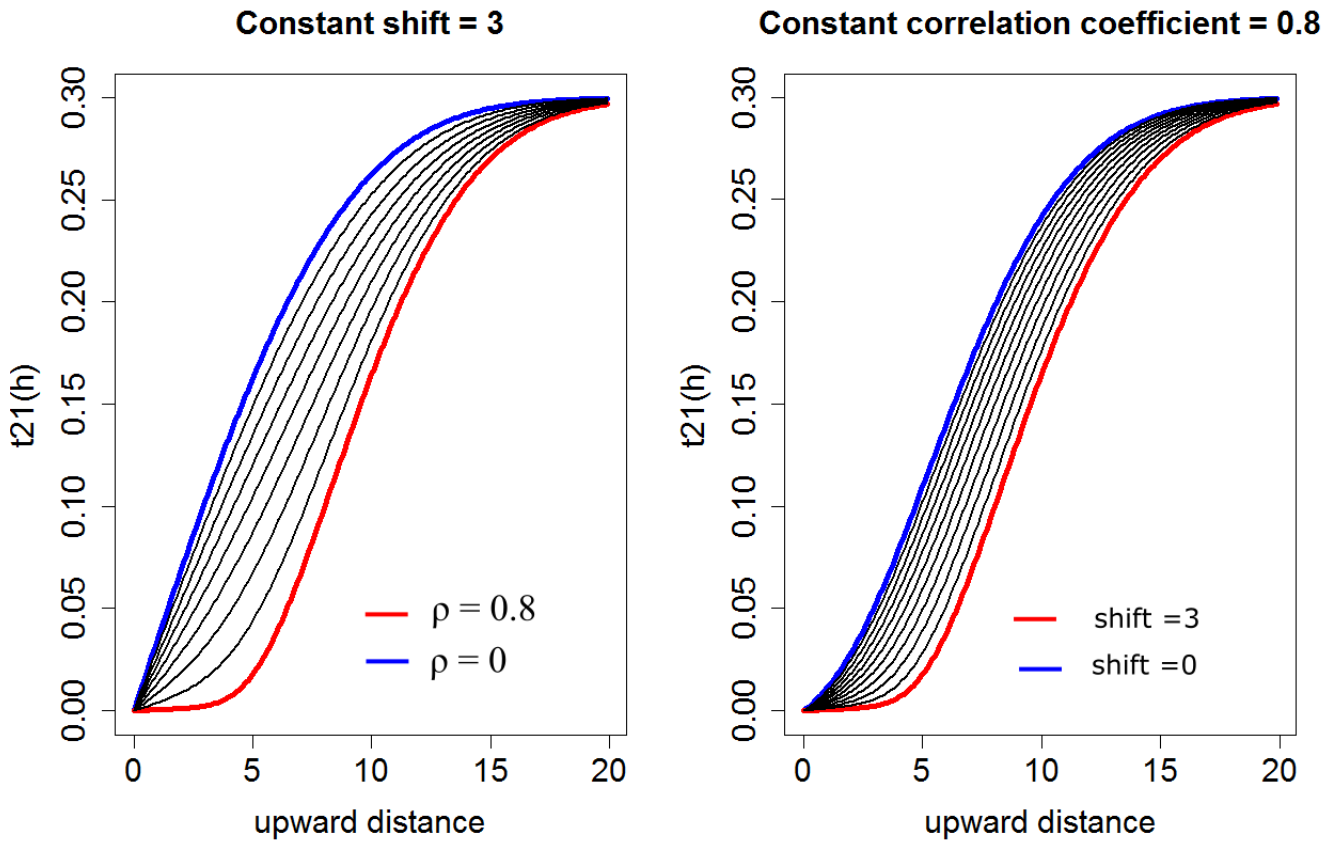

Figure 4.3: Comparison of the impact of the correlation and the shift on the transition probability from facies 2 to facies 1 upwards. The step for the black curves is 0.1 for the correlation (left) and 0.3 for the shift step (right). The range of the first Gaussian variogram is 8, the proportion of facies 1 is 0.3 and facies 2 is 0.4.

We can see in Fig. 4.3 that both the correlation and the shift have an impact on the tangent at the origin which provides a flexibility to match the asymmetry between facies contacts. The asymmetrical limit behaviour α_{lim} (Eq. 4.16) seems to have been reached with $\rho = 0.8$ and $\alpha = 3$ as the transition rate is close to 0 for these values. The two parameters also affect differently the curvature of the transition probability increasing the flexibility of the method.

4.5 Case study

This section presents a case study for illustrating the method described earlier with three facies and the truncation rule of Fig. 4.1. The geostatistical package RGeostats is used for the simulation (Renard et al., 2015). The transiograms are studied for two facies as the relation with the third can be automatically deduced from them.

4.5.1 The Latemar Dataset

Carbonate outcrops usually show significant vertical asymmetries in their facies distribution, in part explained by a gradual lateral shift in environments of depositions during sea-level high-stands, followed by non deposition during sea-level lowstands and the subsequent transgression (Catuneanu et al., 2011). For instance, the intertidal environment tends to be on top of the subtidal environment in shallowing-upward sequences (Sena and John, 2013). The Latemar massif in the Dolomites of Northern Italy shows well-documented examples of asymmetrical vertical facies sequences in a carbonate platform. As reported by Egenhoff et al. (1999), a typical asymmetrical, upward-shallowing succession is bounded by a supratidal exposure surface at its top, which tends to cap intertidal-to-shallow- subtidal grainstones that overlie subtidal wackestones (Fig. 4.4).

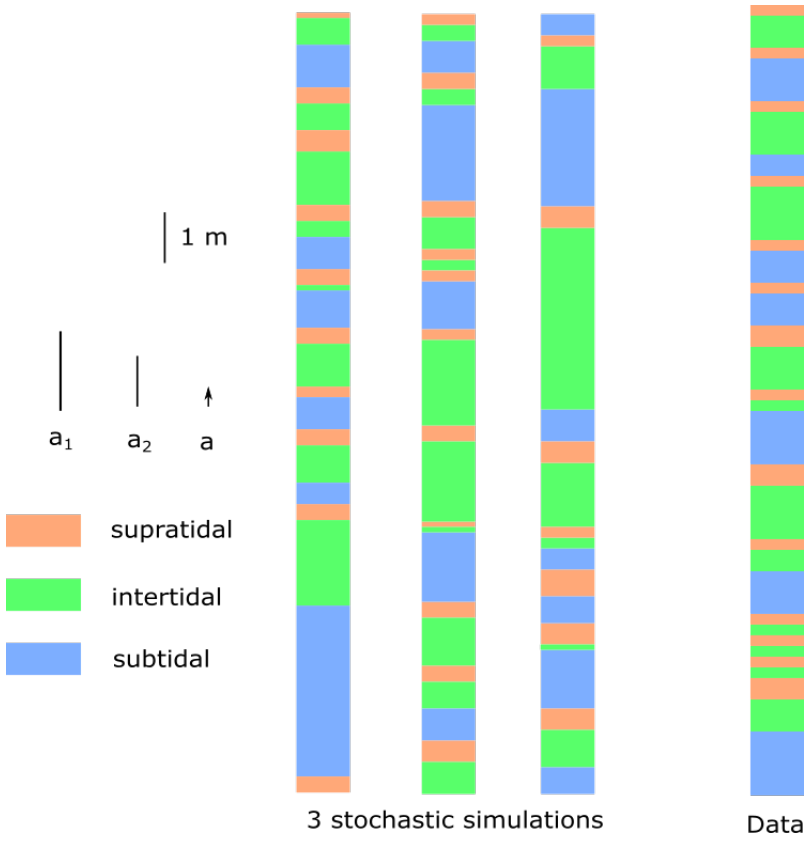

Figure 4.4: Comparison between the vertical section of the Latemar section reported by Egenhoff et al. (1999) and simulations with asymmetrical pluri-Gaussian simulations. The parameters for the simulation are the same as described in Fig. 4.5.

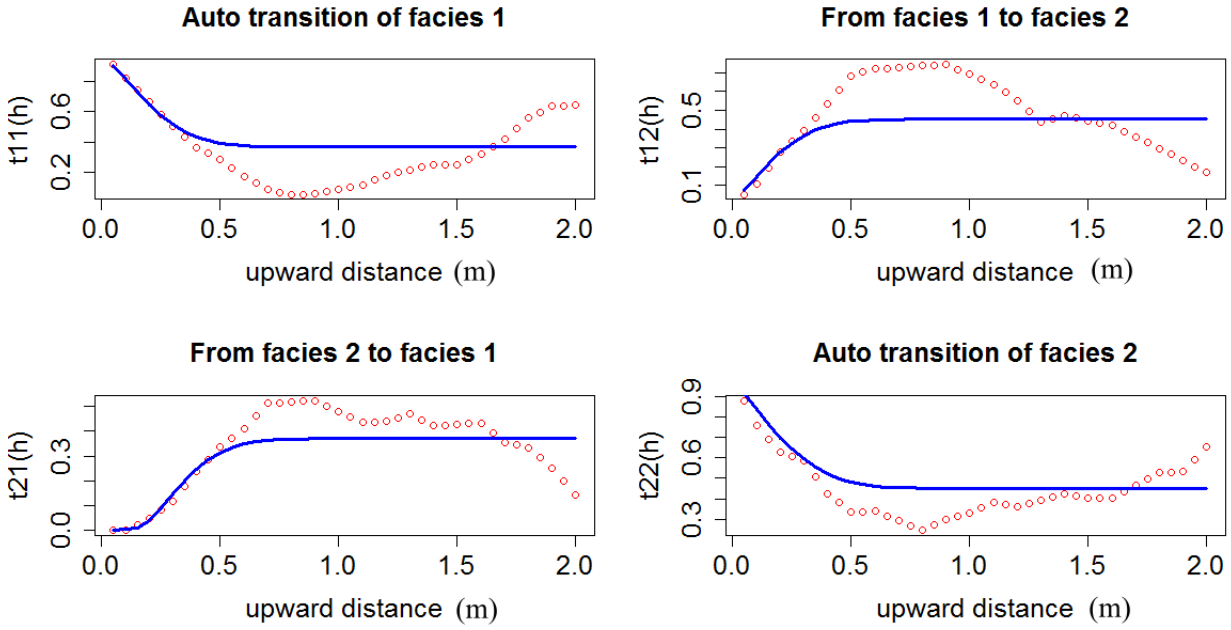

Figure 4.5: Match between experimental transition probabilities (red) observed in Figure 4 and the model (blue). Facies 1 is subtidal and facies 2 intertidal. The parameters used for the model are: 0.9 for the range of the first Gaussian, 0.52 for the range of the second Gaussian, 0.13 for the shift and 0.8 for the correlation.

4.5.2 Constraining the Transition Probabilities

The transition probabilities of Fig. 4.5 were derived from the data shown in Fig. 4.4. They can be fitted with the shifted linear model of co-regionalization manually through a trial-and-error process, by maximum likelihood estimation or by minimizing an objective function. In a more general context, a manual procedure is preferred as transiogram modelling is a step where geological conceptual knowledge can be incorporated. Therefore, we choose to fit manually the transition probabilities of Fig. 4.5.

As seen in Fig. 4.5, the model fitted by trial and error honours the tangent at the origin of the transition probabilities. This means that the transition rates are well constrained. Moreover, a possible hole-effect is observed in the experimental transition probabilities due to a low variance in the facies thicknesses. This effect cannot be modelled with the current model, but a hole-effect variogram on the Gaussian function should be able to model it (Dubrule, 2017).

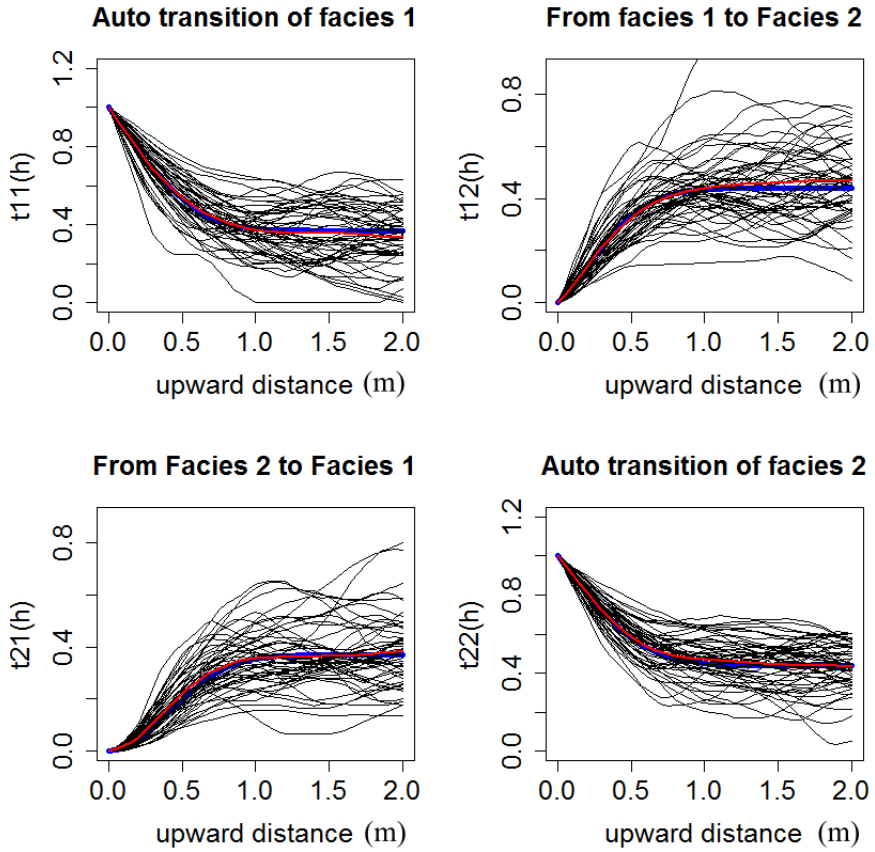

Figure 4.6: Comparison between transition probabilities model (blue) and simulated (grey) and mean of the simulated (red) on 50 simulations of the Latemar section presented Fig. 4.4. Facies 1 is subtidal, and facies 2 intertidal.

4.5.3 Facies Asymmetrical Simulation with Pluri-Gaussian Model

We build two Gaussian random functions, and then we apply the transformations described in Eq. 4.10 on three simulations (see Fig. 4.4). The asymmetry is still preserved in the simulations, with supratidal facies always on top of the intertidal facies and the intertidal facies on top of the subtidal facies. However, the limit shift α_{lim} (Eq. 4.16) has not been reached as the probability of having subtidal on top of supratidal is not 1, which is also observed on the data. To go further in the simulation analysis, the experimental transiograms are computed on 50 simulated sections and compared to the model variogram (Fig. 4.6).

This Monte Carlo study shows that the simulated transition probabilities seem to match the model well at the origin and for other distances as the mean transiogram of the simulations matches with the transiogram model (Fig. 4.6).

4.6 Discussion and Conclusion

This study has shown that the shifted linear model of co-regionalization seems well-suited to model facies transitions asymmetries using PGS. For the case of modelling three facies, the first two Gaussian variograms allow to define facies mean thicknesses, while the shift and the correlation determine the asymmetrical patterns. Therefore, every transition rate of the transiogram matrix can be inferred independently making the method very flexible. Moreover, we saw analytically and numerically that the maximum rate of transitions could be reached asymptotically, which allows to build perfect asymmetrical sequences.

More precisely, the Gaussian integral allows to fix the transition rates as with a Markov process (Carle and Fogg, 1996). However, if the number of facies is increased, it would be more difficult to respect the different asymmetries, and manual fitting of the different transition probabilities would be more complex. Automatic procedures such as maximum likelihood estimations might address that issue.

The advantage of PGS over continuous-time Markov chains is that it provides a framework in which the resulting indicator variograms are automatically valid but also quite flexible. Beyond just transition rates, the parametrical covariances can lead to linear or fractal behaviour of the indicator variogram at the origin (Chiles and Delfiner, 2012; Dubrule, 2017). Other models than the linear model of co-regionalization would allow to select different behaviours for every facies. For instance, the multivariate Matern model would allow cross-transition probabilities to have different smoothness parameters for every facies (Gneiting et al., 2010), and the spatial shift could be applied to it (Li and Zhang, 2011), which would also result in facies asymmetries.

4.A Appendix

In a similar fashion as Kendall M (1994), we consider three correlated Gaussian variates being in their respective intervals as a set of three dependent events. With the truncation rule displayed in Fig. 4.1 and thresholds that equal 0, facies 1 at location x and facies 2 at location $x + h$

correspond to one variate being negative and two positive. The indicator covariance $C_{12}(h)$ quantifies the probability of the intersection of these three events. The correlation matrix between the three Gaussian variates is the following

$$\Sigma(h) = \begin{bmatrix} 1 & \rho_{Z_1}(h) & \rho\,\frac{\rho_{Z_1}(|h+\alpha|)}{\rho_{Z_1}(\alpha)} \\ \rho_{Z_1}(h) & 1 & \rho \\ \rho\,\frac{\rho_{Z_1}(|h+\alpha|)}{\rho_{Z_1}(\alpha)} & \rho & 1 \end{bmatrix}. \tag{4.20}$$

The probability can be written as a triple integral of the corresponding Gaussian density $g_{\Sigma(h)}(u,v,w)$

$$C_{12}(h) = \int_{-\infty}^{0}\int_{0}^{\infty}\int_{0}^{\infty} g_{\Sigma(h)}(u,v,w)\; du\; dv\; dw. \tag{4.21}$$

Thanks to the Gaussian integral symmetry property, the probability of intersection of the events is the complementary of the probability of their union (Kendall et al. 1994). Therefore, by definition of the union, the intersection of the three events can be expressed as a sum of the corresponding single and pair events and so the triple integral as a sum of the single integrals that equal to 0.5 and double integrals with their respective correlation coefficient

$$C_{12}(h) = \frac{1}{2}\left(1-3*0.5+\int_{-\infty}^{0}\int_{0}^{\infty} g_{\rho_{Z_1}(h)}(u,v)\; du\; dv+\int_{-\infty}^{0}\int_{0}^{\infty} g_{\frac{\rho\rho_{Z_1}(|h+\alpha|)}{\rho_{Z_1}(\alpha)}}\; du\; dv+\int_{0}^{\infty}\int_{0}^{\infty} g_{\rho}(u,v)\; du\; dv\right) \tag{4.22}$$

Sheppard (1899) gives then the solution of the double integral that allows to obtain the final expression of the transition probability between facies 1 and 2 (equation 15):

$$\int_{0}^{\infty}\int_{0}^{\infty} g_{\rho}(u,v)du\; dv = \frac{1}{2} - \int_{-\infty}^{0}\int_{0}^{\infty} g_{\rho}(u,v)du\; dv = \frac{1}{4} + \frac{1}{2\pi}\arcsin(\rho) \tag{4.23}$$

Chapter 5

Geostatistical Modelling of Cyclic and Rhythmic Facies Architectures

5.1 Abstract

A Pluri-Gaussian method is developed for facies variables in three dimensions to model vertical cyclicity, related to facies ordering, and rhythmicity. Cyclicity is generally characterized by shallowing-upward or deepening-upward sequences and rhythmicity by the repetition of facies at constant intervals along sequences. Both of these aspects are commonly observed in shallow-marine carbonate successions, especially in the vertical direction. A grid-free spectral simulation approach is developed, with a separable covariance allowing a dampened hole-effect to capture rhythmicity in the vertical direction and a different covariance in the lateral plane, along strata, as in space-time models. In addition, facies ordering is created by using a spatial shift between two latent Gaussian functions in the Pluri-Gaussian approach. Rapid conditioning to data is performed via Gibbs sampling and kriging using the screening properties of separable covariances. The resulting facies transiograms can show complex patterns of cyclicity and rhythmicity. Finally, a three dimensional case study of shallow-marine carbonate deposits at outcrop shows the applicability of the modeling method.

5.2 Introduction

Spatial distributions of facies in sedimentary rocks are commonly characterized by cyclicity and rhythmicity in the vertical direction, and a variety of lateral patterns along stratigraphy. The resulting facies architectures control heterogeneity in hydrocarbon reservoirs and groundwater aquifers. It is therefore important to represent them in three-dimensional geostatistical earth models that are used as input to flow simulations and reserves quantification (Pyrcz and Deutsch, 2014).

Cyclicity is defined as a characteristic facies ordering in vertical successions (Wilkinson et al., 1997; Burgess, 2016). The characterization of cyclicity needs to be addressed statistically (Wilkinson et al., 1997) in order to apprehend the variability of the resulting facies patterns and to reproduce them in earth models. Facies cycles show preferential transitions between successive facies, such that one facies tends to be observed on top of another facies. This is also called asymmetry (Carle and Fogg, 1996), because the transitions between facies differ between the upward and downward directions. For example, shallow-marine carbonate rocks at outcrops (Strasser, 1988; Goldhammer et al., 1990) and in subsurface reservoirs (Lindsay et al., 2006) are typically characterized by facies cycles that record upward shallowing (regression) and that consist of subtidal facies overlain by intertidal facies then by supratidal facies. The facies succession that records upward deepening is commonly incomplete or absent, due to non-deposition or erosion, such that supratidal facies are directly overlain by subtidal facies, which mark the base of a new cycle. Such sequences are illustrated in Fig. 5.1c, d.

Classical geostatistical methods such as sequential indicator simulation (Alabert, 1989) and object-based methods (Deutsch and Tran, 2002) do not in their traditional form reproduce this asymmetric facies ordering. Multi-Point statistics (Strebelle, 2002) should be able in theory to reproduce cyclicity, but in practice, it is not easy to obtain a three dimensional training image showing cyclicity. The representation of asymmetry and facies ordering is however straightforward in one dimension with Markov Chains (Carle and Fogg, 1996; Parks et al., 2000; Li, 2007; Purkis et al., 2012) or renewal processes (Matheron, 1968), which are based on probabilities of transition between facies, but are difficult to generalize to two or three dimensions.

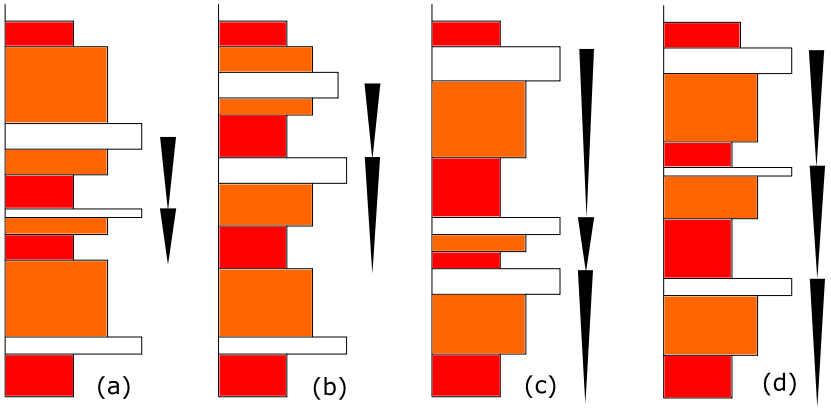

Figure 5.1: (a-d) Synthetic examples of facies sequences: (a) cyclic (two cycles), non rhythmic, (b) cyclic (two cycles) and red facies presents rhythmicity, (c) perfect cyclicity, non rhythmic (d) perfect cyclicity and rhythmicity

Rhythmicity is another important aspect observed in vertical facies successions. It is characterized by the repetition of a facies at a constant interval along a sequence, a feature which has commonly been used to interpret periodic processes of deposition (e.g., via analysis of Fischer plots) (Read and Goldhammer, 1988). Note that periodic processes (i.e., repetitive processes when looking at a time series) can either result in rhythmic sequences (when sedimentation rates are similar from cycle to cycle) or non rhythmic sequences (if sedimentation rates change between cycles). Because the space domain is considered here, we use the term rhythmicity rather than periodicity. Rhythmic stacking of facies cycles has been observed in many shallow-marine carbonate successions (Goldhammer et al., 1993; Egenhoff et al., 1999; Lindsay et al., 2006). This aspect is also shown by the red facies in Fig. 5.1b, d, in which thicknesses between different beds of the same facies are constant.

Rhythmicity can be quantified by geostatistical tools, such as the variogram and the transiogram which show oscillations or dampened oscillations called hole-effects (Pyrcz and Deutsch, 2014). By looking at the probability density function (pdf) of facies thicknesses, Ma and Jones (2001) show that, as the coefficient of variation of this pdf decreases, the hole-effect becomes more pronounced. This observation is in agreement with the above remark that rhythmicity is associated with low thickness variability of vertically stacked facies cycles. This also explains why Markov processes cannot create hole-effect transiogram models (Dubrule, 2017), as the corresponding thickness pdf is exponential (coefficient of variation equal to one). On the other hand, some

renewal processes may be able to create dampened hole-effect transiograms, because they offer the possibility to choose a thickness pdf with a lower coefficient of variation (Matheron, 1968). However, the transiograms derived from renewal processes are not always known analytically, and are thus difficult to fit to the observed rhythmicity.

Truncated (Pluri-) Gaussian methods have been successfully used to create facies models (Armstrong et al., 2011), and they have been applied to shallow-marine carbonate reservoirs (Doligez et al., 2011; Amour et al., 2012; Le Blévec et al., 2017b). The contacts between facies are defined by the truncation rule applied to a random Gaussian function, which provides control on facies juxtapositions. However, in its traditional form the method does not incorporate cyclicity and rhythmicity. Le Blévec et al. (2017b) have extended the Pluri-Gaussian method to the modelling of facies asymmetry in vertical successions. They produce asymmetric transition probabilities between facies by introducing a shift in the correlation of two random Gaussian functions as suggested by Armstrong et al. (2011). This is similar to the approaches of Langlais et al. (2008) or Renard and Beucher (2012), but with more flexibility in the resulting facies transiograms. However, the use of this approach to model cyclicity and rhythmicity has not yet been investigated. Pluri-Gaussian Simulations enable the use of hole-effect models (Beucher and Renard, 2016) and may lead to hole-effect facies transiograms that could model rhythmicity.

Although cyclicity and rhythmicity are common features of vertical facies successions, they may have a variable expression laterally, depending on the formative depositional processes and controls. Laterally extensive facies in shallow-marine carbonate strata are generally attributed to external (allogenic) controls that operated over an entire carbonate platform or shelf, such as relative sea-level variations (Goldhammer et al., 1990). Facies of limited lateral extent may be attributed to the nucleation, vertical build-up and lateral shifting of tidal flat islands across a carbonate platform or shelf (Pratt and James, 1986). This mechanism is internal to the dynamics of the carbonate platform depositional system (autogenic) and may generate both vertical and horizontal asymmetry in the stacking of facies if the tidal-flat-island deposits obey Walthers Law (Burgess et al., 2001; Le Blévec et al., 2016). Cyclic and rhythmic facies successions can also be overprinted by diagenetic facies after deposition; for example, hydrothermal dolomite bodies associated with faults and igneous intrusions are observed to cut across shallow-marine

carbonate platform deposits characterized by rhythmic facies cycles (Jacquemyn et al., 2015).

In order to model cross-sections and volumes that exhibit cyclic and rhythmic vertical facies successions but different lateral facies patterns, it is necessary to use different vertical and lateral covariance models. This is possible via the use of separable anisotropic models (Chiles and Delfiner, 2012), although such models have rarely been used for facies modelling (Matheron et al., 1988).

The aim of this paper is to extend the Pluri-Gaussian Simulations approach of Le Blévec et al. (2017b) to model facies cyclicity and rhythmicity in the vertical direction, and a range of appropriate lateral facies patterns using space-time (lateral-vertical) separable covariance models. After presenting the main definitions, the three key aspects of the modelling method and their impact on the transiograms are presented: cyclicity, rhythmicity, separability. A new method for simulating the resulting complex facies architectures is then presented, firstly for unconditional simulations and then for simulations conditioned to data. Finally, the method is applied to a case study from the Triassic Latemar carbonate platform (northern Italy), which has been widely interpreted to show cyclicity and rhythmicity.

5.3 Definitions

5.3.1 Geostatistical Quantification With Transiograms

The random function representing a facies is the indicator function $I(x)$. If the facies i is present at a spatial location x, $I_i(x) = 1$ and if not, $I_i(x) = 0$. In the stationary case, the probability of having a facies at a location x is equal to the first statistical moment or proportion

$$p_i = E[I_i(x)] = Pr\{I_i(x) = 1\}. \tag{5.1}$$

The presence of a facies also depends on the surrounding facies, quantified by the covariance function $c_{ij}(h)$ for two facies i and j. With the stationary assumption, it is assumed that the

covariance depends only on the vector h separating two locations (Chiles and Delfiner, 2012). This paper uses the non-centered indicator covariance

$$c_{ij}(h) = Pr\{I_i(x) = 1, I_j(x+h) = 1\}, \tag{5.2}$$

from which can be derived the transiogram $t_{ij}(h)$, which is the probability to transition from facies i to facies j along a certain vector h

$$t_{ij}(h) = Pr\{I_j(x+h) = 1 | I_i(x) = 1\} = \frac{c_{ij}(h)}{p_i}. \tag{5.3}$$

This transiogram can be asymmetrical, which means that it is different in opposite directions

$$t_{ij}(h) \neq t_{ij}(-h), \tag{5.4}$$

and can thus quantify asymmetrical facies successions (Carle and Fogg, 1996; Le Blévec et al., 2017b). If the transiogram is symmetric, it means there is no polarity in the facies succession and the transitions between facies are equivalent in opposite directions. The transiograms between different facies can be gathered in a transiogram matrix that the simulation method aims to reproduce. For instance, a transition matrix between three facies $(1, 2, 3)$ is

$$t(h) = \begin{bmatrix} t_{11}(h) & t_{12}(h) & t_{13}(h) \\ t_{21}(h) & t_{22}(h) & t_{23}(h) \\ t_{31}(h) & t_{32}(h) & t_{33}(h) \end{bmatrix}. \tag{5.5}$$

The terms on the diagonal are the auto-transiograms and those off-diagonal are the cross-transiograms. With stationary proportions, the tangent at the origin of the auto-transiograms T_{ii} (which is negative) is related to the mean length of the facies i along this direction (Carle and Fogg, 1996). The tangent at the origin (at right) of the cross-transiogram is called the transition rate

$$T_{ij} = t'_{ij}(0). \tag{5.6}$$

Transition rates are of interest when studying asymmetry because they are related to juxtaposition between different facies along the studied direction h. According to Carle and Fogg (1996) (under the stationary assumption) if a facies j tends to follow a facies i in the direction h, rather than preceding it, then

$$T_{ij}\ p_i > \ p_j\ T_{ji}. \tag{5.7}$$

Transition rates are also related to embedded transition probabilities r_{ij} (given the presence of a facies i, the probability that it precedes j in the direction h)

$$r_{ij} = -\frac{T_{ij}}{T_{ii}}, \tag{5.8}$$

which can also be gathered in a transition matrix

$$R = \begin{bmatrix} 0 & r_{12} & r_{13} \\ r_{21} & 0 & r_{23} \\ r_{31} & r_{32} & 0 \end{bmatrix}. \tag{5.9}$$

The diagonal equals zero because embedded Markov chains only record the transitions between different facies. The following important properties of the embedded matrix are used in this paper (Carle and Fogg, 1997)

$$\sum_j r_{ij} = 1, \tag{5.10a}$$

$$\sum_i r_{ij}\ p_i = p_j. \tag{5.10b}$$

In the next section, it is shown how a geostatistical simulation method, the Truncated Gaussian Simulation, relates to these quantities.

5.3.2 Truncated Gaussian Simulations

Truncated Gaussian (TGS) and Pluri-Gaussian (PGS) Simulations (Armstrong et al., 2011) consist of simulating one or several standardized Gaussian random functions that are then truncated into a facies field. Any pair $(Z(x), Z(x+h))$ of a Gaussian random function $Z(x)$

is a bi-Gaussian random vector, with $Z(x)$ and $Z(x+h)$ correlated to each other according to the non-centered covariance function

$$\rho(h) = E[Z(x)\ Z(x+h)]. \tag{5.11}$$

The truncation rule determines which facies is present at location x from the value of the random variables $Z(x)$. For instance, the truncation rule with the case of only two facies 1 and 2 and one Gaussian function (TGS) controls the indicator functions

$$I_1(x) = 1 \text{ and } I_2(x) = 0 \text{ if } \ Z(x) < q, \tag{5.12a}$$

$$I_1(x) = 0 \text{ and } I_2(x) = 1 \text{ if } \ Z(x) \geq q, \tag{5.12b}$$

where q is the threshold of the truncation rule. It is possible to mathematically relate every moment of the facies field to those of the Gaussian function. According to Eq. (5.12a) the proportion of facies one (first order moment) is

$$p_1 = \int_{-\infty}^{q} g(x)\ dx, \tag{5.13}$$

with $g(x)$ the standardized Gaussian pdf. The cross-transiogram (second order moment) between facies one and two is

$$t_{12}(h) = \frac{1}{p_1} \int_{-\infty}^{q} \int_{q}^{\infty} g_{\rho(h)}(x,y)\ dx\ dy, \tag{5.14}$$

where $g_{\rho(h)}$ is the standardized bi-Gaussian probability density with correlation matrix defined by the covariance $\rho(h)$. For $q = 0$ the two facies have same proportion 1/2 and the analytical solution of this bi-Gaussian integral (Lantuéjoul, 2002; Le Blévec et al., 2017b) gives the following auto-transiogram for the two facies

$$t_{11}(h) = t_{22}(h) = \frac{1}{2} + \frac{1}{\pi} \arcsin[\rho(h)], \tag{5.15}$$

Table 5.1: Notations for the truncated Gaussian model

p_i	Facies i proportion
$c_{ij}(h)$	Non centered covariance between facies i and j
$t_{ij}(h)$	Transiogram from facies i to facies j
T_{ij}	Transition rate from facies i to facies j
r_{ij}	Embedded transition rate from facies i to facies j
$\rho(h)$	Covariance of the latent standardized Gaussian function $Z(x)$
q_1, q_2	Thresholds of the Gaussian function $Z_1(x)$ and $Z_2(x)$
$g_{\rho(h)}$	Standardized bi-Gaussian density with correlation $\rho(h)$

and the cross-transiograms

$$t_{12}(h) = t_{21}(h) = \frac{1}{2} - \frac{1}{\pi}\arcsin[\rho(h)]. \tag{5.16}$$

For different thresholds, the transiograms can be derived by numerical integration (Genz, 1992) or expansions into Hermite polynomials (Chiles and Delfiner, 2012).

More than one Gaussian function can also be used. This is the Pluri-Gaussian Simulation (PGS) approach, which provides more flexibility thanks to a larger number of possible truncation rules. In this paper, two Gaussian functions are used, with two thresholds defining three facies $(1, 2, 3)$ (Fig. 5.2)

$$I_1(x) = 1, \quad I_2(x) = 0, \quad I_3(x) = 0 \text{ if } \quad Z_1(x) < q_1, \tag{5.17a}$$

$$I_1(x) = 0, \quad I_2(x) = 1, \quad I_3(x) = 0 \text{ if } \quad Z_1(x) \geq q_1, \quad Z_2(x) < q_2, \tag{5.17b}$$

$$I_1(x) = 0, \quad I_2(x) = 0, \quad I_3(x) = 1 \text{ if } \quad Z_1(x) \geq q_1, \quad Z_2(x) \geq q_2. \tag{5.17c}$$

As for TGS, the corresponding indicator statistical moments can be derived by numerical integration (Genz, 1992). Therefore, the facies transiograms can be derived from the parameters of the Truncated Gaussian model which are summarized in Table 5.1. A more detailed discussion on the link between the Pluri-Gaussian parameters and the transiograms is given in Le Blévec et al. (2017b). This link is used in this paper to match different transiograms and a key objective is to use a covariance $\rho(h)$ such that the transiograms $t_{ij}(h)$ show rhythmicities and asymmetries.

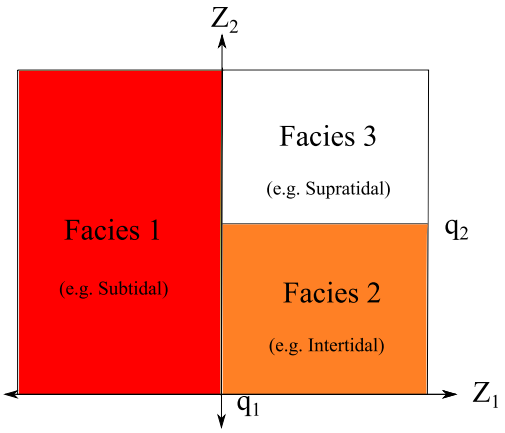

Figure 5.2: Truncation rule used for the cyclical Pluri-Gaussian Simulation. q_1 and q_2 are the thresholds of the Gaussian functions $Z_1(x)$ and $Z_2(x)$

5.3.3 Understanding Cyclicity and Rhythmicity With Transiograms

Wilkinson et al. (1997) define cyclicity as an apparent ordering between facies. Therefore, this definition directly relates to the transition rates (Eq. (5.6)) or the embedded transitions (Eq. (5.8)) that define the juxtapositions between facies. For instance, the perfect cyclic sequences of Fig. 5.1c, d, have the upward embedded transition matrix

$$R = \begin{bmatrix} 0 & 1 & 0 \\ 0 & 0 & 1 \\ 1 & 0 & 0 \end{bmatrix}. \tag{5.18}$$

In other words, every facies transitions into only one other facies upwards ($r_{ij} = 1$). However, in practice such perfect facies successions are rare and the embedded transition probabilities generally do not equal one or zero but have intermediate values. For instance the sequences of Fig. 5.1a, b, show two identical cycles while the other facies transitions are different. A sequence is called acyclic if facies have equal probability of transitioning with the other facies, which would give for three facies the embedded transition matrix

$$R = \begin{bmatrix} 0 & 0.5 & 0.5 \\ 0.5 & 0 & 0.5 \\ 0.5 & 0.5 & 0 \end{bmatrix}. \tag{5.19}$$

One can quantify cyclicity with the probability P_c to observe a given cycle above a given facies, which can be written as the probability of observing the sequence $2-3-1$ above an occurrence of facies one (under the Markov assumption)

$$P_c = r_{12}\ r_{23}\ r_{31}. \tag{5.20}$$

We see that the notion of cyclicity is related to asymmetry by using the closing relations of embedded transition matrices (Eqs. 5.10a and 5.10b)

$$P_c = r_{12}\ (1 - r_{21})\ \frac{p_1 - r_{21}\ p_2}{p_3}. \tag{5.21}$$

The probability P_c increases as r_{12} increases and r_{21} decreases. Therefore, for a sequence with three facies, asymmetry between two facies results in cyclicity. The cyclicity studied here (Fig. 5.1c, d) is such that each facies appear only once per cycle. This is incompatible with symmetric cycles, which are not considered here.

Rhythmicity is defined by the repetition of a facies at constant intervals. This is usually observed on experimental transiograms that show dampened hole-effects (Journel and Froidevaux, 1982; Johnson and Dreiss, 1989; Ma et al., 2009). Rhythmicity cannot be quantified by embedded transition rates as they are independent of facies thicknesses. Rhythmicity can first be understood when studying two facies. If those facies have constant thicknesses, the auto-transiogram varies with a constant wavelength that is equal to the sum of the two facies thicknesses (Jones and Ma, 2001). This is similar with more facies as we can still regard this as the succession of two facies, the one of interest and its complement. This is interesting to consider in combination with cyclicity because the resulting sequences show a constant cycle thickness (Fig. 5.1d). Thicknesses along sequences are not usually constant but can show low variability which results in non-perfect rhythmicity and dampened hole-effects. The method developed here models cyclic and rhythmic sequences, quantified by transiograms.

5.4 The Cyclical Pluri-Gaussian Approach

In this section, the classical Pluri-Gaussian Simulation is extended to render cyclicity (or asymmetry) (Sect. 5.4.1), rhythmicity (Sect. 5.4.2) and separable anisotropy (Sect. 5.4.3). The first two sections (Sect. 5.4.1, Sect. 5.4.2) present results in one dimension and the last section (Sect. 5.4.3) extends them to three dimensions.

5.4.1 Modelling Asymmetrical Facies Juxtapositions in Vertical Successions

A method to simulate asymmetrical facies successions is summarized here (see Le Blévec et al. (2017b) for a detailed treatment). For simplicity two standardized Gaussian random functions with a Cartesian truncation rule are used (Fig. 5.2) as in Eq. (5.17). The correlation between the Gaussian functions $Z_1(x)$ and $Z_2(x)$ is based on the linear model of co-regionalization (Wackernagel, 2003) with a shift α between the Gaussian random functions as proposed by Armstrong et al. (2011)

$$\begin{cases} Z_1(x) = Y_1(x), \\ Z_2(x) = \frac{\rho}{\rho_1(\alpha)} Y_1(x+\alpha) + \sqrt{1 - \frac{\rho^2}{\rho_1(\alpha)^2}} Y_2(x), \end{cases} \tag{5.22}$$

with $Y_1(x)$ and $Y_2(x)$ uncorrelated standardized Gaussian random functions, $\rho_1(h)$ and $\rho_2(h)$ respectively their covariances and ρ the correlation coefficient between $Z_1(x)$ and $Z_2(x)$.

The proportions of the different facies define the thresholds of the truncation rule as in Eq. (5.13), which are also impacted by the correlation coefficient ρ. The resulting transiograms between facies can be computed by Gaussian integral on the facies domain defined by the truncation rule as in Eq. (5.14). Le Blévec et al. (2017b) demonstrate analytically and numerically that these transiograms are asymmetric as in Eqs. (5.4) and (5.7). A sensitivity study is also carried out on the parameters α and ρ showing that the asymmetry can be controlled by varying these two parameters (Le Blévec et al., 2017b). Here, the covariance models $\rho_1(h)$ and $\rho_2(h)$ used for

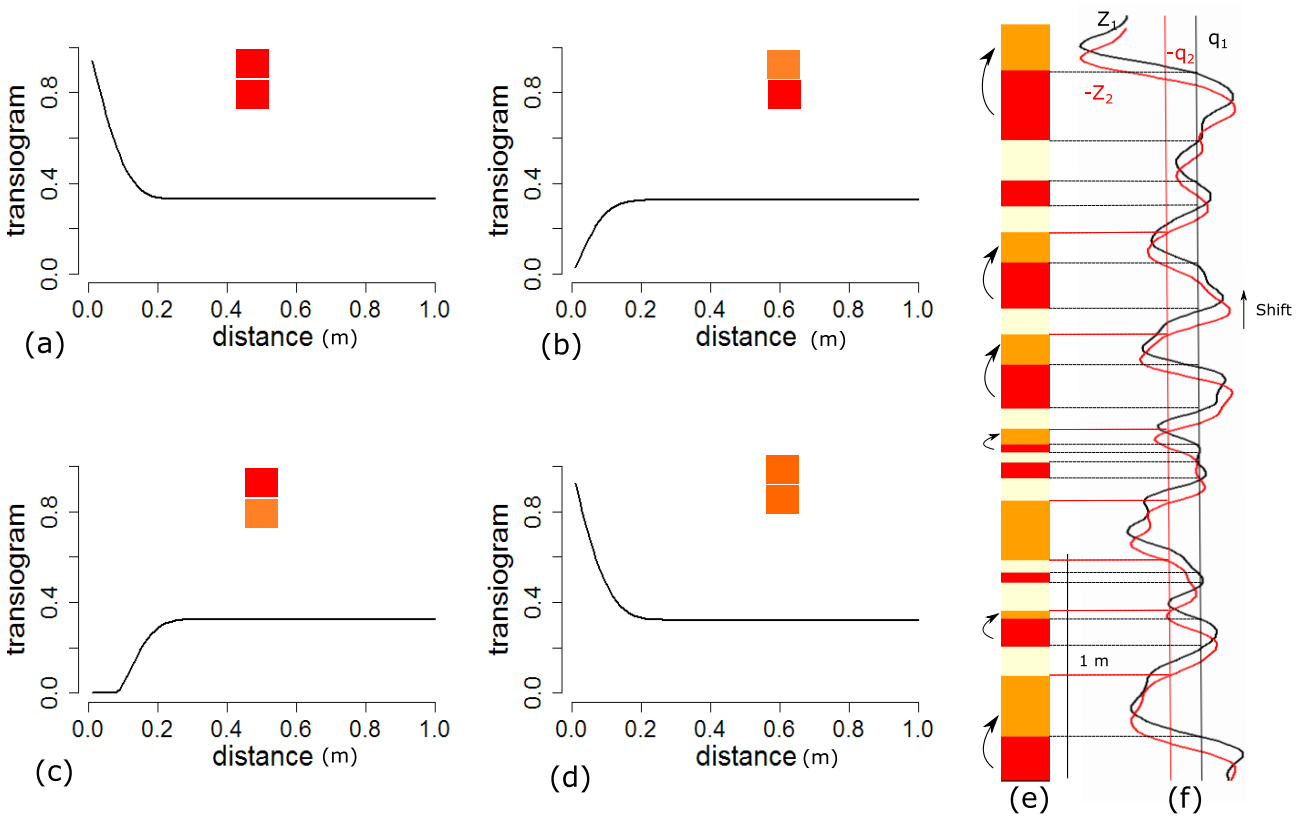

Figure 5.3: One realization (e) with corresponding transiogram matrix model (a-d) and Gaussian functions $Z_1(x)$ and $Z_2(x)$ (f), parameters: $\rho = -0.8$, $r_1 = r_2 = 0.1$, $\alpha = 0.05$, $p_1 = p_2 = p_3$

the Gaussian functions $Y_1(x)$ and $Y_2(x)$ are Gaussian

$$\rho_1(h) = \exp(-\frac{h^2}{r_1^2}), \tag{5.23a}$$

$$\rho_2(h) = \exp(-\frac{h^2}{r_2^2}), \tag{5.23b}$$

with parameters r_1 and r_2 the scale factors of the models. This gives in total four parameters for the method: α, ρ, r_1 and r_2.

An example of a vertical sequence generated with this method and the corresponding facies transiograms is shown in Fig. 5.3. The simulation method of the latent Gaussian functions is given in Sect. 5.5 and the transiograms are computed numerically (Genz, 1992) based on Eq. (5.14). For clarity, only four transiograms instead of nine are shown for the three facies (Fig. 5.3a-d), because the transiograms of the third facies can be directly derived from the transiograms of the other facies. However, in practice, one can work with all the transiograms.

It is clear in the realization shown in Fig. 5.3 that the facies are statistically organized in shallowing-upward cycles as highlighted by the low tangent at the origin of the cross transiogram from intertidal (orange) facies to subtidal (red) facies upwards (Fig. 5.3c). Indeed, this transition is absent along the vertical section while the opposite transition (from subtidal facies to intertidal facies) occurs 6 times. However, the succession is not perfectly cyclic (Fig. 5.3e) because of a low but non-null probability of the subtidal (red) facies to transition upwards directly to the supratidal (white) facies. A high variation of facies thicknesses is also noted, resulting in a non-rhythmic sequence.

5.4.2 Modelling Rhythmicity in Vertical Successions

Using covariance functions with hole-effects for the latent Gaussian function is expected to produce hole-effect facies transiograms. This is verified in this section in which a new indicator transiogram model representing facies rhythmicity is obtained. In one dimension, the cosine function is a valid covariance model (Chiles and Delfiner, 2012) and produces by truncation vertical sequences with a constant cycle thickness. As this is rarely observed, a model in which the oscillations attenuate with distance, called dampened hole-effect (Pyrcz and Deutsch, 2014) gives more flexibility in reproducing cycle thicknesses. Ma and Jones (2001) define the Gaussian cosine covariance as the product of two valid one-dimensional covariance functions

$$\rho(h) = \exp(-\frac{h^2}{r^2}) \ \cos(b\ h). \tag{5.24}$$

This covariance gives dampened oscillations controlled by the two parameters r and b. If the scale factor r tends to infinity, the model is the cosine function. According to Eq. (5.15) the resulting hole-effect transiogram model is

$$t_{11}(h) = \frac{1}{2} + \frac{1}{\pi} \arcsin[\exp(-\frac{h^2}{r^2}) \ \cos(b\ h)]. \tag{5.25}$$

As seen in Fig. 5.4, this transiogram model has the same wavelength as the latent covariance model (Eq. (5.24)) and the attenuation of the oscillations is also similar. Therefore, this

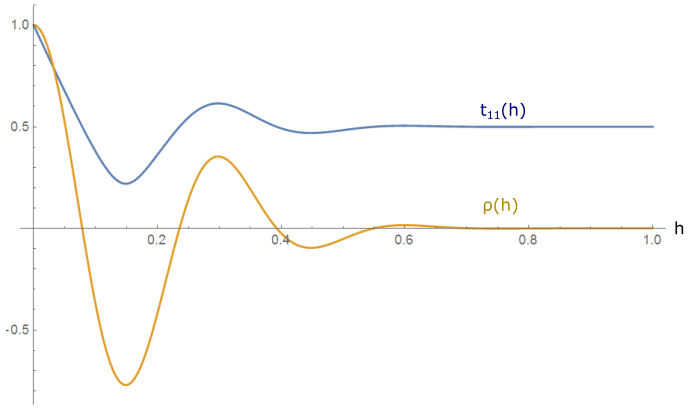

Figure 5.4: Hole-effect on the latent Gaussian field (yellow, Eq. (5.24)) and the resulting hole-effect on the facies transition probability (blue, Eq. (5.25)), with $r_1 = 0.3$ and $b_1 = 20$

transiogram model seems a good candidate to model rhythmicity because of its flexibility.

It is important to remember that Eq. (5.25) is valid only if the threshold is zero, that is the two facies have equal proportions. When this is not the case, the model $t_{11}(h)$ can be numerically computed (Genz, 1992). Figure 5.5 gives the simulation of a vertical sequence with three facies (Fig. 5.5e) and corresponding hole-effect transiograms (Fig. 5.5a-d). The covariances of the two Gaussian random functions have the form of Eq. (5.24) with respective parameters r_1, b_1 and r_2, b_2.

Figure 5.5 clearly shows the effect of rhythmicity on the transiograms and the corresponding realization. The facies cycles are repeated in the vertical succession (Fig. 5.5e) with a rhythmicity controlled by the latent Gaussian functions (Fig. 5.5f). Asymmetry in facies stacking is also added to create a cyclical vertical succession. After developing covariance models in one dimension, it is necessary to expand these models into two and three dimensions while incorporating anisotropy.

5.4.3 Modelling Facies Distributions in Two and Three Dimensions With Separable Anisotropy

In sedimentary deposits, a strong anisotropy is always observed between the vertical direction and the one parallel to stratigraphy. A simple way to represent such anisotropy is to use a

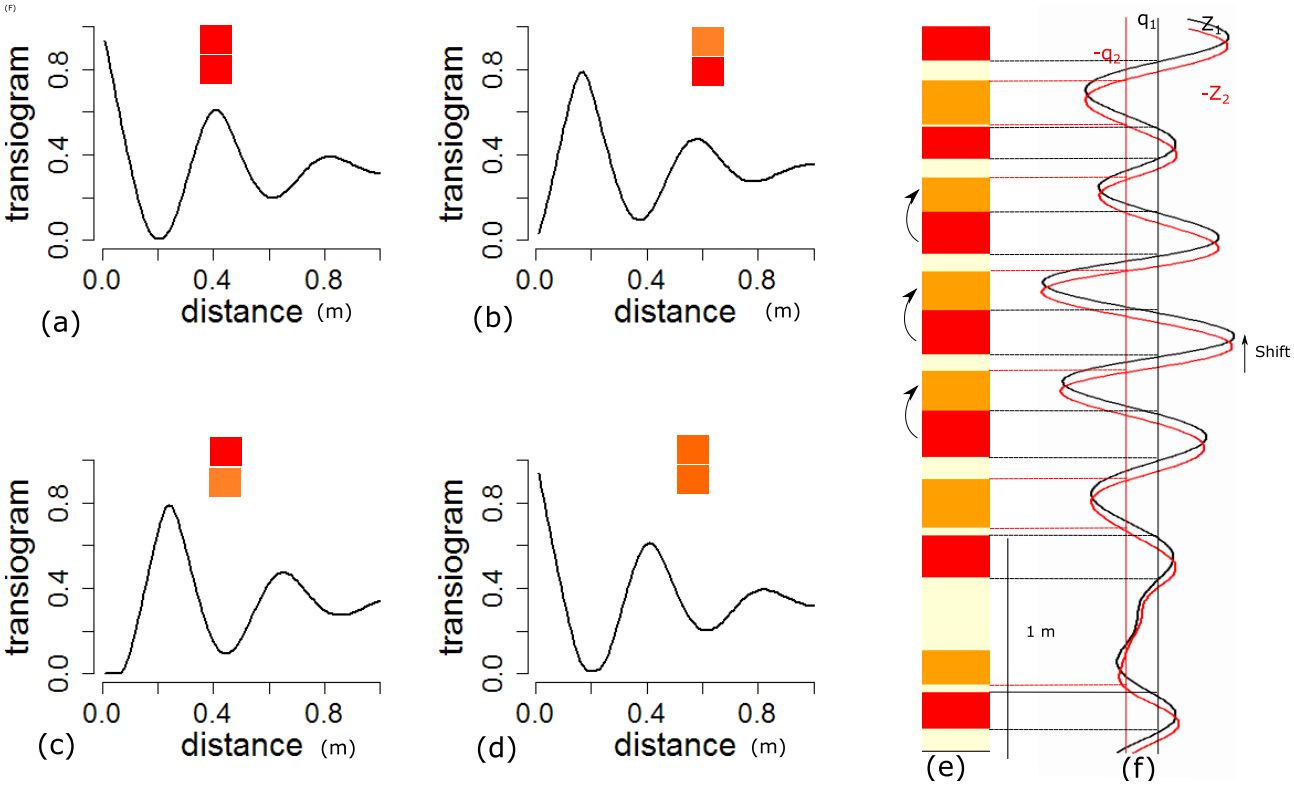

Figure 5.5: One realization (e) with transiogram matrix model (a-d) and latent Gaussian functions (f) with parameters: $\rho = -0.82$, $r_1 = r_2 = 0.6$, $b_1 = 15$, $b_2 = 30$, $\alpha = 0.04$, $p_1 = p_2 = p_3$

separable covariance (Chiles and Delfiner, 2012). A separable covariance model can be built from the product of a covariance in the vertical direction $\rho_v(h_z)$ and a lateral covariance along stratigraphy $\rho_l(h_x, h_y)$

$$\rho(h_x, h_y, h_z) = \rho_l(h_x, h_y)\ \rho_v(h_z). \tag{5.26}$$

As hole-effect usually occurs only in the vertical direction, it is possible to use a dampened hole-effect model for $\rho_v(h_z)$ (Eq. (5.24)) but not for $\rho_l(h_x, h_y)$

$$\rho(h_x, h_y, h_z) = \exp[-\frac{h_x^2}{r_x^2} - \frac{h_y^2}{r_y^2}]\ \exp[-\frac{h_z^2}{r_z^2}]\ \cos[b\ h_z]. \tag{5.27}$$

Along stratigraphy, a standard geometrical anisotropy (which is also separable in this case of a Gaussian covariance) is here used (Chiles and Delfiner, 2012). In an earth modelling software, the lateral direction is usually controlled by the stratigraphic grid. According to Eq. (5.15), the corresponding transiogram model of two facies, after thresholding a single Gaussian at cut

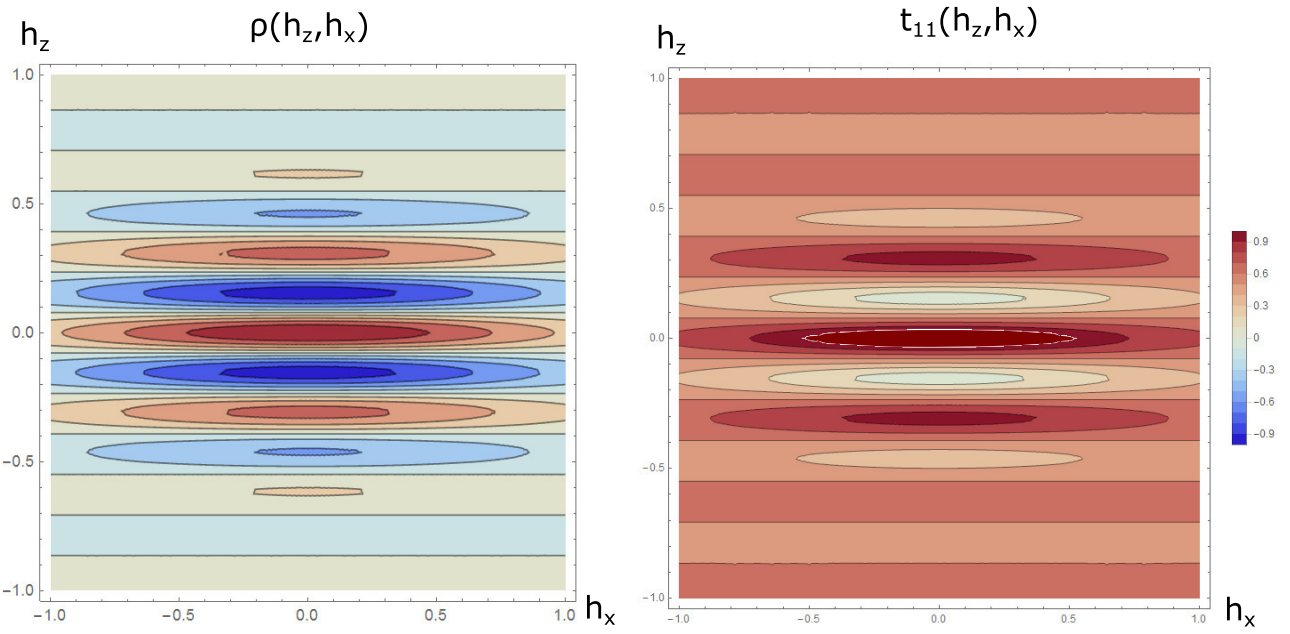

Figure 5.6: Covariance map of the latent Gaussian function (left, Eq. (5.27)) and resulting facies transiogram (right, Eq. (5.28)) in two dimensions with $r_z = 0.5$, $r_x = 1$ and $b = 20$

off 0 is therefore

$$t_{11}(h_x, h_y, h_z) = \frac{1}{2} + \frac{1}{\pi} \arcsin \left[\exp[-\frac{h_x^2}{r_x^2} - \frac{h_y^2}{r_y^2}] \ \exp[-\frac{h_z^2}{r_z^2}] \ \cos[b \ h_z] \right]. \tag{5.28}$$

Equation (5.28) shows that even though the covariance of the latent Gaussian function is separable, the resulting transiogram is not separable. Figure 5.6 displays maps (h_y constant) of the latent Gaussian function covariance and the resulting transiogram which both show a dampened hole-effect in the vertical direction and the absence of a hole-effect along stratigraphy. In intermediate directions, the dampened hole-effect is present but attenuated. Once again, the behavior of the auto-transiogram in two or three dimensions is very similar to the covariance of the latent variable. This suggests that there is about as much flexibility in the transiogram model as in the covariance model.

These transiogram models are valid for two facies in equal proportions but for a more general case, different examples in three dimensions are shown in cross sections with their corresponding transiograms in the vertical direction (Figs. 5.7 and 5.8). The transiograms have been computed by numerical integration (Genz, 1992) (Eq. (5.14)). The parameters for the two Gaussian functions are respectively r_{1_x}, r_{1_y}, r_{1_z} and r_{2_x}, r_{2_y}, r_{2_z}, and vertical hole-effect parameters b_1,

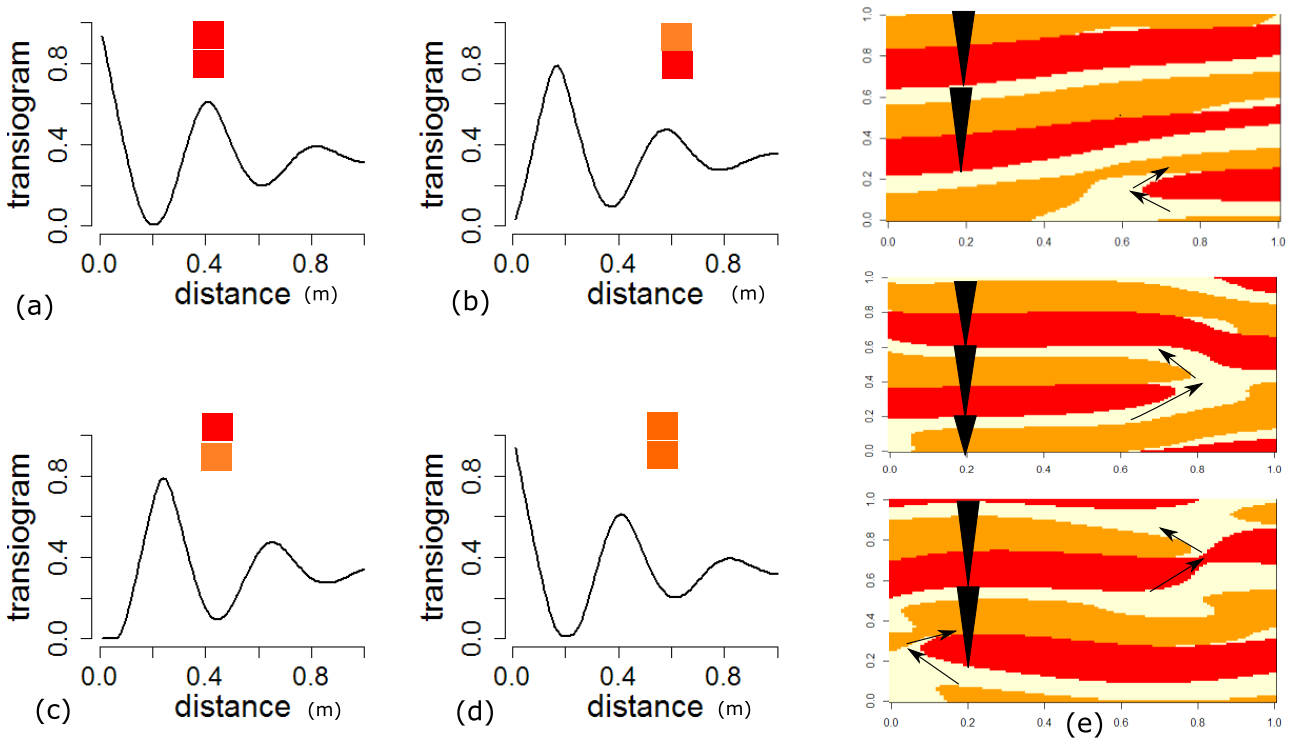

Figure 5.7: Vertical transiogram matrix model (a-d) and three corresponding realizations (e). $\rho = -0.8$, $r_{1_z} = 0.6$, $r_{1_x} = r_{1_y} = 0.4$, $b_1 = 15$, $b_2 = 30$, $r_{2_z} = 0.6$, $r_{2_x} = r_{2_y} = 0.4$, $\alpha = 0.04$, $p_1 = p_2 = p_3$

b_2.

Figure 5.7 shows the combination of asymmetry, rhythmicity and anisotropy in facies distributions in both the realizations and the transiograms. The facies are ordered according to the cycle: subtidal, intertidal and supratidal facies upwards (Fig. 5.7e). The vertical thickness of these cycles is almost constant, confirming the rhythmicity. The different realizations can be interpreted as facies bodies that pinch out laterally or split into different cycles and inter-finger.

Changes in the different parameters can create more complex transiogram models. By using a hole-effect covariance on the second Gaussian function but not on the first, only the orange facies auto-transiogram shows the combined effect of the Gaussian covariance and the hole-effect covariance (Fig. 5.8d). This results in more complex geometries for the orange and white facies that show two combined behaviors. They show thin beds corresponding to the high frequency rhythmicity and thicker beds (Fig. 5.8e) corresponding to a lower frequency. The red facies has a different transiogram from the other facies (Fig. 5.8a), and appears to truncate both of them. Bodies of the red facies can be interpreted either to be erosional or to be diagenetic in origin,

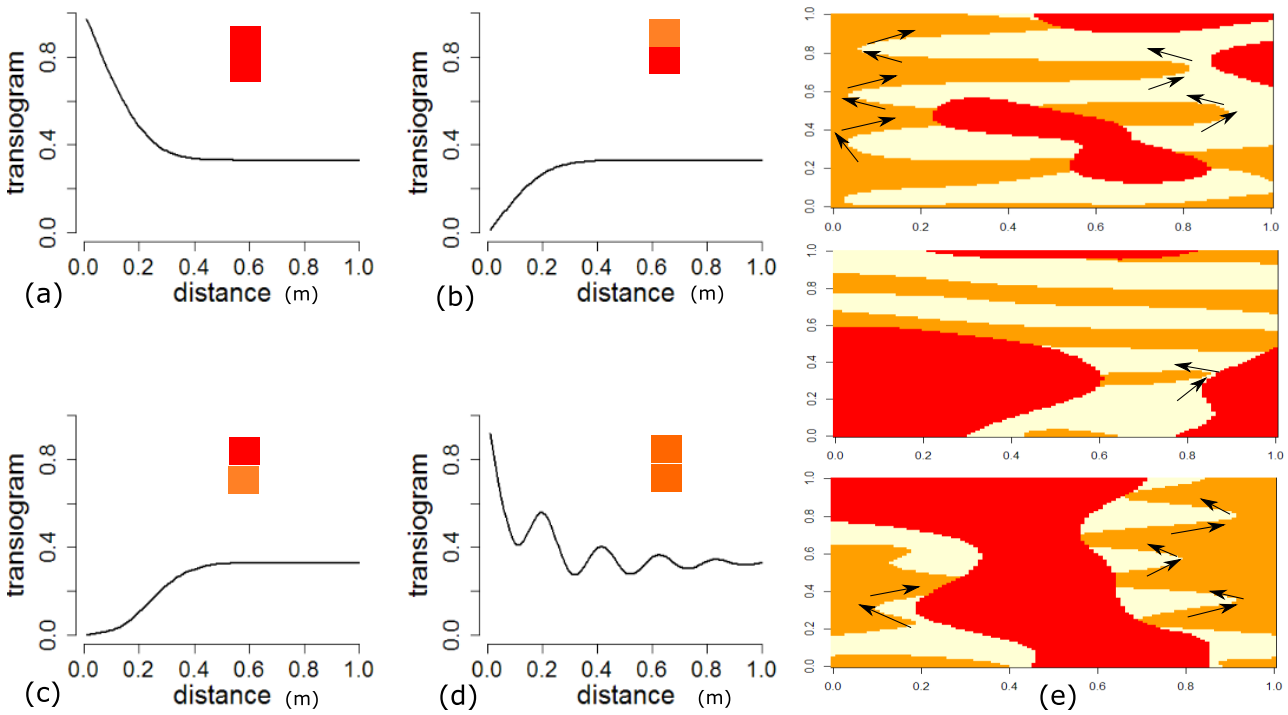

Figure 5.8: Vertical transiogram matrix model (a-d) and three corresponding realizations (e). $\rho = -0.6$, $r_{1_z} = 0.2$, $r_{1_x} = r_{1_y} = 0.4$, $b_1 = 0$, $b_2 = 30$, $r_{2_z} = 0.6$, $r_{2_x} = r_{2_y} = 0.4$, $\alpha = 0.1$, $p_1 = p_2 = p_3$

having formed after deposition. In order to have a better understanding of the geometries generated by this transiogram model (Fig. 5.8), a three dimensional simulation with the same transiograms is also presented in Fig. 5.9. The orange and white facies clearly show vertical rhythmicity with low lateral variability in thickness, consistent with a depositional architecture, while the red (diagenetic) facies truncates them.

Until now Gaussian covariances have been used. However, a more general model could be used in order to control the behavior of the transiogram at the origin. For instance, using the stable covariance model (Chiles and Delfiner, 2012) with a geometrical anisotropy along stratigraphy and separable anisotropy in the vertical direction would give transiograms of the form (for one latent Gaussian function with a threshold at zero)

$$t_{11}(h_x, h_y, h_z) = \frac{1}{2} + \frac{1}{\pi} \arcsin \left[\exp \left[- \left(\sqrt{\frac{h_x^2}{r_x^2} + \frac{h_y^2}{r_y^2}} \right)^{\beta} \right] \exp[-(\frac{h_z}{r_z})^{\gamma}] \, cos[b \, h_z] \right]. \quad (5.29)$$

The smoothness of facies boundaries decreases with the coefficients β and γ ($0 < (\beta, \gamma) \leq 2$).

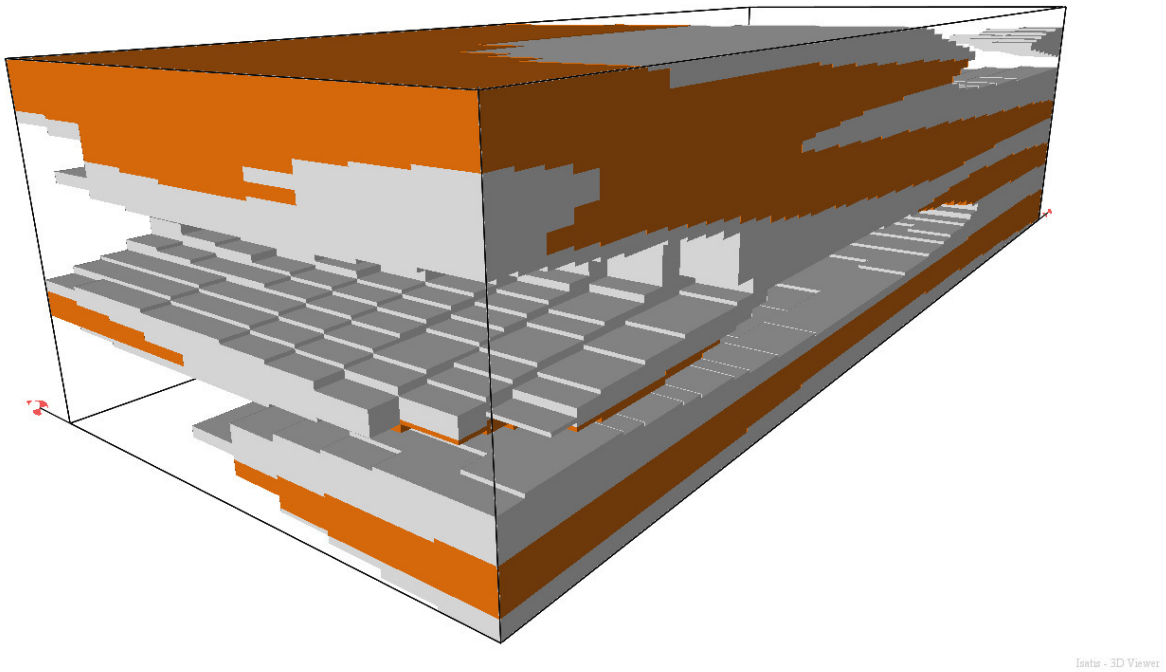

Figure 5.9: Three dimensional simulation with the cyclical PGS obtained with the parameters shown in Fig. 5.8. The void represents the red facies in Fig. 5.8

5.5 Conditional Simulation of the Cyclical Pluri-Gaussian Model

A simple method is here presented to simulate the latent Gaussian functions with covariance presented in Sect. 5.4 and to condition them to the facies observed along the wells.

5.5.1 Unconditional Simulation

The continuous spectral approach developed by Shinozuka (1971) is convenient to build simulations based on separable covariances. The Fourier transform of the covariance model is normalized and used as a probability density function (pdf) to sample frequency vectors ν_k

generating the three dimensional Gaussian function

$$Z(x) = \sqrt{\frac{2}{N}} \sum_{k=1}^{N} cos(< \nu_k, x > + \Phi_k), \tag{5.30}$$

with Φ_k random phases sampled from a uniform pdf between 0 and 2π and $<>$ the scalar product. The resulting function is Gaussian when N tends to infinity (central limit theorem). Based on the knowledge of x, the individual value of $Z(x)$ at each location x can be simulated, which enables the algorithm to be coded in parallel and to be grid-free.

The spectral approach is well suited for a separable covariance as the multi-dimensional Fourier transform of a separable covariance is the product of the Fourier transforms. The three dimensional Fourier transform of a separable covariance model $\rho(h_x, h_y, h_z)$ (Eq. (5.26)) is

$$\mathcal{F}_{\rho(h_x,h_y,h_z)}(\nu_z, \nu_x, \nu_y) = \mathcal{F}_{\rho_v(h_z)}(\nu_z) \;\; \mathcal{F}_{\rho_l(h_x,h_y)}(\nu_x, \nu_y), \tag{5.31}$$

which means the frequencies ν_z in the vertical direction are sampled independently from ν_x and ν_y according to the Fourier transform of their respective covariance models.

In order to simulate the covariance model of Eq. (5.27), the Fourier transforms of the covariance in the vertical direction and the lateral plane must be known (Eq. (5.31)). For the lateral plane, as a Gaussian covariance with geometrical anisotropy is also separable, the two directions h_x and h_y are also sampled independently

$$\mathcal{F}_{\rho_l(h_x,h_y)}(\nu_x, \nu_y) = \mathcal{F}_{\rho_l(h_x)}(\nu_x) \;\; \mathcal{F}_{\rho_l(h_y)}(\nu_y). \tag{5.32}$$

The Fourier transform of a Gaussian covariance is a Gaussian pdf (Chiles and Delfiner, 2012). The Fourier transforms in the lateral direction h_x and h_y are respectively $\mathcal{N}(0, \frac{\sqrt{2}}{r_x})$ and $\mathcal{N}(0, \frac{\sqrt{2}}{r_y})$. In the vertical direction, the Fourier transform of the Gaussian cosine covariance model (Eq. (5.24)) is a bi-modal Gaussian pdf $\mathcal{N}(b, \frac{\sqrt{2}}{r_z}) \cup \mathcal{N}(-b, \frac{\sqrt{2}}{r_z})$ (by modulation of the cosine function)

$$\mathcal{F}_{\rho_v(h_z)}(\nu_z) = \frac{1}{2\ r_z\sqrt{\pi}} \left[\exp(-\frac{1}{4}\frac{(b+\nu_z)^2}{r_z^2}) + \exp(-\frac{1}{4}\frac{(b-\nu_z)^2}{r_z^2}) \right]. \tag{5.33}$$

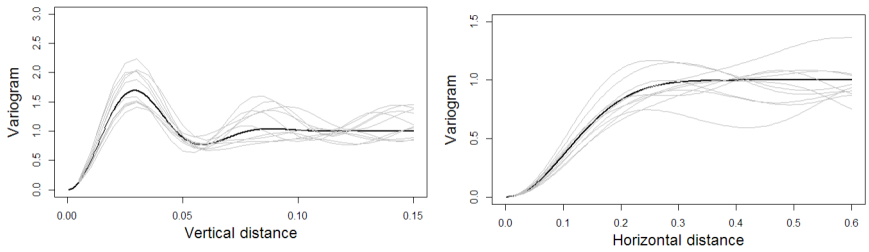

Figure 5.10: Variograms (grey) computed from ten realizations with model (black) and parameters: r_x=0.15, r_z=0.05, $b = 100$, $N = 100$. The simulated grid has $200 * 200$ cells of size $(0.005, 0.005)$

Algorithm 1 describes how to simulate a facies field with such a covariance model. Figure 5.10 shows experimental variograms $(1 - \rho(h))$ of 10 realizations of the simulation of a separable Gaussian cosine covariance in two dimensions (Eq. (5.27)). As expected the covariances of the realizations are centered around the covariance model and represent the hole-effect only in the vertical direction. Some fluctuations of the experimental variograms on the realizations are observed (Fig. 5.10) which are explained in detail by Lantuéjoul (1994) or Emery and Lantuéjoul (2006).

Algorithm 1 Separable Gaussian cosine simulation in three dimensions

1: $\phi \longleftarrow$ Generate N samples in $\mathcal{U}(0, 2\pi)$
2: $\nu_z \longleftarrow$ Generate N samples in $\mathcal{N}(b, \sqrt{2}/r_z)$
3: $\nu_x \longleftarrow$ Generate N samples in $\mathcal{N}(0, \sqrt{2}/r_x)$
4: $\nu_y \longleftarrow$ Generate N samples in $\mathcal{N}(0, \sqrt{2}/r_y)$
5: $i \longleftarrow$ Generate N samples in $(-1, 1)$ to be multiplied with ν_z to sample from $\mathcal{N}(b, \frac{\sqrt{2}}{r_z}) \cup \mathcal{N}(-b, \frac{\sqrt{2}}{r_z})$
6: For every location (x, y, z): apply Eq. (5.30)
7: Truncate according to truncation diagram

The spectral approach can also be used to simulate a stable separable covariance model (Eq. (5.29)). The Fourier transform of a stable covariance is a stable spectral pdf with stability and scale parameters α and r, skewness and location 0 (Chiles and Delfiner, 2012). Therefore, to simulate this covariance, one can use Algorithm 1 by replacing the Gaussian distributions with the stable distributions. These simulations are unconditional, and they must now be conditioned to facies data observed at specific locations in the simulated volume.

5.5.2 Conditioning the Gaussian Simulation to Facies Data

Some methods already exist for conditioning Pluri-Gaussian Simulations to hard data (Emery and Lantuéjoul, 2006; Chiles and Delfiner, 2012). This section summarizes the main steps and proposes improvements in the case of separable covariances. The truncation rule defines intervals of the Gaussian function corresponding to each facies. At data locations x_i, the observed facies constrain the Gaussian random functions with the following inequalities

$$Z_1(x_i) < q_1 \quad \text{if} \quad I_1(x_i) = 1, \tag{5.34a}$$

$$Z_1(x_i) \geq q_1, \quad Z_2(x_i) < q_2 \quad \text{if} \quad I_2(x_i) = 1, \tag{5.34b}$$

$$Z_1(x_i) \geq q_1, \quad Z_2(x_i) \geq q_2 \quad \text{if} \quad I_3(x_i) = 1, \tag{5.34c}$$

according to the truncation diagram (Fig. 5.2). The conditional simulation is usually performed in three steps (Chiles and Delfiner, 2012), (i) unconditional simulation, (ii) Gibbs sampling at data locations and (iii) conditioning by kriging of the mismatch at data locations. Here, the conditioning is broken down in more steps for optimization purposes:

1. Unconditional uncorrelated simulations $Y_1^u(x)$ and $Y_2^u(x)$ are performed over the domain as in Sect. 5.5.1.

2. Joint local conditional simulation of $Z_1(x_i)$ and $Z_2(x_i)$ is carried out only at data locations x_i using Gibbs sampling such that Eq. (5.34) is respected (Freulon and de Fouquet, 1993).

3. Back-transform of correlated $Z_1(x_i)$ and $Z_2(x_i)$ into uncorrelated $Y_1(x_i)$ and $Y_2(x_i)$ at data location according to Eq. (5.22).

4. Two separate simple kriging $R_1(x)$ and $R_2(x)$ based on the mismatch at data locations

$$R_1(x_i) = Y_1(x_i) - Y_1^u(x_i), \tag{5.35a}$$

$$R_2(x_i) = Y_2(x_i) - Y_2^u(x_i), \tag{5.35b}$$

are performed (Chiles and Delfiner, 2012)

$$R_1(x) = \sum_i \lambda_i^1(x)\ R_1(x_i), \tag{5.36a}$$

$$R_2(x) = \sum_i \lambda_i^2(x)\ R_2(x_i), \tag{5.36b}$$

with $\lambda_i^1(x)$ and $\lambda_i^2(x)$ the kriging weights (Chiles and Delfiner, 2012). The conditional uncorrelated Gaussian random functions Y_1 and Y_2 at every location x are finally obtained by

$$Y_1(x) = Y_1^u(x) + R_1(x), \tag{5.37a}$$

$$Y_2(x) = Y_2^u(x) + R_2(x). \tag{5.37b}$$

5. Transform conditioned Y_1 and Y_2 into conditioned and correlated Z_1 and Z_2 according to Eq. (5.22).

The Gibbs sampling at data locations is not described here. Any algorithm can be chosen (Emery et al., 2014) and applied with the desired covariance model to simulate the values of $Z(x_i)$ at the data locations. Because Z_1^u and Z_2^u are co-simulated, the covariance matrix used for the Gibbs sampling is made of the cross-covariances between Z_1^u and Z_2^u, given in more details in Le Blévec et al. (2017b). As this covariance matrix can be singular, it is advised to perform a Gibbs sampling that does not involve its inversion (Dubrule, 1983; Emery et al., 2014).

The kriging of the difference (Eqs. (5.36a) and (5.36b)) can be optimized when using a separable covariance such as the model of Eq. (5.26) and if the wells are strictly vertical. This is important because kriging over the whole domain is computationally expensive, and can make simulation prohibitively slow. The simple kriging is optimized thanks to the well known screening properties of separable covariances (Matheron et al., 1988; Chiles and Delfiner, 2012). Performing kriging in the uncorrelated space of the Y_i allows firstly a reduction of the size of the covariance matrix to invert (and the stability of the inversion) for finding the weights λ_i^1 and λ_i^2. Secondly, it ensures that the covariance is separable (and thus its screening property)

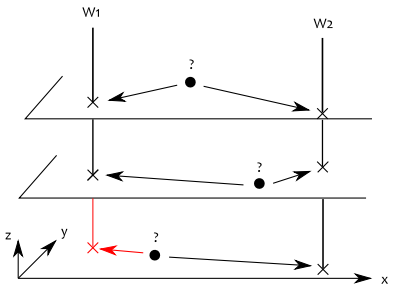

Figure 5.11: The screening effect for simple kriging applied on two wells W_1 and W_2 to estimate three locations on three different horizontal planes with one extended well (red)

which is not the case for the covariance of Z_2.

With a separable covariance model such as that of Eq. (5.26), the weights $\lambda_i(x)$ associated with data located on different lateral planes from that of the estimated location x are equal to zero (Chiles and Delfiner, 2012). This means that the estimation at a given location only depends on the data at the same horizontal level, and the number of kriging weights therefore equals the number of wells intersecting this horizontal level, as shown in Fig. 5.11. Assuming all wells are vertical and have the same length, the number of weights for every kriged point is therefore simply the number of wells. If this is not the case, for instance because some vertical wells do not penetrate a particular level, it is convenient to artificially extend them by an unconditional simulation with Gibbs sampling at step (ii) (Fig. 5.11), so that the geometrical configuration of the data points remains the same at all levels. Therefore, the weights are the same for every horizontal plane and the dual form of two-dimensional kriging may be used, in which the data covariance matrix is inverted only once (Dubrule, 1983; Chiles and Delfiner, 2012). This enables rapid and efficient kriging. An example of conditional simulation with this method is given in the following section.

5.6 Case study: the Latemar Carbonate Platform, Northern Italy

The Triassic Latemar carbonate platform is superbly exposed in northern Italy and has been chosen as a case study as it provides well-documented examples of facies cyclicity with rhythmic-

ity and asymmetry in shallow-marine peritidal strata (Goldhammer et al., 1990). Rhythmicity has been quantified along a vertical sequence through the entire platform succession using spectral analysis, in order to understand the potential expression of orbital forcing (Milankovitch cycles) on platform growth (Hinnov and Goldhammer, 1991; Preto et al., 2001). However, few studies describe sequences in different parts of the platform with the aim of performing facies modelling. Here, the dataset of Peterhänsel and Egenhoff (2008) (Upper Cyclic Facies stratigraphic interval) is used to evaluate and model asymmetrical (upward-shallowing) facies cycles and facies rhythmicity near the topographically high platform margin (Cimon Latemar) and in deeper lagoonal deposits of the platform interior (Cimon Forcellone). Peterhänsel and Egenhoff (2008) describe five microfacies based on thin sections: peloidal packstone to wackestone (facies one), algae peloidal packstone (facies two), fenestral packstone to wackestone (facies three), packstone to grainstone (facies four), diagenetically overprinted grainstone to packstone (facies five). To illustrate our geostatistical method, these microfacies are re-grouped into three main environments of deposition: subtidal (facies one), intertidal (facies two and three), supratidal storm deposits (facies four and five). The next paragraph provides a quantitative analysis of the variations of these three facies.

5.6.1 Qualitative and Quantitative Study of the Case-study Dataset

As illustrated by Fig. 5.12, the eight vertical logs show a high number of facies transitions. The asymmetry is clear as the subtidal facies (red) tends to be on top of the supratidal (white) facies. However, complete upward-shallowing facies cycles, containing subtidal, intertidal and supratidal deposits, occur only 24 times, while there are 56 incomplete cycles in the eight logs, which means that the sequences have some cyclic features. The subtidal facies appears to show regular spacing between beds within some wells (Fig. 5.12, in logs N8 and N16), which would suggest a rhythmicity of this facies. This is not the case for the intertidal and supratidal facies, which show very different spacings between the beds (Fig. 5.12).

All this information can be verified in the experimental transiograms computed on the logs (Fig. 13, grey points). A dampened hole-effect is observable on the auto-transiogram of the

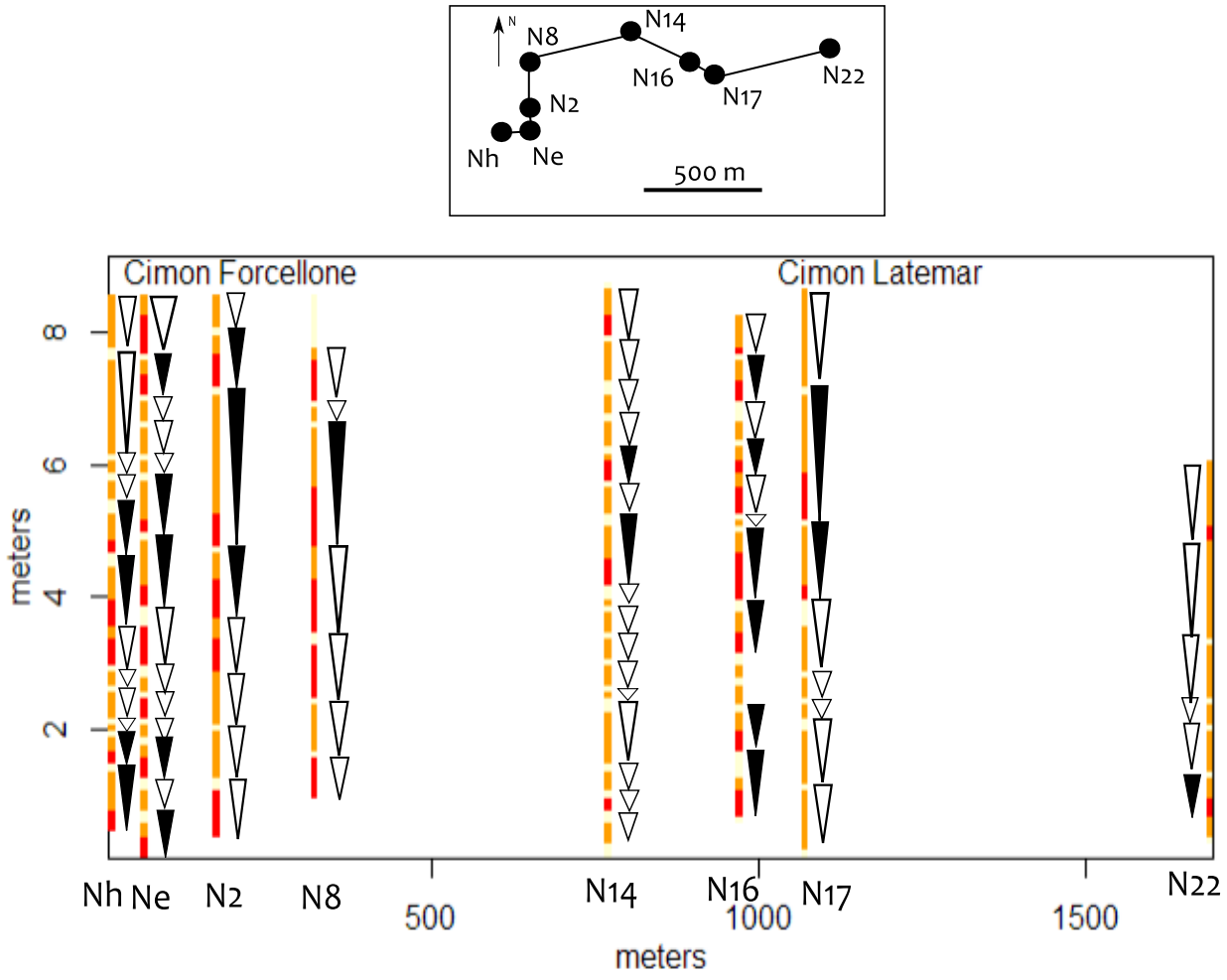

Figure 5.12: Logs through the Upper Cyclic Facies interval of the Latemar carbonate platform (Peterhänsel and Egenhoff, 2008) subtidal (red), intertidal (yellow) and supratidal (white)

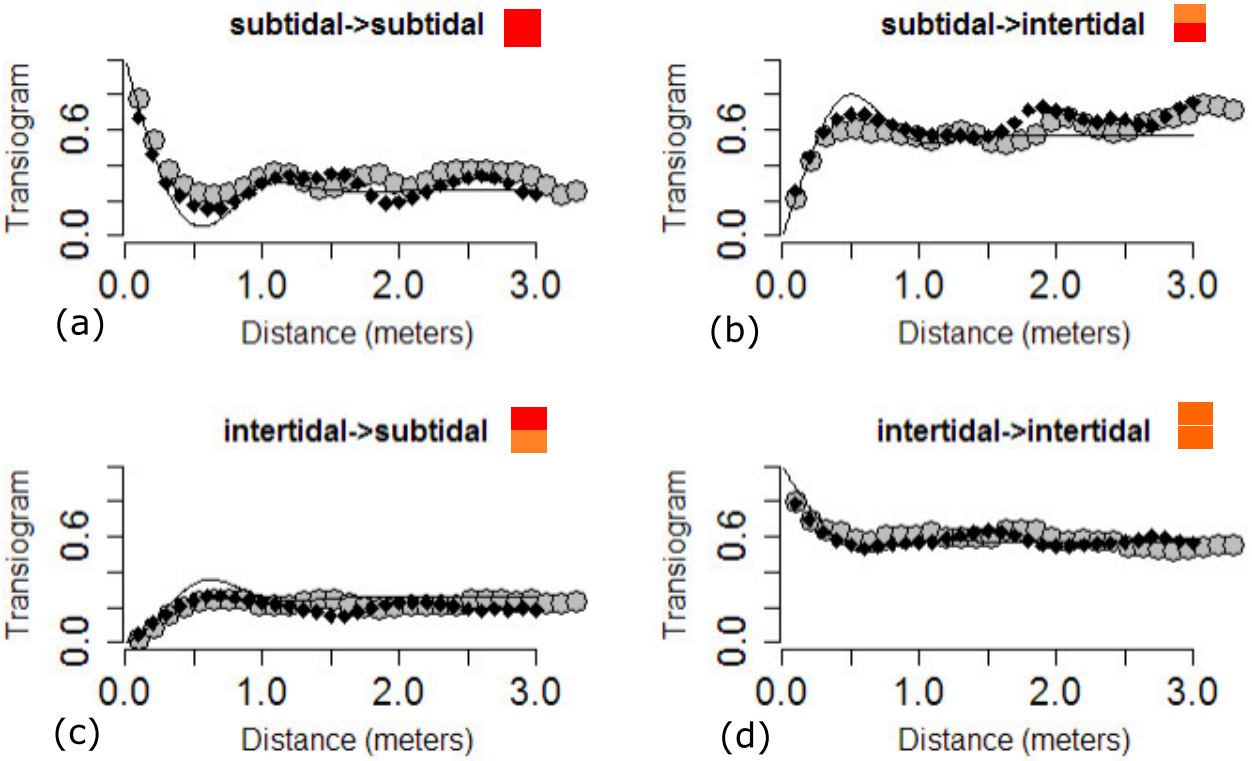

Figure 5.13: (a-d) Experimental transiograms (grey points), model (black line) and realization (black diamonds) after simulation with parameters in Table 5.2

subtidal deposits (Fig. 5.13a). The tangent at the origin of the cross-transiogram of intertidal deposits overlain by subtidal deposits (Fig. 5.13) is low, showing that this transition is rare. More precisely, $T_{12} = 2.06$ and $T_{21} = 0.19$ which means according to Eq. (5.7) that the intertidal facies is four times more likely to overlie the subtidal facies than to underlie it.

5.6.2 Inference of the Co-regionalization Model

As seen in Fig. 5.13a, the subtidal deposit auto-transiogram shows a dampened hole-effect. In order to model this hole-effect properly, it is easier to derive it from only one covariance rather than a combination of two covariances. Therefore, the truncation rule of Fig. 5.2 where the subtidal facies is defined by only one Gaussian function, is chosen. The use of more complex truncation rules is discussed in Sect. 5.7.1.

The parameters of the Pluri-Gaussian model are determined using the procedure described in Le Blévec et al. (2017b). Only the auto- and cross-transiograms of two of the three facies

are necessary to determine the parameters of the model, as the transiograms for the third facies are derived from those of the two other facies. A trial and error procedure is here chosen for determining the parameters, as this gives the possibility to incorporate conceptual knowledge. For instance, as it is known that rhythmicity and asymmetry occur, it is important to incorporate these features during the model construction, which would be difficult with an automatic fitting procedure.

The covariance of the first Gaussian function $\rho_1(h)$ is used to describe the transiogram of the subtidal facies. The Gaussian cosine model (Eq. (5.24)) gives an appropriate fit although the oscillations observed on the logs seem less pronounced (Fig. 5.13a). This fit could be improved by using a more complex covariance model, as discussed in Sect. 5.7.2. Then, the correlation coefficient ρ and the shift α can be chosen to fit the transition rates between the subtidal and intertidal facies. Here the asymmetry (Eq. (5.7)) is clear, because the probability of intertidal facies overlying subtidal facies is four times higher that of the opposite. Therefore, the shift α is equal to the size of one vertical cell and the correlation coefficient ρ is rather high (-0.6) which allows the model to match these transition rates. The shift is strictly vertical because no information on a possible lateral asymmetry is available (this topic is further discussed in Sect. 5.7.3). Finally the covariance of the second Gaussian functions $\rho_2(h)$ determines the transiogram of intertidal facies. A rhythmic covariance is not necessary here, as the transiogram does not show a clear hole-effect. There is not enough information to determine the lateral scale factors of the covariance directly from the data. Therefore, they are derived from visual comparison of the realizations with the outcrop facies panel interpreted between the vertical logs by Peterhänsel and Egenhoff (2008) and are chosen to be isotropic (in the lateral plane). Finally, the thresholds q_1 and q_2 of the Gaussian functions are determined according to the proportions of the facies and the correlation coefficient ρ between the two Gaussian random functions (Armstrong et al., 2011). The parameters are summarized in Table 5.2.

Vertically, a Gaussian cosine covariance is chosen but laterally an exponential covariance (Chiles and Delfiner, 2012) is preferred. A Gaussian or cubic covariance in the lateral direction may lead to a singular kriging system for the conditioning step as the lateral scale factor is large (Sect. 5.5.2). A stable covariance with a power close to two could also be chosen to obtain a

Table 5.2: Parameters of the Pluri-Gaussian Simulation for the Latemar platform

(q_1, q_2)	$(-0.65, 0.41)$	Thresholds for the two Gaussian functions
ρ	-0.6	Correlation between Gaussian functions
α	$0.1m$	Vertical shift between Gaussian functions
$(r_{1_x}, r_{1_y}, r_{1_z})$	$(500m, 500m, 0.8m)$	Scale factors of the first Gaussian covariance
$(r_{2_x}, r_{2_y}, r_{2_z})$	$(500m, 500m, 0.4m)$	Scale factors of the second Gaussian covariance
(b_1, b_2)	$(5m^{-1}, 0m^{-1})$	Vertical frequencies of the two covariances

smoother model than that obtained with the exponential.

5.6.3 Simulation Results

The cell sizes of the grid are 0.1 meters vertically and 10 meters laterally in both North and East directions, which gives approximately 800,000 cells. The simulation takes approximately one minute to run with a standard Intel processor i7, but it could be much faster by performing the unconditional simulation with the spectral method in parallel, which is the longest computational step. The conditioning by kriging every surface independently, as described in Sect. 5.5.2, is almost instantaneous. One realization of the field is shown in Fig. 5.14.

The visual aspect of the simulation is granular due to the exponential covariance model used in the lateral plane. Visually, the subtidal (red) facies tends to lie on top of the supratidal (white) facies and rhythmicity is confirmed by the regular thickness between two subtidal (red) facies bodies. The transiograms of the wells and the transiograms computed on one realization are compared in Fig. 5.13. The sills derived from simulation (black diamonds in Fig. 5.13) are accurate, which means that the facies proportions match those in the wells. The tangent at the origin of the auto-transiograms is appropriately fitted, which means the average thicknesses of different facies bodies honours the well data. The tangent at the origin of the cross-transiograms matches the transition rates of the wells ($T_{12} = 2.1$ and $T_{21} = 0.19$) which means the asymmetry and cyclicity are respected. The hole-effect in the realization transiogram is less pronounced than the one used for the theoretical model, but is closer to the one observed at the wells (grey circles in Fig. 5.13). This might be due to the conditioning of the realization to the wells, where

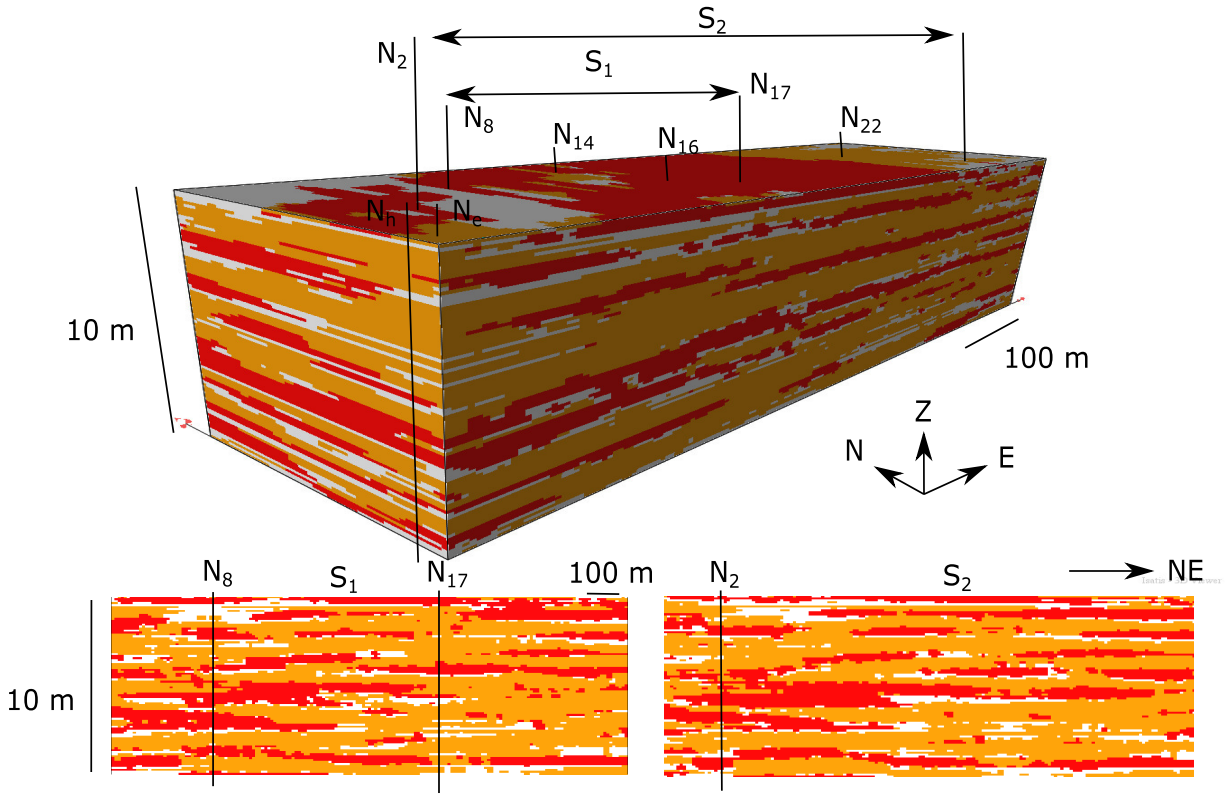

Figure 5.14: One realization of the Latemar facies field from Peterhänsel and Egenhoff (2008) data (Fig. 5.12), and two cross-sections obtained with the parameters summarized in Table 5.2

the experimental transiograms show less pronounced oscillations (black lines in Fig. 5.13).

5.7 Discussion

In order to illustrate the method, standard parameters have been chosen so far for both the synthetic examples and the case study. However, some parameters such as the truncation rule, the covariance model, or the shift can be changed to adjust to different geological environments.

5.7.1 The Truncation Rule

Choosing the Truncation Rule

The same truncation rule has been applied through the paper (Fig. 5.2) with the subtidal facies defined by the first Gaussian function and the two others by both Gaussian functions. This

has implications for the geometries of individual facies bodies and for facies relationships. The facies defined by the first Gaussian function erodes the two other facies (e.g., Fig. 5.8e), which means that bodies of these facies can have very different geometries from those of the other facies. This behavior can be reduced by increasing the correlation ρ between the two Gaussian functions $Z_1(x)$ and $Z_2(x)$.

The truncation rule affects not only the facies transiograms but also higher order statistical moments, which can have an impact on connectivity (Beucher and Renard, 2016). However, these moments are not known analytically and so are difficult to use for defining the truncation rule. It is recommended that the earth modeller tries different truncation rules and inspects the visual aspect of simulations so that it matches with his or her conceptual knowledge.

Adapting the Truncation Rule for More Facies

In this paper, only three facies have been used to illustrate the method. Two methods for generalizing the truncation rule to more facies are found in the literature: either the truncation is made more complex (Galli et al., 2006) or the number of Gaussian functions is increased (Maleki et al., 2016). The first method is probably too limited to represent a large number of transition rates between facies, while the second one should be able to model all transition rates (but the number of parameters would be very high). The choice between the two methods should depend on the case study and further work on this topic is required. It should also be noted that some methods that create automatic truncation rules have been developed (Deutsch and Deutsch, 2014; Astrakova et al., 2015). It would be interesting to generalize these methods by incorporating the shift between the Gaussian functions in order to match asymmetric transition probabilities.

5.7.2 Elaborating More Complex Hole-effect Models

The vertical hole-effect model used in this paper is made of two parameters r_z and b (Eq. (5.24)) which provides some flexibility to match observed rhythmicity. However, the case study shows

that the observed transiograms can be even more complex (Fig. 5.13) and two parameters might not be sufficient to represent them. The covariance model could be modified to incorporate more than one structure (Chiles and Delfiner, 2012). For instance a Gaussian covariance or a cosine covariance can be added to the Gaussian cosine model (Eq. (5.24)).

5.7.3 Walther's Law

The method developed in this paper models cyclicity only in the vertical direction, which is consistent with observations of most outcrop and subsurface data. However Walther's Law suggests that the transitions between facies should be equivalent laterally and vertically if no erosion is present (Middleton, 1973). This means that the facies ordering could be similar and the transition rates proportional as in Markov Chains methods (Doveton, 1994; Purkis et al., 2012). Thus asymmetry could also be observed laterally. Since the shift is actually a three-dimensional vector, it is possible to model such patterns with the presented method by defining a non-vertical vectorial shift between the Gaussian functions (Eq. (5.22)), such that the asymmetry is also lateral (Le Blévec et al., 2016).

This choice will depend on the depositional environments, processes, controls, and scale to be modelled. These aspects are typically interpreted with reference to an underlying conceptual model, such as those for allocyclically and autocyclically generated facies cycles in peritidal carbonate strata (Pratt and James, 1986; Goldhammer et al., 1990). The facies architectures to be modelled are also scale dependent. Environments of deposition generally have large lateral extents (1 - 10 km), such that few lateral transitions between them are observed at reservoir (1 - 10 km) and inter-well (<1 km) scales (Sena and John, 2013), which limits the expression of lateral ordering of depositional environments. At smaller scales, the lateral transitions between lithofacies within depositional environments (or facies associations) may be different from the vertical transitions (Hönig and John, 2015) because of erosion or lateral changes in palaeotopography. The resulting lithofacies distributions may be highly variable, potentially reflecting a facies migration that is well-ordered and obeys Walther's Law as one end member (Obermaier et al., 2015) or more complex and less ordered facies mosaics as the opposite end

member (Wilkinson et al., 1997). The choice of appropriate conceptual model at the scale of depositional environments (facies association) or lithofacies must be made by the earth modeler in collaboration with the geologist, and then used to govern the selection of parameters of the model.

5.8 Conclusion

While cyclicity and rhythmicity are commonly observed in facies architectures, few existing geostatistical algorithms can model both patterns in an efficient manner. By addressing this issue, the method developed here is useful for modelling carbonate or shallow-marine clastic reservoirs that contain such cyclical facies successions. Broadly speaking, cyclicity and rhythmicity are quantified by facies transiograms that are computed from data (e.g., vertical facies successions) and fitted with an advanced truncated Pluri-Gaussian model for performing three dimensional simulations.

The model used for the latent Gaussian functions is the linear model of co-regionalization with a spatial shift, which creates the asymmetric cycles. The covariance of the Gaussian functions presents a dampened hole-effect, which captures the rhythmicity. As this hole-effect is generally observed only in the vertical direction, a separable covariance model, which is the product of a lateral and a vertical covariance is used so that no rhythmicity is modelled laterally along the stratigraphy. The space-time separable covariance is simulated readily by the continuous spectral method. The numerical properties of separable covariance allows rapid and efficient conditioning to data via kriging of every horizontal surface independently. The procedure has been applied successfully to model a carbonate platform environment that shows cyclicity and rhythmicity in facies architecture.

Chapter 6

Geostatistical Earth Modelling of Cyclic Depositional Facies and Diagenesis

6.1 Abstract

In siliciclastic and carbonate reservoirs, depositional facies are often described as being organized in cyclic successions that are overprinted by diagenesis. Most reservoir modelling workflows are not able to reproduce stochastically such patterns. Herein, a novel geostatistical method is developed to model depositional facies architectures that are rhythmic and cyclic, together with superimposed diagenetic facies.

The method uses truncated Pluri-Gaussian random functions constrained by transiograms. Cyclicity is defined as an asymmetric ordering between facies, and its direction is given by a three-dimensional vector, called shift. This method is illustrated on two case studies. Outcrop data of the Triassic Latemar carbonate platform, northern Italy, are used to model shallowing-upward facies cycles in the vertical direction. A satellite image of the modern Bermuda platform interior is used to model facies cycles in the windward-to-leeward lateral direction.

As depositional facies architectures are modelled using two Gaussian random functions, a third Gaussian random function is added to model diagenesis. Thereby, depositional and diagenetic facies can exhibit spatial asymmetric relations. The method is applied in two regions of the Latemar carbonate platform that experience two different types of diagenetic transformation: syn-depositional dolomite formation, and post-depositional fracture-related diagenesis. The method can also incorporate proportion curves to model non-stationary facies proportions. This is illustrated in Cretaceous shallow-marine sandstones and mudstones, Book Cliffs, Utah, for which cyclic facies and diagenetic patterns are constrained by embedded transition probabilities.

6.2 Introduction

In reservoir modelling applications, an important step is the representation of three-dimensional facies architecture and the quantification of associated uncertainty. The Earth modelling community routinely uses geostatistical methods to reach this goal (Koltermann and Gorelick, 1996; Alabert and Modot, 1992; Pyrcz and Deutsch, 2014). However, the commonly-used geostatistical approaches have some significant limitations. For instance, geostatistical models often show the same facies successions in the upward as in the downward direction, which does not allow the representation of classic geological features such as facies cyclicity or certain types of syn-depositional diagenesis.

modelling Cyclicity and Rhythmicity

Depositional facies in vertical successions exhibit extensive cyclicity and rhythmicity (Strasser, 1988; Goldhammer et al., 1990; Wilkinson et al., 1997; Lindsay et al., 2006; Burgess, 2016). These features are defined respectively as facies ordering (Gingerich, 1969; Hattori, 1976) and repetition of facies at intervals of constant thickness (De Boer and Wonders, 1984; House, 1985). Their origin is attributed to various controls, including relative sea level oscillations (e.g., Grotzinger, 1986b), local tectonic activity (e.g., Cisne, 1986) and autogenic mechanisms. These different origins may lead to cycles and rhythms of differing lateral extent and stacking

patterns, which should be reproduced by the modelling method. For example, facies cycles are commonly interpreted at reservoir scale with reference to sequence stratigraphic models, implying that they are laterally extensive (e.g., Goldhammer et al., 1990), although over such distances, some facies cycles are documented to pinch out (e.g., Egenhoff et al., 1999). In order to represent these diverse facies cycles and rhythms, reservoir-wide deterministic correlations may not be appropriate.

Diverse facies distributions are modelled by geostatistical methods, but their current implementation cannot generate facies cycles and rhythms simultaneously. For example, cyclicity quantification is possible with Markov Chain analysis (Gingerich, 1969; Hattori, 1976), but the method is originally limited to one dimension. It was later improved by Carle and Fogg (1996) who model cyclic three dimensional Earth models thanks to asymmetric transiograms. However, the method does not incorporate rhythmicity, because the transiogram models are not flexible enough to incorporate the characteristic periodic oscillations (Jones and Ma, 2001; Dubrule, 2017), called hole-effects. Facies cyclicity and rhythmicity could theoretically be modelled by Multi-Point Statistics (Strebelle, 2002), but it is challenging to include those patterns in the required three dimensional training image.

A geostatistical method has been developed recently to model simultaneously facies cyclicity and rhythmicity (Le Blévec et al., 2018), thus improving the realism of facies Earth models. The method is based on Pluri-Gaussian Simulations (Armstrong et al., 2011), constrained by facies transiograms. The facies asymmetric ordering (or cyclicity) is defined by two Gaussian random functions spatially shifted from each other, and rhythmicity of the facies succession is modelled by defining new hole-effect covariance models (Le Blévec et al., 2018).

So far, this method has only been used to model cyclicity in the vertical direction, although cyclicity can also be observed in lateral directions. Stratigraphic forward models can produce asymmetry between facies in lateral directions (Burgess et al., 2001), and such lateral facies asymmetry is also explicit within Walther's Law (e.g., Middleton, 1973). This could possibly be modelled with the shifted Pluri-Gaussian method (Le Blévec et al., 2018) by defining a spatial shift with a lateral component.

Modelling Diagenesis

Reservoir quality is not only affected by depositional facies cyclicity. Rock properties of carbonate (e.g., Bartok et al., 1981; Moore, 2001) and siliciclastic (e.g., Taylor et al., 2010) deposits are also influenced by diagenesis. Diagenetic processes give rise to depositional and diagenetic facies with a variety of geometrical relationships, which should be captured by the modelling method. Early diagenesis tends to closely follow the texture and stratal configuration of depositional facies (e.g., Ginsburg, 1957; Egenhoff et al., 1999; Peterhänsel and Egenhoff, 2008; Rameil, 2008) while late diagenesis either follow depositional features, or other structures such as faults, fractures, and karsts, thus resulting in diagenetic bodies and trends that cut across depositional facies geometries (e.g., Sharp et al., 2010; Vandeginste et al., 2013; Jacquemyn et al., 2014; Beckert et al., 2015). It is therefore highly desirable that reservoir modelling methods are flexible enough to embrace these different possibilities.

In many geostatistical studies, diagenesis is modelled as porosity or permeability variations (Wang et al., 1998; Pontiggia et al., 2010). This is a useful approach, but it cannot be applied to the representation of distinct diagenetic geobodies or of different diagenetic phases within a depositional facies. Therefore, some authors model diagenesis as a facies random field that is superimposed on the depositional facies field (Renard et al., 2008; Doligez et al., 2011; Barbier et al., 2012; Carrera et al., 2018). These authors use a version of truncated Pluri-Gaussian Simulations (Bi-PGS) developed by Renard et al. (2008), which models two facies fields with different Gaussian random functions. The depositional and diagenetic facies fields can be either independent of or correlated to each other, which allows to model depositional and diagenetic facies geometries that are either discordant or conformable. However, this method does not generate distributions of diagenetic facies that are asymmetric such as occurring preferentially towards the top or the base of depositional facies bodies.

The algorithm of Renard et al. (2008) to model diagenesis is thus extended here by including a shift between depositional and diagenetic facies fields, which allows diagenetic facies to overprint depositional facies preferentially at their top or at their base. These relationships are constrained by cross-transiograms between the two facies fields, and the method is also

combined with the advancements of Le Blévec et al. (2018), so that diagenesis is modelled in the context of depositional facies cyclicity and rhythmicity.

Aims

Therefore, this paper presents a new geostatistical facies modelling method that is able to represent facies cyclicity and rhythmicity, together with diagenetic facies bodies, which have either conformable or non-conformable geometries. The structure of the paper is outlined below. First, we illustrate the concepts of cyclicity and rhythmicity and show that these concepts are captured by transiograms. Modelling of cycles and rhythms is then illustrated using: (1) synthetic facies successions; (2) facies successions from the outcropping Triassic Latemar carbonate platform of Northern Italy; and (3) lateral facies relationships on the interior of the modern Bermuda carbonate platform. Then, diagenesis is modelled by adding another Gaussian random function to the method. Three examples are modelled to illustrate the flexibility of the method: (1) syn-depositional diagenesis below hardgrounds in facies cycles of the Latemar carbonate platform; (2) early diagenetic development of concretions in shallow-marine, siliciclastic facies cycles in the Cretaceous Blackhawk Formation, Book Cliffs outcrops (Utah), in which the facies proportions are non-stationary; and (3) post-depositional diagenesis caused by localised movement of hydrothermal fluids through faults and fractures in the Latemar carbonate platform.

6.3 Quantifying Cyclicity and Rhythmicity with Transiograms

6.3.1 Defining Cyclicity and Rhythmicity

Although facies cyclicity and rhythmicity are commonly interpreted in sedimentary sequences, these concepts have different meanings to different authors. Formal, quantitative definitions of

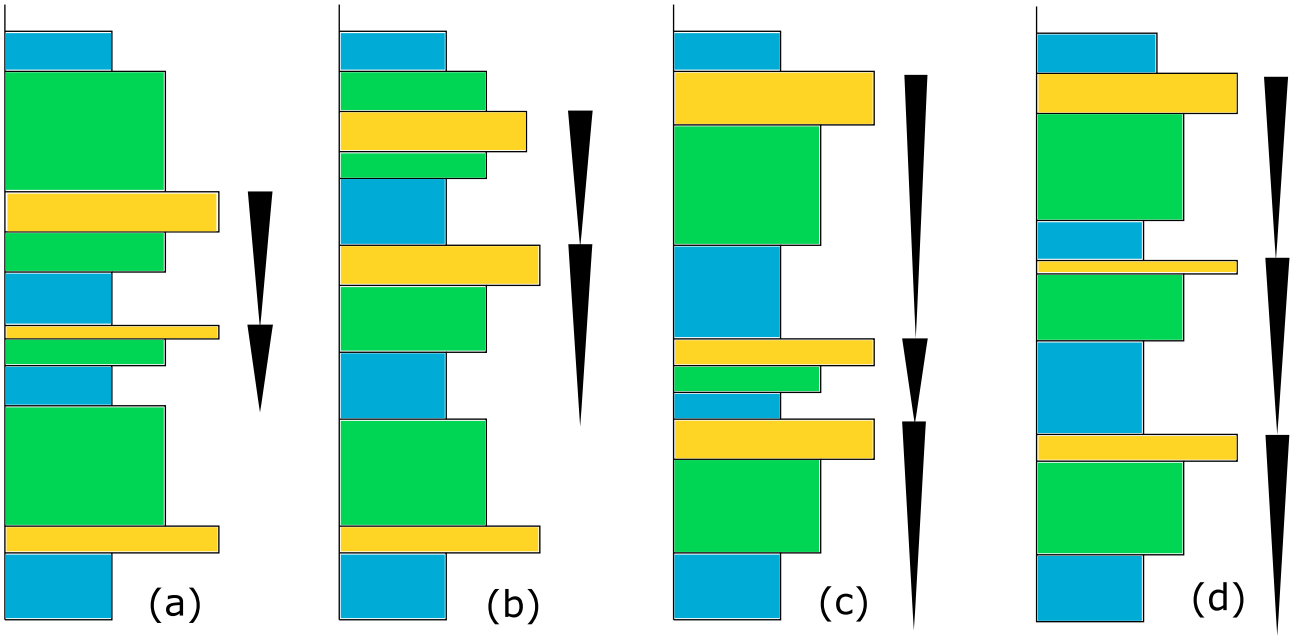

Figure 6.1: Four synthetic facies successions: (a) non rhythmic with two cycles; (b) rhythmic (blue facies) with two cycles; (c) cyclic and non rhythmic; and (d) cyclic and rhythmic. Modified from Le Blévec et al. (2018).

cyclicity and rhythmicity are needed for facies modelling, as a facies succession can be more or less ordered or exhibit more or less variability in facies thickness. Cyclicity is defined as facies ordering in a given direction (Gingerich, 1969; Hattori, 1976; Le Blévec et al., 2018), usually vertically (Fig. 6.1). The ordering considered here is asymmetric, which means that it differs going upwards from going downwards. For instance, in vertical shallow-marine carbonate and siliciclastic successions, facies cycles tend to be shallowing-upward (Strasser, 1988; Goldhammer et al., 1990; Lindsay et al., 2006), which is equivalent to deepening-downward.

Another commonly observed feature is that the same facies tends to appear repeatedly at intervals of constant thickness (e.g., Goldhammer et al., 1993; Lindsay et al., 2006), which defines rhythmicity (De Boer and Wonders, 1984; House, 1985; Le Blévec et al., 2018). If cyclicity and rhythmicity are both present, it implies that the facies cycles have low variability in thickness. For instance, the vertical succession in Figure 6.1d is cyclic and rhythmic because the facies are fully ordered and have constant thickness intervals between them. The succession illustrated in Figure 6.1a has non-ordered transitions between facies and also contains two facies cycles. The succession in Figure 6.1b also contains two facies cycles, and the blue facies is rhythmic, because intervals between occurrences of this facies have similar thickness. Figure 6.1c shows a cyclic

and non-rhythmic facies succession, and the succession in Figure 6.1d is cyclic and rhythmic, because the facies are fully ordered and the blue facies is separated by intervals of constant thickness. For three-dimensional Earth models to be geologically realistic, facies cyclicity and rhythmicity must be properly modelled.

6.3.2 The Transiogram: a Tool to Capture Cyclicity and Rhythmicity

Standard geostatistical simulation approaches quantify geologic patterns by computing experimental variograms, modelling them mathematically and then ensuring that the variogram models are reproduced in the final simulation (Pyrcz and Deutsch, 2014). However, Carle and Fogg (1996) show that variograms are not able to quantify asymmetric cycles, and promote the use of the transiogram instead.

The transiogram gives the probability $t_{AB}(h)$ of finding a facies B at a vector h from a given facies A (Carle and Fogg, 1996; Le Blévec et al., 2018). If the two facies A and B are identical, the transiogram is referred to as an auto-transiogram, otherwise it is referred to as a cross-transiogram. Auto-transiograms and cross-transiograms are calculated experimentally and gathered in a transiogram matrix (Fig. 6.2). As with variograms, the direction h is usually vertical, but it can also have a lateral component if calculated along other directions. For sedimentary facies, transiograms are commonly different in opposite directions (e.g., upward and downward) (Carle and Fogg, 1996).

Transiograms have specific properties, which are described in detail by Carle and Fogg (1996). One property is that at long distances h, $t_{AB}(h)$ tends towards the proportion of facies B. For example, Figure 6.2b-e shows that the transiograms tend towards the value of 0.5, which is the proportion of facies 1, and 0.25, which is the proportion of facies 2. Also, the tangent at the origin $t'_{AA}(0)$ of the auto-transiogram $t_{AA}(h)$ defines the mean length of facies A, denoted as $\overline{L_A}$ (Carle and Fogg, 1996), as shown in Figure 6.2b, e ($\overline{L_1}$ and $\overline{L_2}$).

Figure 6.2c, and 2d also show that cyclicity is captured by the behavior at the origin of the

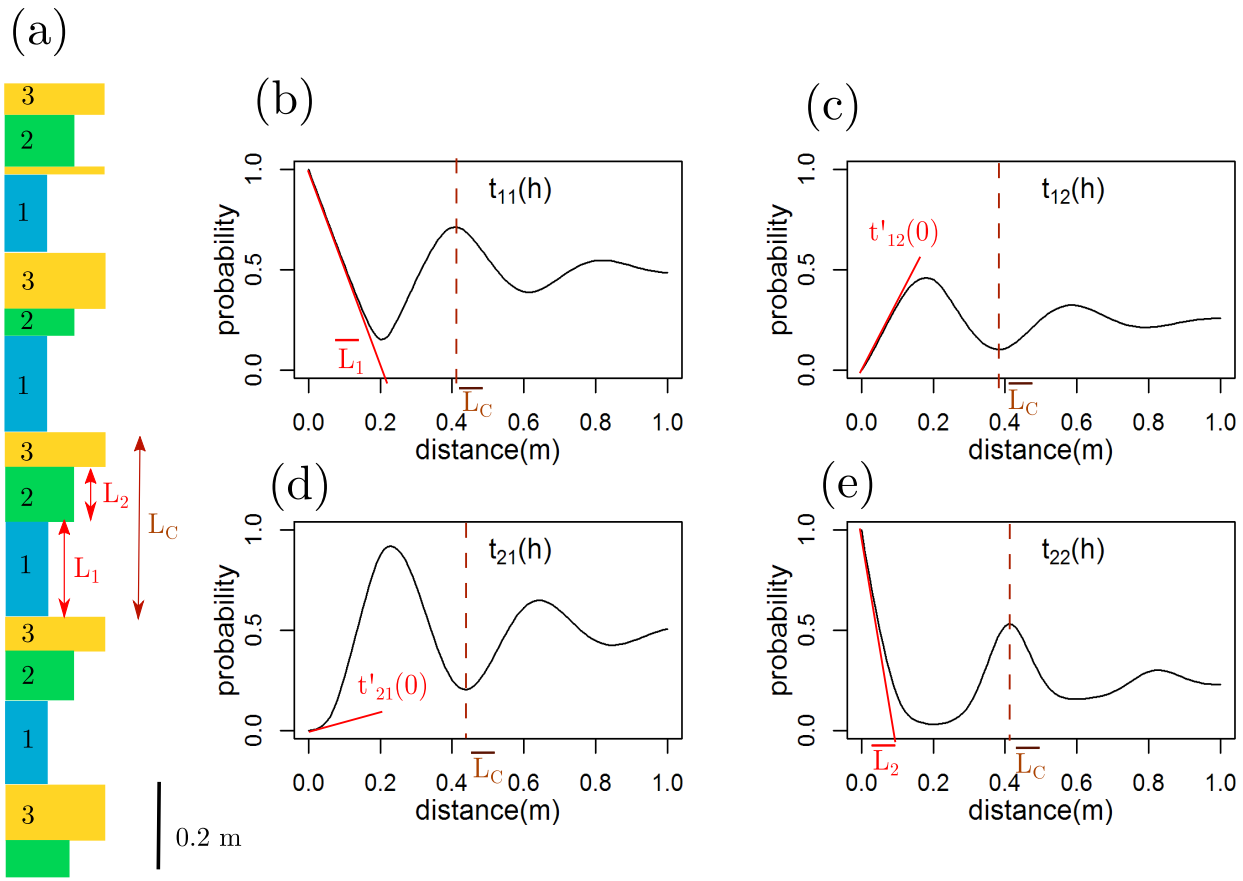

Figure 6.2: Cyclic and rhythmic facies succession (a) with associated transiogram matrix between facies 1 and 2 (b-e). $\overline{L_c}$ is the mean thickness of a facies cycle, and $\overline{L_1}$ and $\overline{L_2}$ are the mean thicknesses of facies 1 and 2. Proportion of facies 1 is 0.5 and proportion of facies 2 is 0.25.

cross-transiograms (Le Blévec et al., 2018). $t'_{12}(0)$ is high while $t'_{21}(0)$ is low, which means that facies 2 tends to overlie facies 1, while facies 1 does not tend to overlie facies 2. Consequently facies 3 overlies facies 2, creating facies cycles with facies 1 at the base, facies 2 in the center and facies 3 at the top. This cyclicity is observed in the corresponding succession (Fig. 6.2a), which shows that facies 1 almost always transitions upward to facies 2 (except on one occasion when it transitions directly to facies 3), and facies 2 transitions upward to facies 3.

Rhythmicity is characterized by the oscillations of the transiograms or variograms (Jones and Ma, 2001; Le Blévec et al., 2018), as shown in Figure 6.2. The average distance separating two repetitions of a facies is given by the first maximum of the corresponding auto-transiogram, as this is associated with the highest probability of finding the same facies (Fig. 6.2b, e, $\overline{L_c} = 0.4$ m). It also corresponds to the first minimum of the cross-transiograms (Fig. 6.2c, d), which is associated with the lowest probability of finding two different facies. In this case, because there is also cyclicity, this length $\overline{L_c}$ corresponds to the average thickness of the facies cycle and is approximately the sum of the mean thicknesses of all facies present in a cycle. This also explains why the auto-transiogram of facies 2 shows the same rhythmicity (Fig. 6.2e) as the auto-transiogram of facies 1 (Fig. 6.2b). Rhythmicity can be visually verified by examining the corresponding succession (Fig. 6.2a), which shows that facies cycles indeed exhibit low thickness variations (thickness of approximately 0.4 m). Therefore, transiograms appear to be better suited than variograms to the quantification of cyclicity and rhythmicity.

6.4 Modelling Cyclicity and Rhythmicity with Shifted Pluri-Gaussian Simulations

6.4.1 Principle of Truncated Gaussian Simulations

The truncated Gaussian approach for facies modelling was first developed by Matheron et al. (1988) and is explained in detail by Armstrong et al. (2011). It has two steps: (1) first, the simulation of a continuous Gaussian random function, and then (2) the truncation of this

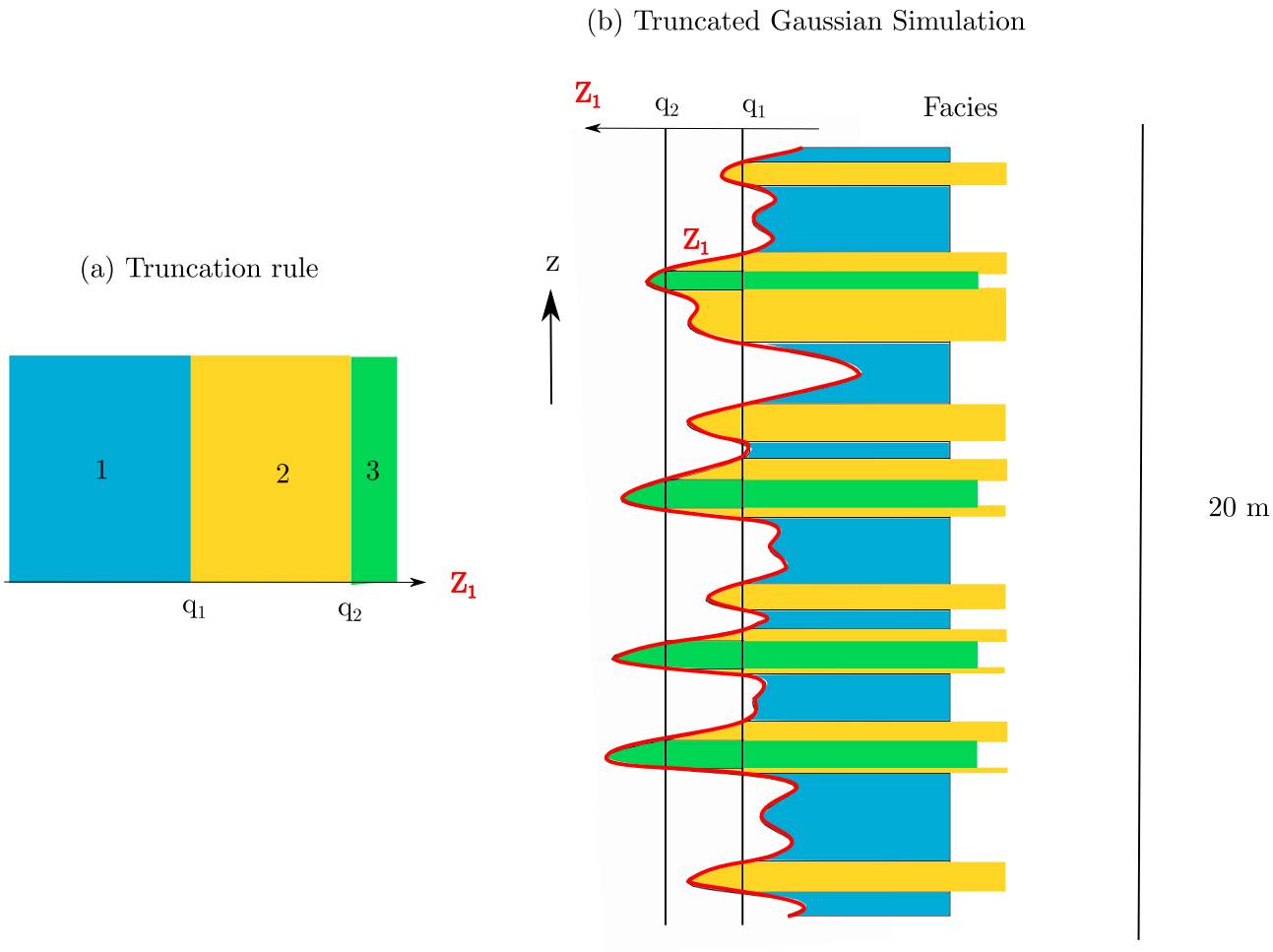

Figure 6.3: Facies succession (b) modelled with Truncated Gaussian Simulations according to the truncation rule (a) and parameters $r_1 = 0.1$ m , $b_1 = 0$ m^{-1}, $(p_1, p_2, p_3) = (0.4, 0.4, 0.2)$ (Eq. 6.A.4a).

continuous function into facies with the help of a truncation rule.

A Gaussian random function defines at every location (x, y, z) (usually in a grid) a Gaussian random variable. The Gaussian random function is controlled by its covariance model (Chiles and Delfiner, 2012). In this paper, as explained in the Appendix, Gaussian cosine covariances (with frequency parameter b) are used with scale factor noted r_z (Eq. 6.A.4a) in the vertical direction. In lateral directions Gaussian covariances are used, with scale factors noted r_x and r_y for each principal direction (Eq. 6.A.4a). Scale factors control the average length scale of the Gaussian random functions in the corresponding direction and b their periodicity (Le Blévec et al., 2018). Figure 6.3b (red curve) shows an example of a realization of a Gaussian random function Z_1 along a vertical succession (i.e., on a one-dimensional grid).

The truncation rule defines the number of facies, their proportions, and their contacts. For instance, Figure 6.3a shows a truncation rule with three facies, with a small area for facies 3 defined by the threshold q_2. This results in a smaller proportion of facies 3 in the corresponding vertical succession (Fig. 6.3b). As shown by Figure 6.3b, when Z_1 is higher than q_1, facies 2 is allocated, and when it reaches q_2, facies 3 is defined.

By using only one Gaussian random function, modelling is limited because each facies can only transition into one or, at most two other facies. For instance, in Figure 6.3 facies 1 and 3 can only transition into facies 2, while facies 2 can transition into both facies 1 and 2 upward or downward. Therefore, cyclicity cannot be modelled because there is no asymmetry associated to the simulation. Armstrong et al. (2011) extend the method to Pluri-Gaussian Simulations, and it was then modified by Le Blévec et al. (2018) to model cyclicity.

6.4.2 The Shifted Pluri-Gaussian Simulations Approach

Here we summarize the modelling method developed in Le Blévec et al. (2018). The method is based on Pluri-Gaussian Simulations (PGS) (Armstrong et al., 2011), which generalizes Truncated Gaussian Simulations by using several Gaussian random functions instead of just one. An example is given in Figure 6.4b, which shows a Pluri-Gaussian Simulation using two Gaussian random functions Z_1 and Z_2. The variations of each Gaussian random function are controlled by their respective covariance model (Eqs. 6.A.4a and 6.A.4b). The truncation rule applied to them is two dimensional (Fig. 6.4a) and defines in this example three facies separated by two thresholds q_1 and q_2, with all three facies in contact with each other. For instance, the defined facies is yellow if q_1 is smaller than Z_1 and q_2 is smaller than Z_2. The corresponding facies succession (Fig. 6.4b) shows no specific cyclicity, because all facies can transition into each other randomly.

In order to model cyclicity, Le Blévec et al. (2018) introduced a spatial shift α between the two Gaussian random functions. More specifically, the Gaussian random functions are correlated (or anti-correlated) to each other by a correlation coefficient β, then shifted by a vector noted α (Eq. 6.A.3), which gives the direction of the cyclicity. This is illustrated in Figure 6.4c, in

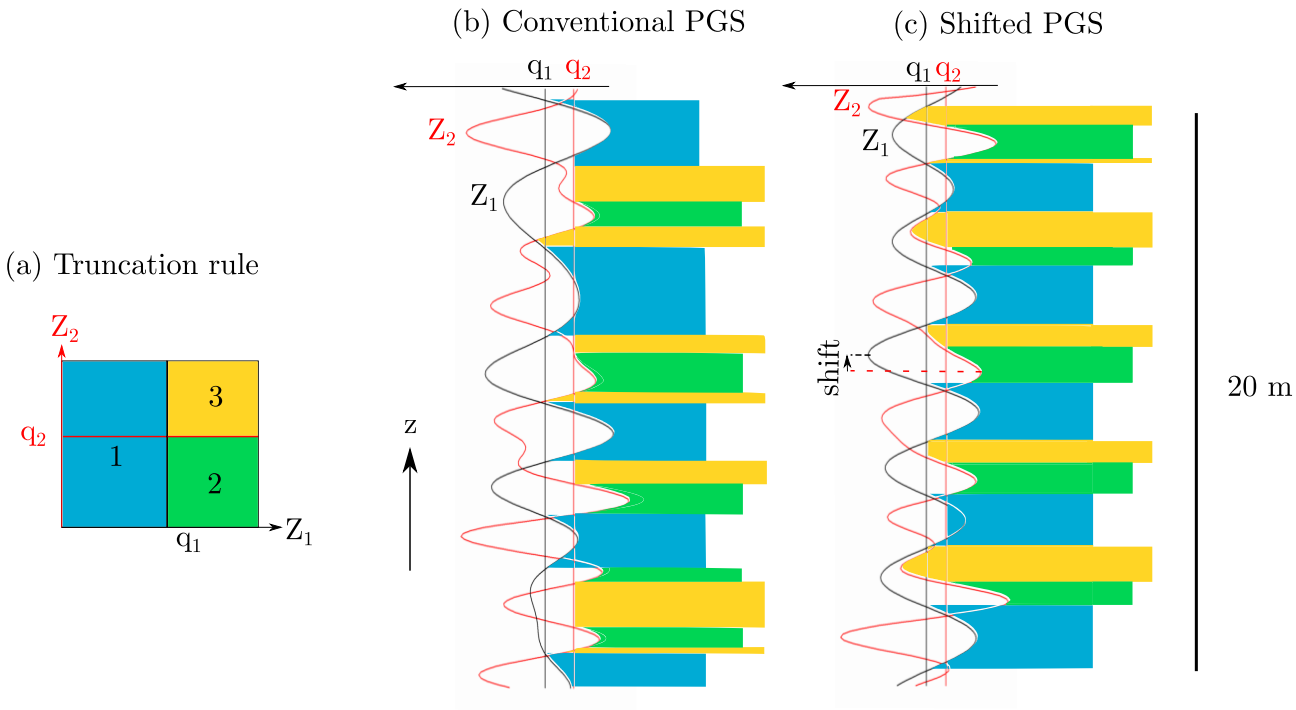

Figure 6.4: Comparison between conventional Pluri-Gaussian Simulation (PGS) (b) and shifted PGS (c) with the same truncation rule (a). For (b), the parameters are $r_1 = r_2 = 0.6$ m, $b_1 = 15$ m^{-1}, $b_2 = 30\ \mathrm{m}^{-1}$ (Eqs. 6.A.4a, 6.A.4b), and facies proportions $(p_1, p_2, p_3) = (0.5, 0.25, 0.25)$ and for (c), the same parameters are applied together with the shift $\alpha_{12} = 0.04$ m and correlation coefficient $\beta_{12} = -0.7$ (Eq. 6.A.3).

which the Gaussian random functions are anti-correlated ($\beta < 0$), with a small shift α oriented upward. This results, after truncation, into a highly cyclic facies succession (Fig. 6.4c). The upward cycle from facies 1 to facies 2 then to facies 3 is repeated almost everywhere because Z_2 tends to cross its threshold q_2 (from facies 2 to facies 3) just after Z_1 crosses its threshold q_1 (from facies 1 to facies 2), as if the truncation rule (Fig. 6.4a) had an anti-clockwise motion in the upward direction. The cyclicity of the succession shown in Figure 6.4c is confirmed by its corresponding transiograms (Fig. 6.2) as explained previously.

6.4.3 Modelling Vertical Facies Cyclicity and Rhythmicity in the Latemar Carbonate Platform

Dataset

The Triassic Latemar carbonate platform (northern Italy) is renowned for its cyclicity (Goldhammer et al., 1990; Hinnov and Goldhammer, 1991) and is thus well suited for analysis to the new method described above. Using the original data of Peterhänsel and Egenhoff (2008), part of the Upper Cyclic Facies interval has previously been modelled by Le Blévec et al. (2018) with a simplified, three-fold classification of depositional facies that is modified from Egenhoff et al. (1999). Here, the same interval is modelled in the Cimon Latemar outcrop with the full four-fold classification of depositional facies of Egenhoff et al. (1999): subtidal (e_1), intertidal (e_2), supratidal (e_3) and subaerial exposure facies (e_4). Diagenetic overprinting is at first not considered in the model described here, but models of the Latemar platform presented later include diagenetic facies. Although depositional facies are here denominated as environments of deposition, their interpretation is directly based on application of the Dunham classification to observations in thin sections (Egenhoff et al., 1999). Therefore, it is possible that they transition laterally with each other several times at the same stratigraphic level, in a mosaic-like fashion, as shown by the interpreted cross section of Peterhänsel and Egenhoff (2008). The measured sections of Peterhänsel and Egenhoff (2008) are presented in Figure 6.5.

As discussed by Egenhoff et al. (1999) and Peterhänsel and Egenhoff (2008), the facies tend to be organized in shallowing-upward facies cycles that comprise, from base to top, facies 1, facies 2, facies 3, facies 4. This interpreted organization is supported by logs in Figure 6.5. For example, the subtidal facies e_1 tends to overlie the subaerial exposure facies e_4, which defines the base of a cycle, and is generally overlain by intertidal facies e_2. However, many cycles are incomplete and lack one or more facies (Fig. 6.5). There is also a high number of alternations between intertidal facies e_2 and subaerial exposure facies e_4 (e.g., in log $N17$, Fig. 6.5). Therefore, the cyclicity of the facies succession is not perfect and this imperfect pattern should be reproduced statistically in the model. It is also noteworthy that subtidal facies e_1 and supratidal facies e_3

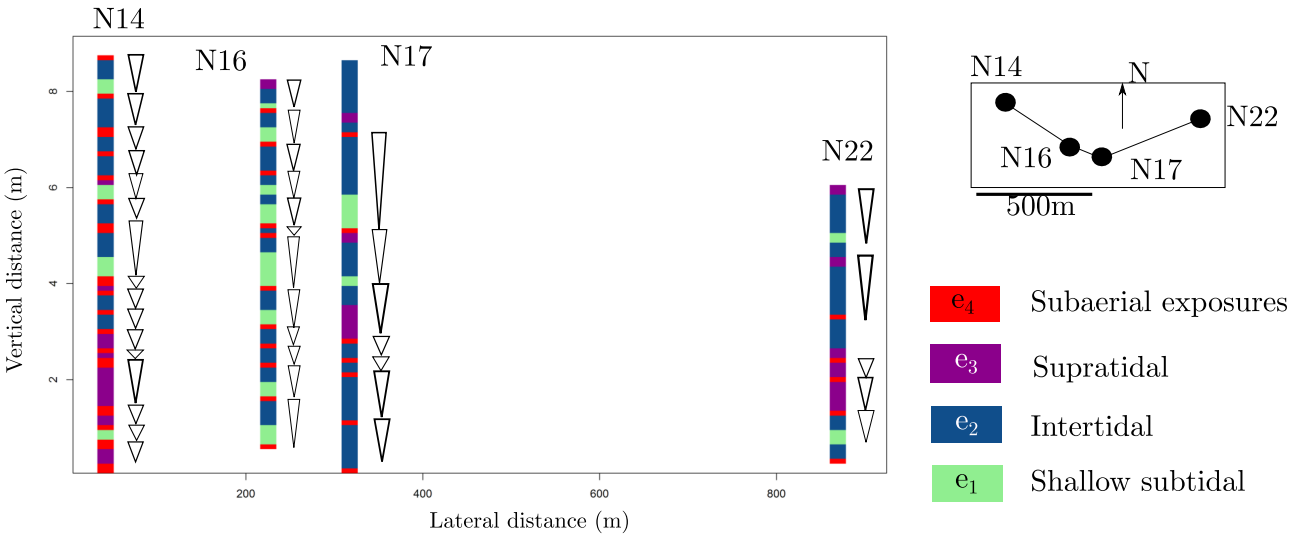

Figure 6.5: Measured sections through part of the Upper Cyclic Facies interval in the Cimon Latemar outcrop, Latemar platform. Figure modified from Peterhänsel and Egenhoff (2008).

are never in contact (Fig. 6.5).

Model

The first step is to define an appropriate truncation rule based on the observed contacts between facies and their cyclicity. As the typical cycle is $e_1 \rightarrow e_2 \rightarrow e_3 \rightarrow e_4$, these facies should be arranged clockwise (or counter-clockwise) in the truncation rule. Moreover, as observed (Fig. 6.5), subtidal facies should not be in contact with supratidal facies. Figure 6.6 shows a truncation rule satisfying these constraints. The thresholds q_1, q_2 and q_3 are computed according to the proportions of the different facies (an example of how to compute the thresholds from the proportions is given in the Appendix, using Eqs. 6.A.7, 6.A.8 and 6.A.9).

The next step is to find the parameters of the model (β_{12}, α_{12}, r_1, r_2, b_1, b_2) from the experimental transiograms computed from the logs. The results are shown in Figure 6.7 (grey points). The parameters of the method are found so that they generate theoretical transiograms that provide a good match to the experimental transiograms. The computation of a theoretical transiogram from the parameters of the method is explained in the Appendix (Eqs. 6.A.10, 6.A.11 and 6.A.12). A trial-and-error test is performed on the parameters, and the ones which give the best fit between experimental and theoretical transiograms are chosen.

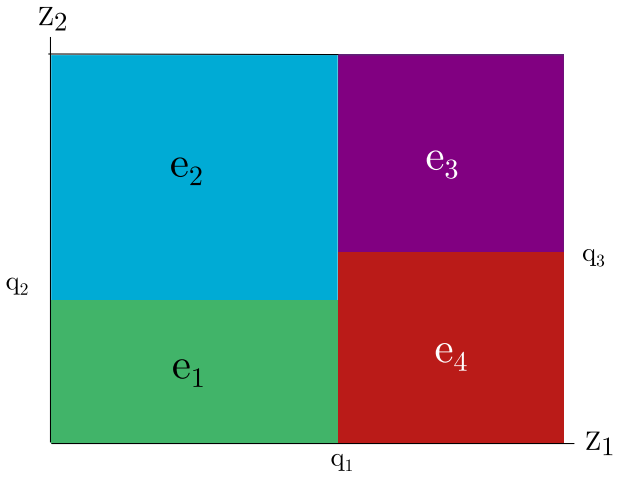

Figure 6.6: Truncation rule used for modelling depositional facies in the Latemar platform dataset (Fig. 6.5).

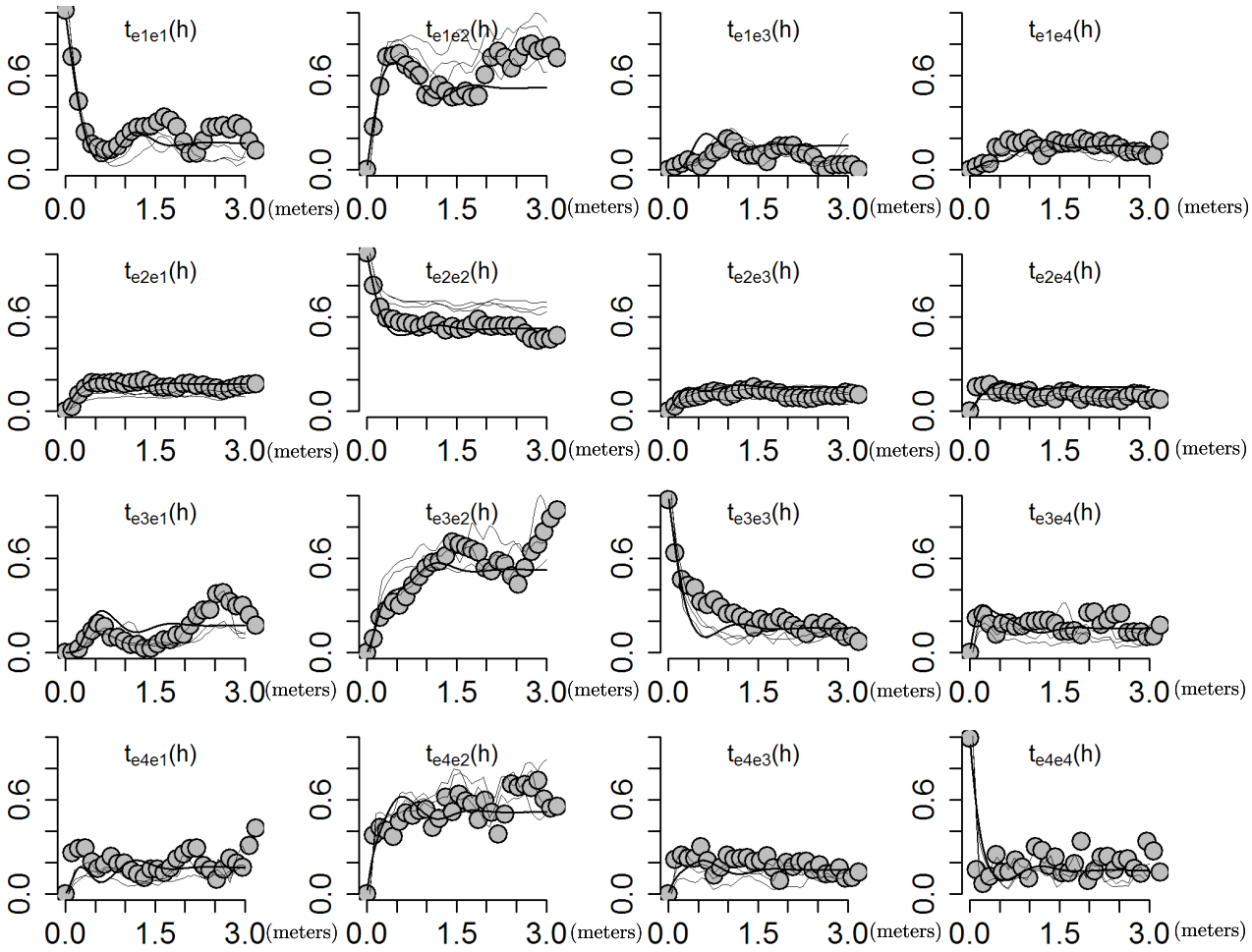

Figure 6.7: Experimental transiograms (grey points) in the upward vertical direction of depositional facies computed from the measured sections shown in Figure 6.5, theoretical transiograms fitted to these points (black line), and transiograms computed in three realizations of the depositional facies Earth model (thin grey lines). The parameters used for the theoretical transiograms are $r_1 = (800, 800, 0.3)$ m, $r_2 = (800, 800, 1.2)$ m, $b_1 = 0$ m^{-1}, $b_2 = 5$ m^{-1}, $\beta_{12} = 0.67$, $\alpha_{12} = 0.1$ m (Eqs. 6.A.4a, 6.A.4b).

It is important to note that transiograms are inter-dependent and cannot be fitted individually. For instance, the first maximum of the auto-transiograms and first minimum of the cross-transiograms are related to the cycle thickness, as explained earlier (Fig. 6.2). Thus, one parameter such as the shift α_{12} controls the behavior of several theoretical transiograms (see Le Blévec et al., 2017b, for details). Because of these relationships between transiograms, it is usually not possible to obtain a perfect fit between experimental and theoretical transiograms, and a compromise should be made based on which feature (or combination of features) is considered by the user to be more important.

The theoretical transiograms after fitting are shown in Figure 6.7 (black curves). The tangents at the origin of the different auto-transiograms and cross-transiograms are matched, which means that the different facies thicknesses and the contacts between them are well constrained. Therefore, the fit between experimental and theoretical transiograms is satisfactory. Subtidal facies e_1 and supratidal facies e_3 are not in contact because $t_{e_1e_3}(h)$ and $t_{e_3e_1}(h)$ both have a tangent at the origin with a very low value, which comes from the truncation rule (Fig. 6.6). The only significant mismatch is for the transiogram $t_{e_4e_1}(h)$, for which the tangent at the origin of the theoretical transiogram is not high enough (Fig. 6.7). This means that in the model, facies e_1 has less tendency to overlie facies e_4 than in the dataset.

Some rhythmic facies patterns are also captured, such as the one observed in the transiogram $t_{e_1e_1}(h)$ (Fig. 6.7).

The scale factors in the lateral direction r_x and r_y are chosen by visual comparison of the resulting facies models with the outcrop cross section of Peterhänsel and Egenhoff (2008). The higher their values, the larger the extent of the facies. As the facies are quite laterally extensive, the scale factors are of the order of the size of the final Earth model of depositional facies.

Simulation

The Earth model for depositional facies is now built using the above fitted parameters. The Gaussian random functions are simulated in the grid described below, and then truncated into

facies. The simulations are also conditioned to the measured sections so that the facies observed in the measured sections are reproduced in the model realizations. The algorithms to perform these steps are explained in Le Blévec et al. (2018).

The number of grid cells in each direction (East, North, Z) is $(100, 10, 182)$, and the grid dimensions are (1000 m, 250 m, 9.1 m)∼(0.62 mi, 820 ft, 29 ft). Hence the size of each cell is (10 m, 25 m, 5 cm)∼(33 ft, 82 ft, 16 ft). The number of cells is a compromise between the desired computational speed of the simulation and the level of details at which the heterogeneities are represented. Here, a high resolution is chosen in the vertical direction, because most of the transitions between facies are vertical. The simulation is fast and several equiprobable realizations are obtained in a two or three minutes with a standard desktop PC. Two realizations are shown in Figure 6.8, together with the original measured sections of Peterhänsel and Egenhoff (2008), reproduced in both realizations.

Incomplete facies cyclicity, as observed in the measured sections (Fig. 6.5) is visible in the realizations (Fig. 6.8). For instance, subaerial exposure facies e_4 are not only overlain by subtidal facies e_1 at the base of each cycle, but also by intertidal facies e_2 or supratidal facies e_3. Subtidal facies e_1 and supratidal facies e_3 are not in contact, as defined by the truncation rule (Fig. 6.6). Laterally, facies transition randomly into each other because no lateral transition constraint is given. This aspect of the Earth model realizations can be improved by using conceptual knowledge of the platform-interior facies architecture, leading to Earth models that exhibit lateral facies cyclicity or non-stationarity, as illustrated below.

For model validation, the transiograms are computed in three realizations of the simulation and shown in Figure 6.7 (thin grey curves). Most transiograms of the realizations are a good fit to the experimental and theoretical transiograms, which shows that the Earth models are geologically realistic. Some mismatches also appear, for instance in $t_{e_2e_2}(h)$, for which it seems that the realizations have a higher plateau than the model. However, these statistical variations are not systematic and are common with stochastic simulations (Chiles and Delfiner, 2012).

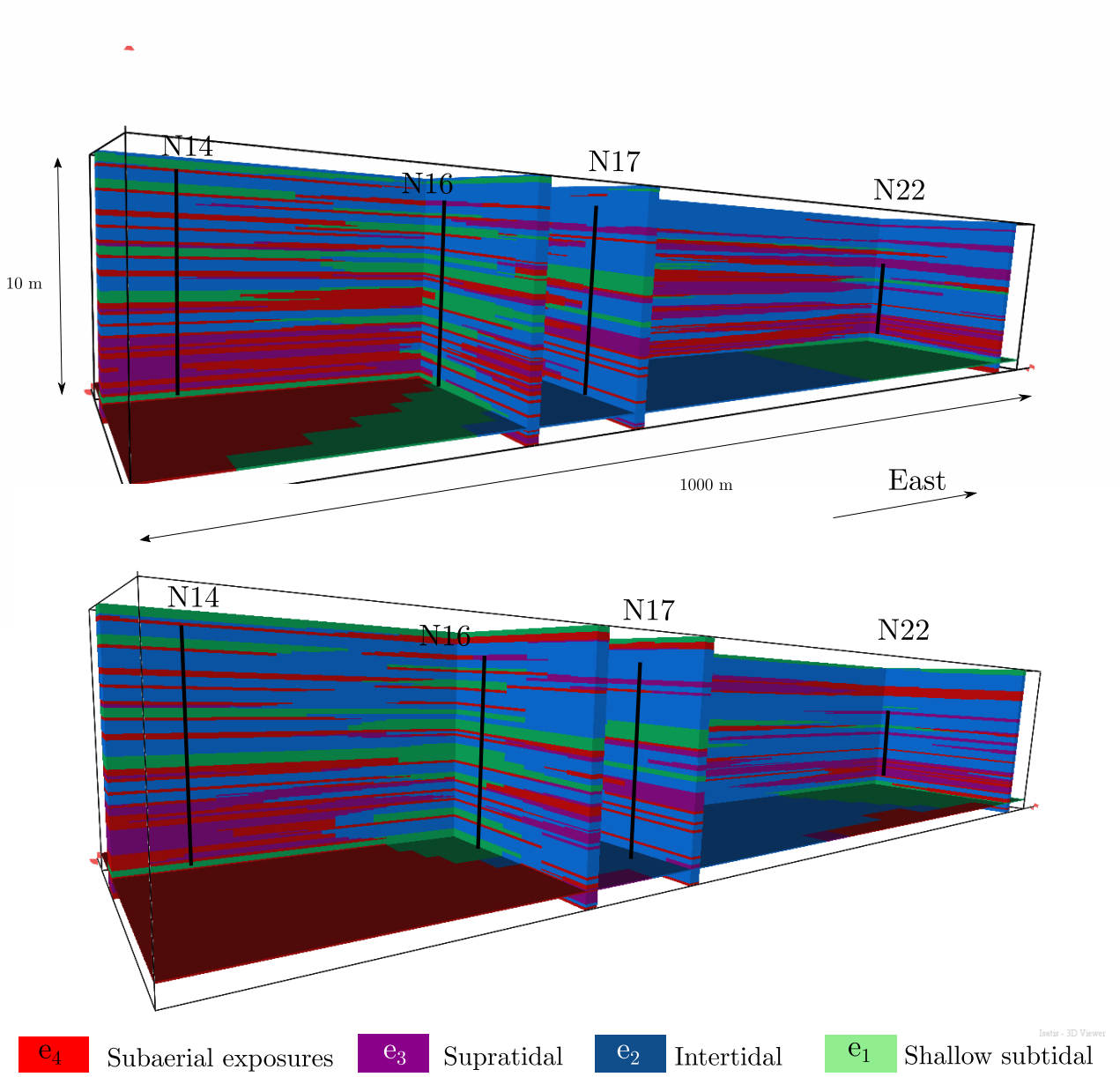

Figure 6.8: Two realizations of an Earth model for depositional facies in the Cimon region of the Latemar carbonate platform conditioned by four measured sections (Fig. 6.5) with modelling parameters explained in Figures 6.7.

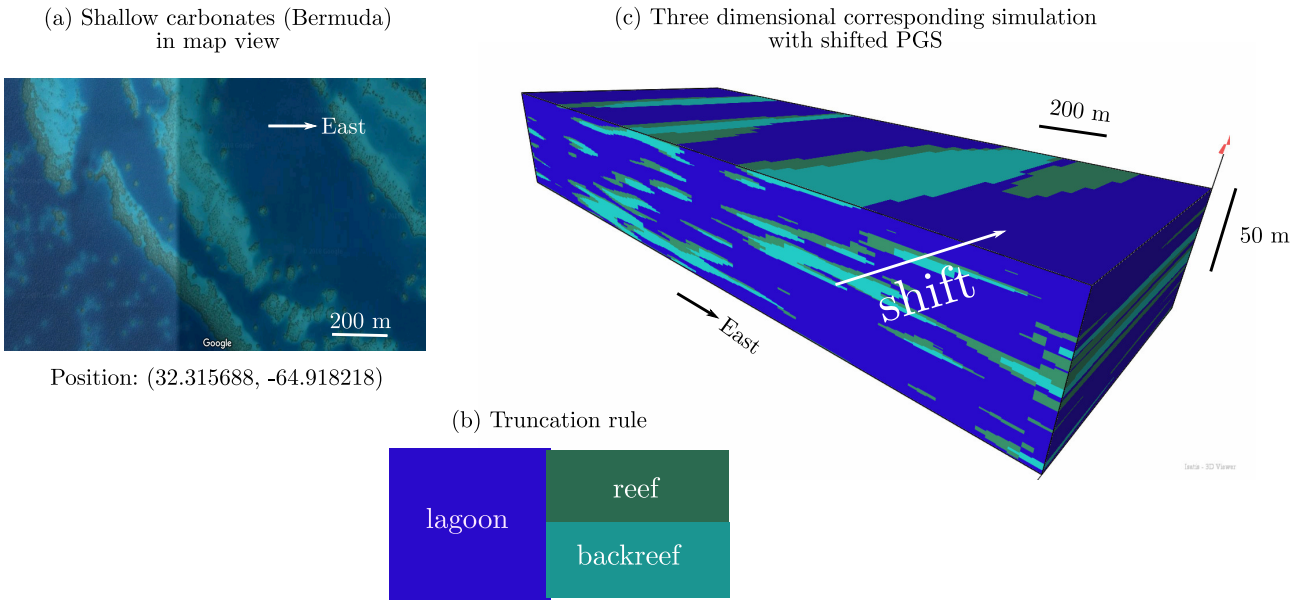

Figure 6.9: Three dimensional unconditional realization from a satellite image of Bermuda carbonate platform interior. (a) satellite image (with latitudinal and longitudinal position) showing three types of facies based on visual interpretation: blue represents the lagoon, light green the backreef, and dark green the reef; (b) truncation rule; and (c) 3D Earth model of facies distributions. The parameters of the simulation are $r_1 = r_2 = (20, 100, 0.4)$ m, $\alpha_{12} = (0.1, 5)$ m, $(p_1, p_2, p_3) = (0.15, 0.15, 0.7)$ (Eqs. 6.A.4a, 6.A.4b).

6.4.4 Extension to Lateral Cyclicity

Lateral facies cyclicity can be observed in modern environments or generated by forward stratigraphic modelling (Burgess et al., 2001). Tidal-flat and reef islands deposits in modern shallow-water carbonate environments can exhibit lateral directionality, induced by currents in the water column, which results in lateral and vertical facies cyclicity (e.g., Burgess et al., 2001). The method developed here models such vertical and lateral facies cyclicity by adding a lateral component to the shift α between the Gaussian random functions. This procedure is demonstrated using a satellite image of reef islands in the interior of the modern Bermuda platform, which was first described by Verrill (1907) (Fig. 6.9a). The reef island deposits show a lateral facies asymmetry, with a typical facies cycle comprising reef, backreef, and lagoonal facies (after Jordan Jr, 1973). Although there are no data describing the vertical facies succession, we assume that Walther's law (Middleton, 1973) is followed, such that the lateral facies transitions are equivalent to the vertical facies transitions. This equivalence is modeled by incorporating the lateral component into the shift vector.

One unconditional (no vertical sections are matched) realization of an Earth model for facies distribution is shown in Figure 6.9c, along with the model truncation rule (Fig. 6.9b). The three modelled facies are in contact, and lateral facies cyclicity similar to that observed in the satellite image is generated. The vertical cyclicity is such that reef facies overlie backreef facies (Fig. 6.9c). The combination of lateral and vertical facies cyclicity results in an overall eastward progradation of reef islands. Therefore, the shift controls the movement over time of the facies belts and bodies. For instance, if the shift was oriented to the west, then this would be the direction of progradation. If the shift was purely vertical, there would only be aggradation. Due to the lateral component of the shift, Walther's Law is respected in the model.

6.5 Modelling Diagenesis with Shifted Pluri-Gaussian Simulations

Siliciclastic and, particularly, carbonate reservoirs are widely documented to undergo extensive diagenetic modification during deposition and subsequent burial, which modifies their petrophysical properties (Moore, 2001). Therefore, it is important to provide a flexible modelling method for diagenetic overprinting of depositional facies that can mimic patterns resulting from multiple diagenetic events, in order to capture the impact on hydrocarbon recovery. Diagenesis can follow the original depositional fabric in some cases, but can also be templated by faults and fractures and thus cross-cut depositional facies. A novel method able to model these two end members, based on the Shifted Pluri-Gaussian Simulations is presented. By adding a third Gaussian function that controls diagenetic facies, the method co-simulates a depositional facies field and a diagenetic facies field. The shifts between the three Gaussian random functions allows the user to model asymmetric relations between diagenetic and depositional facies.

Table 6.1: Proportions of diagenetic facies overprinted on depositional facies in the Latemar carbonate platform, taken from measured sections (Fig. 6.10).

	Dolomitic crust	**Partial dolomite**
Subtidal	0	0
Intertidal	0	0.10
Supratidal	0	0.02
Exposure	0.32	0

6.5.1 Modelling Syn-Depositional Diagenesis: Revisiting the Latemar Carbonate Platform

Syn-Depositional Diagenesis in the Latemar Platform

Previously we modelled the depositional facies of the Latemar carbonate platform using the measured sections of Peterhänsel and Egenhoff (2008) as input data. However, the studies of Egenhoff et al. (1999) and Peterhänsel and Egenhoff (2008) also show that diagenesis affect these facies. Tepee structures, dolomitization and caliche crusts suggest an early diagenetic overprinting.

The measured sections of Peterhänsel and Egenhoff (2008) are again chosen as data for the model. These sections show two diagenetic facies: completely dolomitized crusts and partial dolomitization, which overprint different depositional facies (Fig. 6.10). The dolomitic crust diagenetic facies only occurs in conjunction with subaerial exposure depositional facies, while the partially dolomitized diagenetic facies occurs in conjunction with intertidal and (marginally) supratidal depositional facies. This observation from vertical measured sections is supported by the interpreted lateral correlations of Peterhänsel and Egenhoff (2008), in which the dolomitic crust diagenetic facies transitions laterally only into subaerial exposure depositional facies. Table 6.1 shows the proportions of each diagenetic facies within each depositional facies.

Model

In the Earth model realizations shown in Figure 6.8, depositional facies were modelled using two Gaussian random functions. If diagenetic facies were included in the corresponding two di-

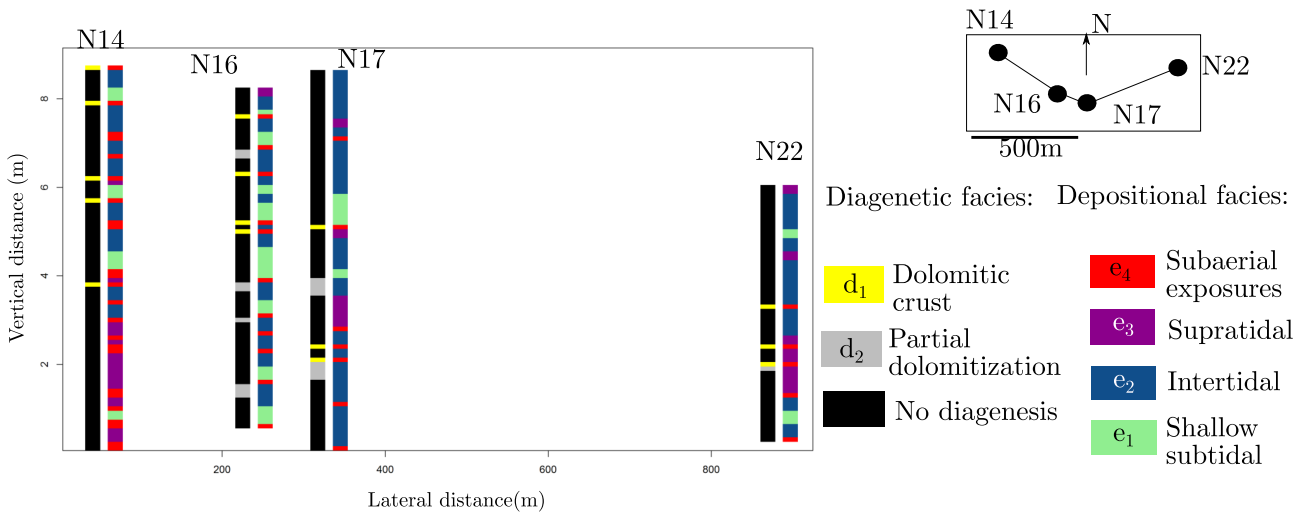

Figure 6.10: Depositional facies and diagenetic facies in the measured sections through part of the Upper Cyclic Facies in Cimon Latemar outcrop, Latemar carbonate platform (Fig. 6.5). Measured sections are adapted from Peterhänsel and Egenhoff (2008).

mensional truncation rule (Fig. 6.6), they would necessarily have geometrical properties similar to those of depositional facies. Adding a third Gaussian random function as a third dimension in the truncation rule gives a greater flexibility to represent diagenetic facies geometries and their relations with depositional facies. Moreover, diagenesis can then be modelled as a superimposed facies field that overprints the depositional facies as explained in Renard et al. (2008).

A three dimensional truncation rule for the Latemar platform is thus defined in Figure 6.11. The truncation rule for the depositional facies is the same as that shown in Figure 6.6. The third Gaussian random function defines two diagenetic facies: dolomitic crust d_1 (which overprints subaerial exposure depositional facies e_4) and partial dolomite d_2 (which overprints intertidal and supratidal depositional facies e_2 and e_3). Depositional facies e_1 is not affected by diagenesis. The thresholds q controlling the proportions of diagenetic facies within depositional facies are computed from Table 6.1, as explained in the Appendix (Eq. 6.A.7). For example, diagenetic facies d_2 is more abundant in depositional facies e_2 than in depositional facies e_3, and so its area is larger in the truncation rule (Fig. 6.11).

Once the truncation rule is chosen, the experimental transiograms of diagenetic facies are fitted with the parameters of the method, as described previously. Cross-transiograms between

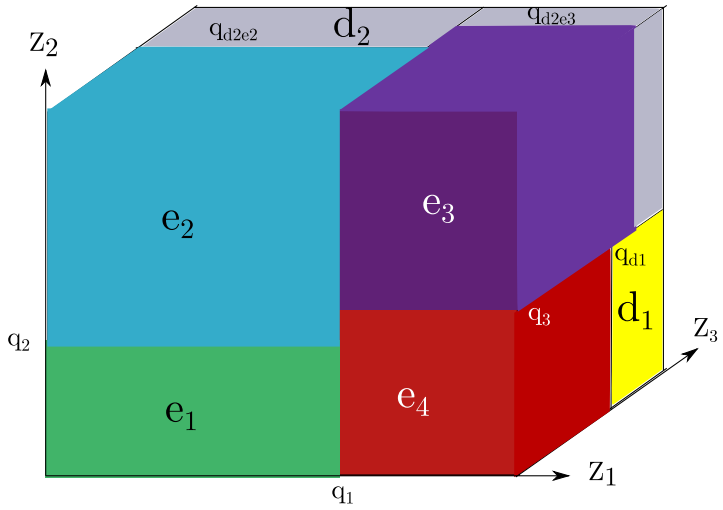

Figure 6.11: Three dimensional truncation rule used for modelling the depositional facies and diagenetic facies in the Latemar platform dataset (Fig. 6.10, Table 6.1).

depositional and diagenetic facies are fitted first, because they are controlled by a smaller number of parameters: α_{13}, β_{13}, α_{23} and β_{23} (Eq. 6.A.3). These parameters define the relations of the first two Gaussian random functions Z_1 and Z_2 with the third Gaussian random function Z_3 and thus control relations between depositional facies and diagenetic facies. These cross-transiograms have different properties from usual cross-transiograms because they relate to two superimposed facies fields, for which facies can both be present at the same location. Therefore, their value at a distance $h = 0$ is not 0 but the probability of finding the two facies types at the same location (Table 6.1). The fit between theoretical transiograms (black curves, Eq. 6.A.11) and experimental transiograms (grey points) of depositional facies and diagenetic facies is shown in Figure 6.12.

For most transiograms, the experimental curve at the first distance step is commonly higher than the theoretical curve (Fig. 6.12). This is due to the small number of data points, because there are few occurrences of diagenetic facies in the measured sections (Fig. 6.10), thus causing the transiograms to be statistically unreliable. However, it is worth noting that the theoretical transiograms generally show reasonable behaviors at the origin. For instance, the tangent at the origin of transiogram $t_{d_1 e_1}(h)$ has a high value (Fig. 6.12), which shows that subtidal depositional facies tends to overlie dolomitic crust diagenetic facies, as observed in the measured sections (Fig. 6.10). This spatial relationship supports the facies cyclicity of the model, because the

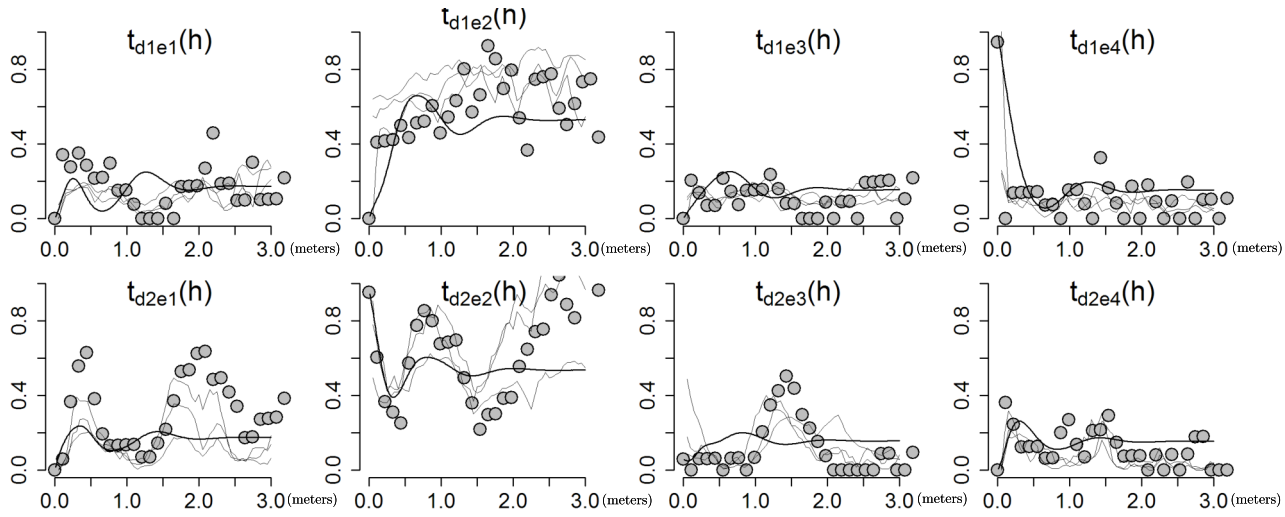

Figure 6.12: Experimental vertical cross-transiograms between depositional facies and diagenetic facies (grey points) from measured sections shown in Figure 6.10, theoretical cross-transiograms fitted to these points (black lines), and cross-transiograms computed in three realizations of a resulting Earth model (thin grey lines). The parameters defining the theoretical transiograms are the same as those for Figure 6.7, with in addition $\beta_{13} = -0.8$, $\beta_{23} = -0.5$, $\alpha_{13} = -0.1$ m, $\alpha_{23} = 0.1$ m (Eq. 6.A.3).

dolomitic crust diagenetic facies is present in the subaerial exposure depositional facies, which are themselves overlain by subtidal depositional facies. Similarly the high value of the tangent at the origin of transiogram $t_{d_2e_4}(h)$ shows that subaerial exposure depositional facies tends to occur above partial dolomite diagenetic facies, which is also observed in the measured sections (Fig. 6.10). The transiograms thus confirm that the method is able to capture asymmetry between depositional and diagenetic facies, so that diagenetic facies are ordered with respect to the depositional facies.

As stated above, the cross-transiograms between depositional facies and diagenetic facies are not equal to zero for a zero distance. For instance transiogram $t_{d_1e_4}(h)$ starts at a value close to 1 (Fig. 6.12) because the dolomitic crust diagenetic facies d_1 is only present in the subaerial exposure diagenetic facies e_4. The cross-transiogram then decreases abruptly, which suggests that units of the subaerial exposure diagenetic facies are thin, which is consistent with the measured sections (Fig. 6.10). Finally, rhythmicity, although not very pronounced, is captured in transiograms $t_{d_2e_1}(h)$ and $t_{d_2e_2}(h)$ (Fig. 6.12). This suggests that partial dolomite diagenetic facies d_2 is separated from subtidal depositional facies e_1 by a nearly constant thickness of 0.3 m and that partial dolomite diagenetic facies d_2 is separated from intertidal depositional facies

e_2 by a nearly constant thickness of 1 m (i.e., the first maxima of transiograms $t_{d_2e_1}(h)$ and $t_{d_2e_2}(h)$; Figure 6.12).

The auto- and cross-transiograms of the diagenetic facies themselves are now fitted using the same procedure. The parameters controlling these transiograms are the parameters of the third covariance r_3 and b_3 (Eq. 6.A.5), and all the other parameters mentioned above, which are left unchanged. They control the spatial properties of Z_3 and thus the geometries of diagenetic facies. Figure 6.13 shows the fit between experimental and theoretical transiograms. The method is able to capture the asymmetry of cross-transiograms between the two diagenetic facies as $t_{d_2d_1}(h)$ and $t_{d_1d_2}(h)$, showing that the dolomitic crust diagenetic facies d_1 tends to overlie the partial dolomite diagenetic facies d_2, and the modelled transiograms are able to match exactly this behavior at the origin (Fig. 6.13). Theoretical auto-transiograms $t_{d_1d_1}(h)$ and $t_{d_2d_2}(h)$ also exhibit the correct behavior at the origin, which confirms that the mean thicknesses of these diagenetic facies are well constrained (Fig. 6.13).

This section has shown the value of the method for capturing complex transiograms between depositional facies and diagenetic facies. Shifts α_{13} and α_{23} play an important role, which emphasizes the value of incorporating asymmetry in the modelling of syn-depositional diagenetic patterns.

Simulation

The simulation is performed as for previously described models (e.g., Figure 6.8), with the added third Gaussian random function. Two realizations of the Earth model showing diagenetic facies superimposed on depositional facies are shown in Figure 6.14. Both realizations honor the data along the measured sections (e.g., long measured section N22; Figure 6.14), but differ away from them (e.g., in the volume above measured section N22; Figure 6.14).

To verify that the resulting simulations honor the data statistics, transiograms are computed on three realizations (thin grey curves in Figure 6.12 and Figure 6.13). The simulated transiograms match the experimental transiograms quite well, even better than the theoretical

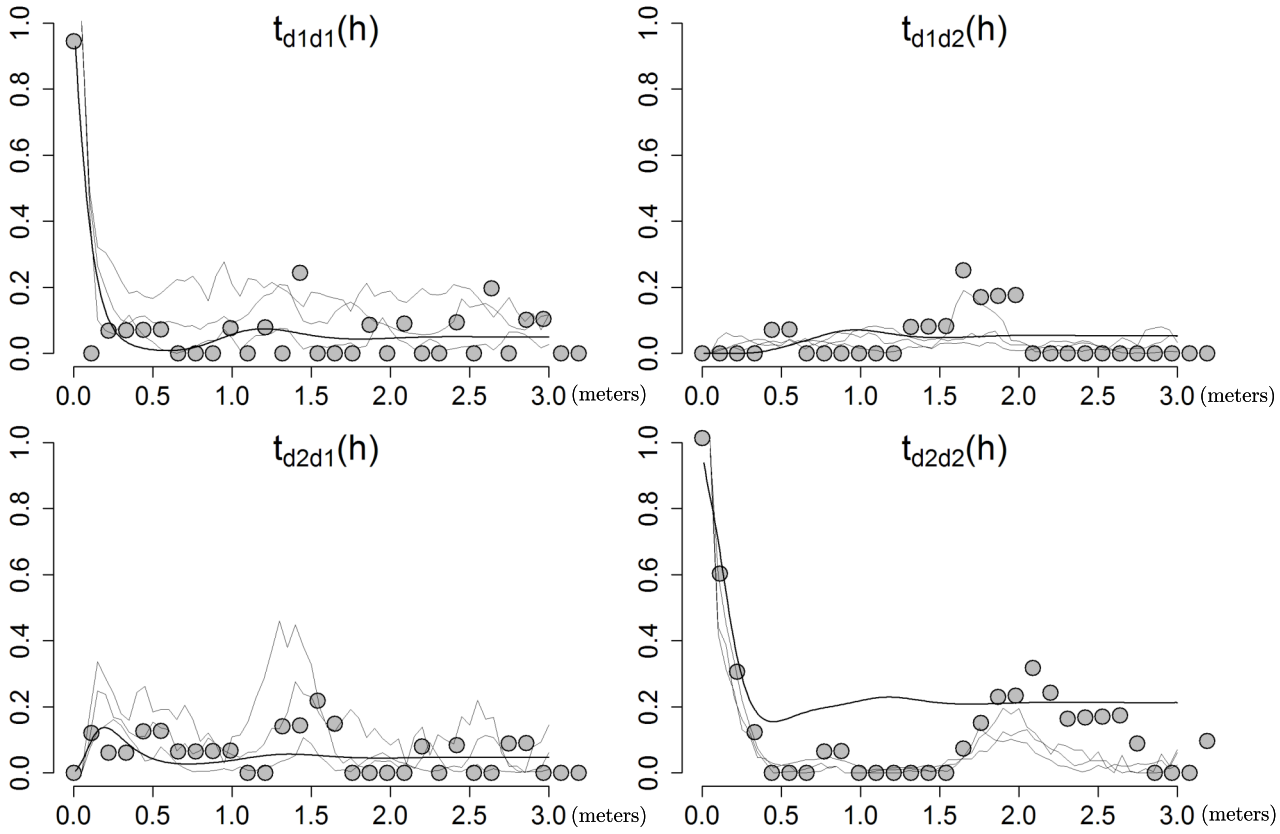

Figure 6.13: Experimental transiograms between diagenetic facies (grey points), theoretical transiograms fitted to these points (black lines), and transiograms computed in three realizations of a resulting Earth model (thin grey lines). The parameters defining the theoretical transiograms are the same as those for Figure 6.7 and 6.12, with in addition $r_3 = (800, 800, 0.3)$ m and $b_3 = 0$ m^{-1} (Eq. 6.A.4c).

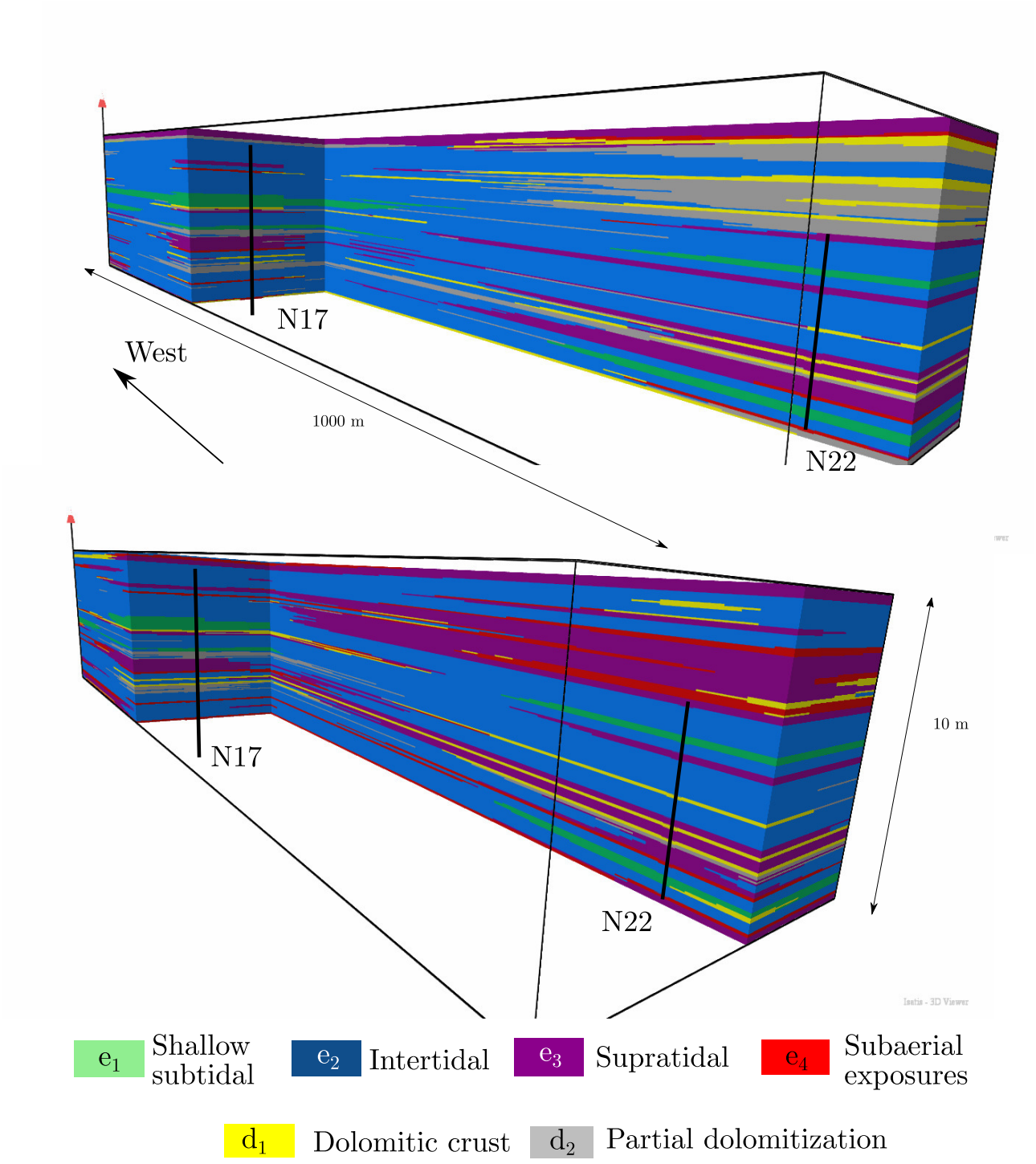

Figure 6.14: Two realisations of an Earth model for depositional facies and diagenetic facies in the Cimon Latemar region of the Latemar carbonate platform, conditioned by four measured sections with modelling parameters noted in Figure 6.7, 6.12 and 6.13.

transiograms. For instance, transiograms $t_{d_2e_2}(h)$ for the realizations reproduce the complex hole-effect observed in the data (Fig. 6.12). Similarly, transiogram $t_{d_2d_2}(h)$ of the realizations follows the experimental transiogram more closely than the theoretical transiogram (Fig. 6.13). This could be due to the conditioning of the simulation, which provides significant constraints on the Earth models.

6.5.2 Modelling Syn-Depositional Diagenesis in Non-Stationary Shallow-Marine Deposits, Book Cliffs, Utah

The Upper Cretaceous Spring Canyon Member of the Blackhawk Formation, which is exposed in the Book Cliffs (Utah), consists of shallow-marine, wave-dominated shoreface sandstones that contain overprinting diagenetic features such as carbonate-cemented concretions and leached zones (whitecaps) (Van Wagoner et al., 1990; Kamola and Huntoon, 1995; Hampson and Storms, 2003; Taylor et al., 2004). Due to their large lateral extent, the deposits display non-stationary facies proportions from proximal to distal. Herein we model the outcrop dataset to show the flexibility of the method and highlight the use of embedded transition probabilities in a non-stationary context.

Dataset

The nine measured sections reported by Taylor et al. (2004) are used here, and the facies classification is simplified into three depositional facies: distal lower shoreface heteroliths and offshore mudstones (E_1), proximal lower shoreface sandstones (E_2) and foreshore and upper shoreface sandstones (E_3). There are also two diagenetic facies: carbonate cement D_1 and leached sandstones ("whitecaps") D_2, in which carbonate material has been removed via syn-depositional diagenesis. Table 6.2 shows the proportion of each diagenetic facies within the different depositional facies, based on measured sections with this facies classification (Fig. 6.15).

No cyclicity is observed between depositional facies. Facies proportions in each measured section (represented by pie charts in Figure 6.15) show that from west (proximal) to east (distal), the

Table 6.2: Proportions of diagenetic facies overprinted on depositional facies in the Spring Canyon Member of the Blackhawk Formation, taken from measured sections (Fig. 6.15).

	Carbonate concretion	**White caps**
Distal mudstones	0	0
Shoreface sandstones	0.21	0.03
Foreshore sandstones	0.59	0.4

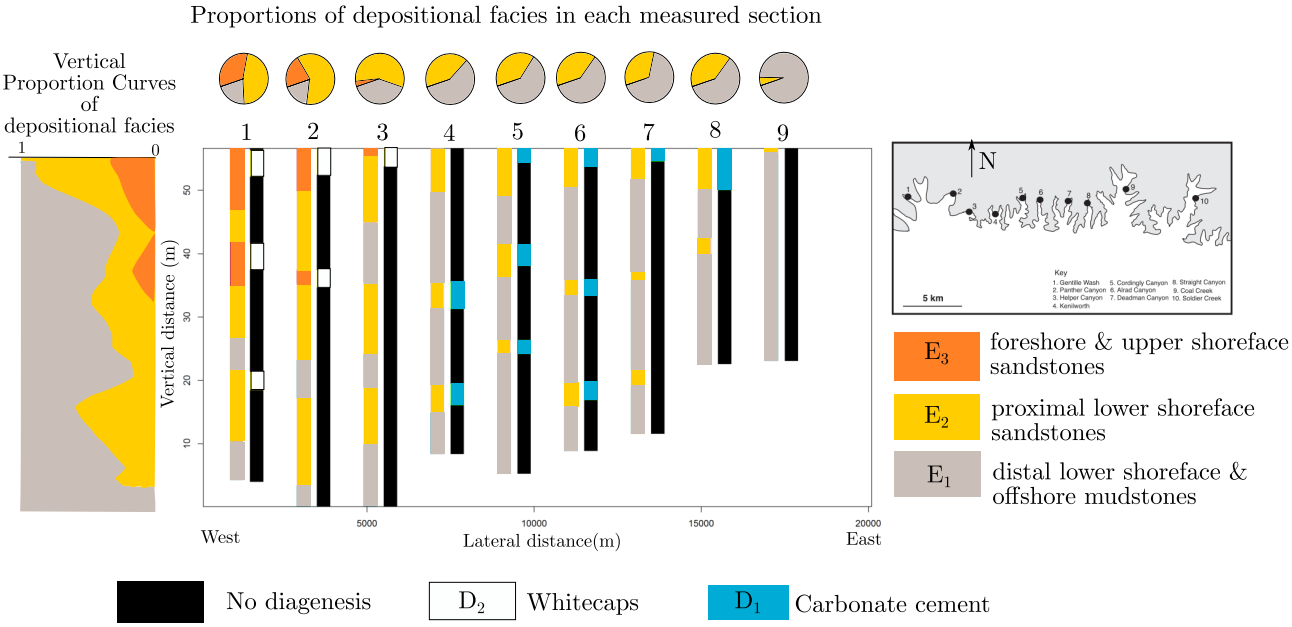

Figure 6.15: Measured sections through the Spring Canyon Member, Blackhawk Formation in outcrops of the Book Cliffs, as reported by Taylor et al. (2004), with simplified classification of depositional facies and diagenetic facies, corresponding facies vertical proportion curves, and pie charts of facies proportions in each measured section.

proportion of depositional facies E_3 decreases while that of depositional facies E_1 increases. Vertical facies proportion curves show that depositional facies E_3 is only present at the top of the Spring Canyon Member in the area sampled by the measured sections. Diagenetic facies are also non-stationary because their distribution is controlled by the distribution of depositional facies (Table 6.2).

Modelling Non-Stationary Facies Proportions

As described above, facies proportions vary systematically over the dataset to be modelled (Fig. 6.15). Therefore, the final Earth model should account for these variations. This is achieved by estimating the proportions of each facies in each cell of the Earth model. (Armstrong et al., 2011; D'Or et al., 2017). First, the proportions of each facies are computed at each horizontal level from all the measured sections to give vertical facies proportion curves (Fig. 6.15). The vertical proportion curves are then smoothed with a moving average algorithm to remove random variations, as described in White et al. (2003). Then, the proportions of each facies are computed at each vertical measured section (pie charts of Figure 6.15). Finally, at each grid cell intersecting a measured section, the proportion of each facies is calculated by averaging the proportion given by the vertical proportion curve with the proportion of the facies at the measured section.

A procedure to interpolate these facies proportions between measured sections is then required. Here this is achieved by lateral simple kriging interpolation (Chiles and Delfiner, 2012) using a Gaussian covariance with a large scale factor and a mean chosen as the global proportion of each facies. Once the proportions of each facies have been calculated for every cell of the model, they are transformed into thresholds for the Gaussian random functions according to the same procedure used for the models presented earlier (Appendix, Eq. 6.A.8).

The Model

The truncation rule can be inferred from the observation of facies contacts in the measured sections (Fig. 6.15). Because of the facies distribution's non-stationarity, the truncation rule is different in every cell and depends on the cell's facies proportion. Therefore, a general truncation rule is first defined in Figure 6.16, which is then adapted to the local facies proportions in the different cells of the Earth model (Fig. 6.16). The foreshore and upper shoreface sandstone depositional facies (E_3) and distal lower shoreface heteroliths and offshore mudstone depositional facies (E_1) are not in contact, because of a limited presence of foreshore and upper shoreface sandstones (which occur only five times in the measured sections) and non stationarity (Fig. 6.15). However, there is no reason why these facies should not be in contact away from the measured sections, and the global truncation rule is thus defined to allow this contact relationship (Fig. 6.16). The carbonate cement diagenetic facies (D_1) and leached sandstone diagenetic facies (D_2) are respectively present in the proximal lower shoreface sandstone depositional facies (E_2) and both the proximal lower shoreface sandstone depositional facies and the foreshore and upper shoreface sandstone depositional facies (E_2, E_3) (Fig. 6.16).

Transiograms are not fitted here because their behavior is strongly influenced by non stationarity, especially at long distances (Armstrong et al., 2011). However, embedded transition probabilities (Krumbein and Dacey, 1969) are not much affected by non stationarity because they just measure facies juxtapositions. They can be deduced from the parameters of the model by taking the derivative at the origin of the transiograms (Eq. 6.A.13). Thus, they are compared to the experimental embedded transitions computed from the measured sections in order to infer the parameters α_{12} and β_{12}. The experimental (red) and model (blue) embedded matrix for the three depositional facies after fitting is

$$R_{logs/model} = \begin{bmatrix} E_1 & E_2 & E_3 \\ 0 & 1.0/0.63 & 0.0/0.36 \\ 0.72/0.79 & 0 & 0.28/0.23 \\ 0.0/0.15 & 1.0/0.85 & 0 \end{bmatrix}. \tag{6.1}$$

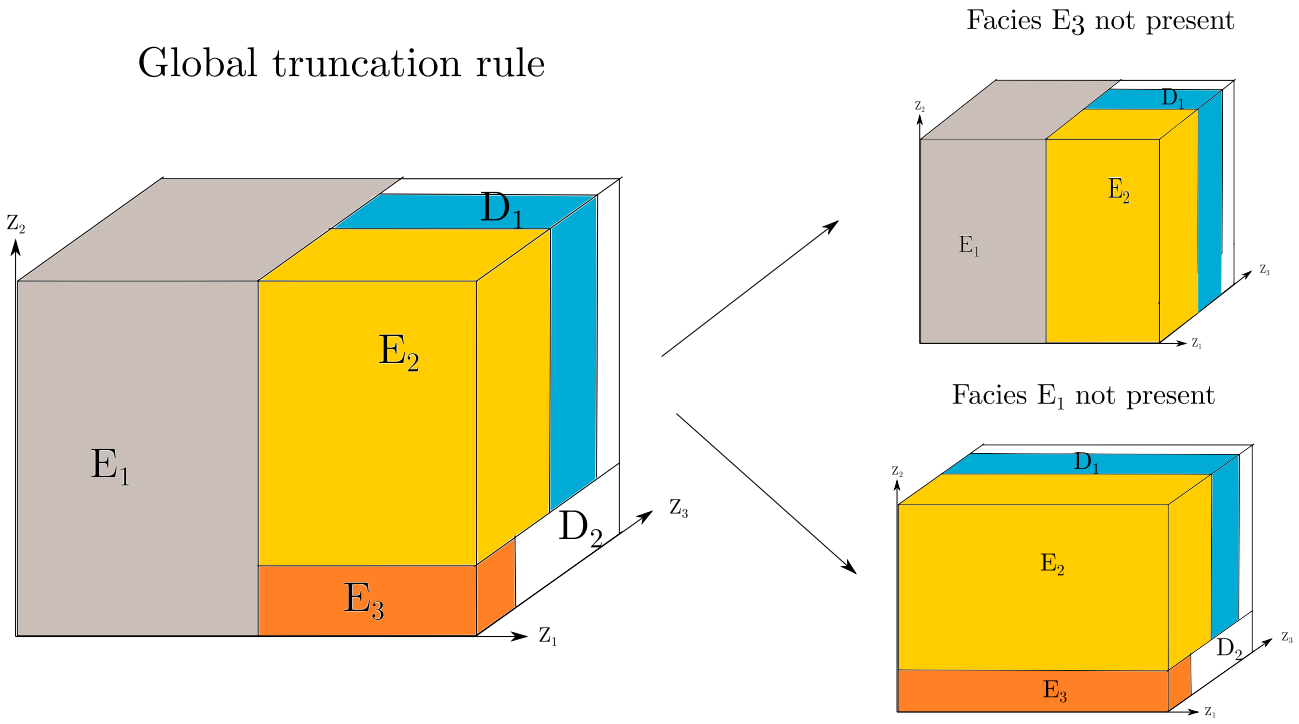

Figure 6.16: Global truncation rule and two examples of local truncation rules for modelling the Spring Canyon Member, Blackhawk Formation in outcrops of the Book Cliffs. The facies E are depositional facies and D are diagenetic facies.

The matrix shows that foreshore and upper shoreface sandstones (E_3) and distal lower shoreface heteroliths and offshore mudstones (E_1) are not in contact in the measured sections because their embedded probability is zero, while in the model they can be in contact (r_{31}=0.15, r_{13} = 0.36) according to the truncation rule (Fig. 6.16). The embedded transitions from proximal lower shoreface sandstones (E_2) to the other depositional facies are similar in the model and in the measured sections.

In order to constrain the vertical component of the scale factors r_1 and r_2, the thicknesses of the depositional facies are computed in the measured sections and matched with the theoretical thicknesses, which are obtained from the derivative at the origin of the auto-transiograms (Carle and Fogg, 1996). The resulting theoretical thicknesses for the three depositional facies E_1, E_2, and E_3 are respectively 1.3 m, 0.8 m, and 0.5 m, while the experimental thicknesses computed from the measured sections are 1.4 m, 0.8 m, and 0.6 m, which is a good match.

Embedded transition probabilities between the diagenetic facies are not shown because they are simply not in contact with each other. The vertical scale factor r_3 is chosen to be similar

to r_1 and r_2 because diagenetic facies have a similar thickness to depositional facies. Lateral components of the scale factors r_1, r_2 and r_3 are chosen by visual comparison of the resulting Earth model realizations and the correlation panel between measured sections of Taylor et al. (2004). The depositional facies have a large lateral extent, of the same order as the west-to-east lateral extent of the Earth model.

Simulation

The number of cells in the grid in each direction is 100 (west-to-east), 20 (north-to-south), 566 (height) and the dimensions of the grid are 20 km (∼12.4 mi) (west-to-east), 5 km (∼3.1 mi) (north-to-south), 56 m (∼184 ft) (height). The simulations are conditioned to the measured sections with the procedure outlined in Le Blévec et al. (2018).

Two realizations of the resulting Earth model are shown in Figure 6.17. It is clear that the realizations are non-stationary as, for instance, the proportion of foreshore and upper shoreface sandstone depositional facies (E_3) decreases towards the west. Leached sandstone diagenetic facies (D_2) also exhibit a decreasing proportion towards the west, because they are constrained by the presence of foreshore and upper shoreface sandstone depositional facies (E_3) (Table 6.2).

As a post-validation step, embedded transition probabilities are computed in three resulting realizations and averaged, to give the embedded matrix of transition probabilities

$$R_{simu} = \begin{bmatrix} E_1 & E_2 & E_3 \\ 0 & 0.75 & 0.25 \\ 0.79 & 0 & 0.21 \\ 0.06 & 0.94 & 0 \end{bmatrix}. \tag{6.2}$$

This matrix matches the embedded matrix computed from the measured sections (Eq. 6.1), although foreshore and upper shoreface sandstone depositional facies (E_3) and distal lower shoreface heteroliths and offshore mudstone depositional facies (E_1) are in contact, as discussed above.

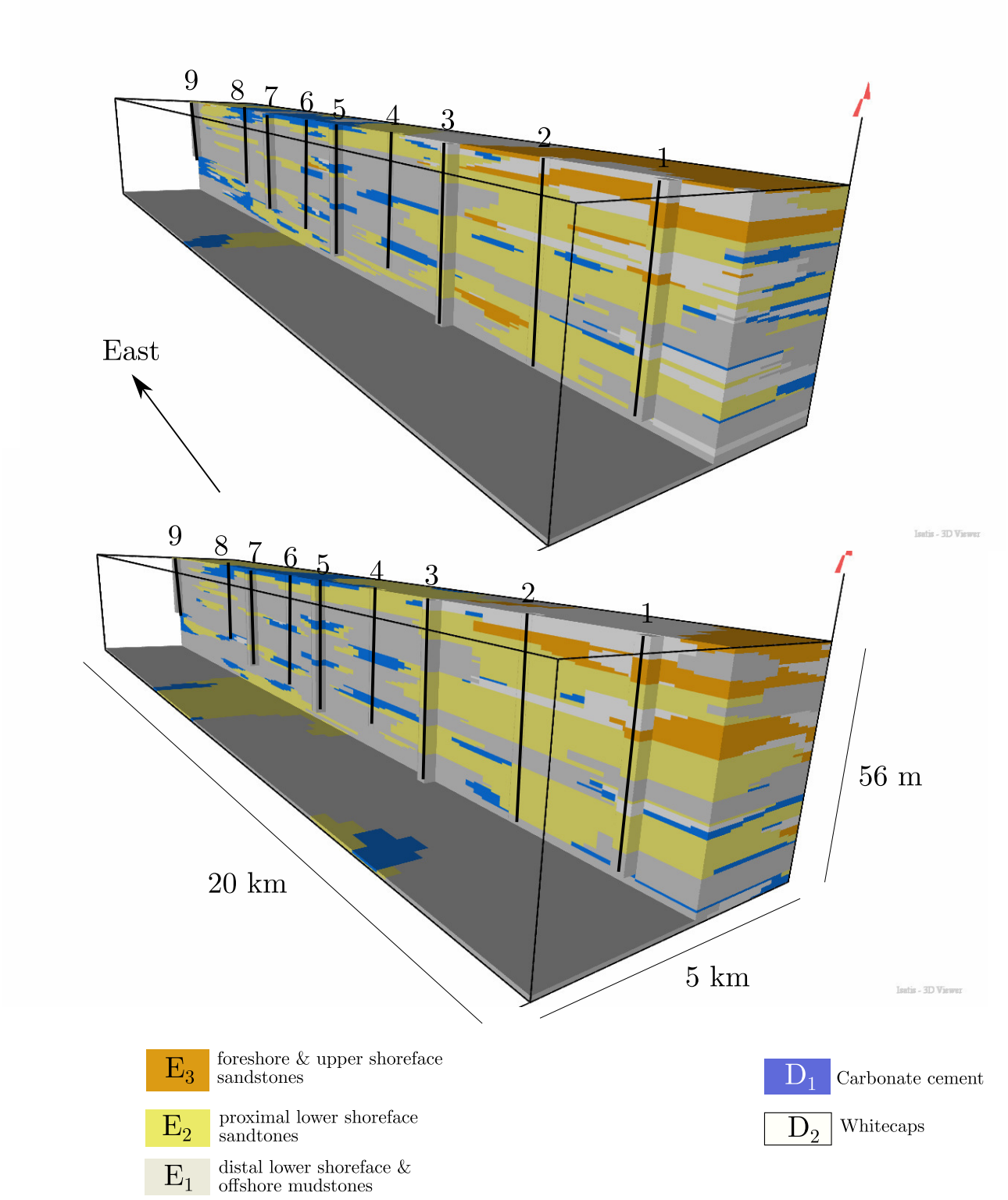

Figure 6.17: Two realizations of an Earth model for depositional facies and diagenetic facies in the Spring Canyon Member, Blackhawk Formation, conditioned by nine measured sections with modelling parameters $r_1 = (0.6, 3000, 3000)$ m, $r_2 = (0.7, 3000, 3000)$ m, $r_3 = (1, 1500, 1500)$ m, $b_1 = b_2 = 0$ m^{-1}, $\alpha_{12} = \alpha_{13} = \alpha_{23} = 0$ m, $\beta_{12} = \beta_{13} = \beta_{23} = 0$ (Eqs. 6.A.3, 6.A.4a, 6.A.4b, 6.A.4c).

6.5.3 Towards Modelling Post-depositional Hydrothermal Diagenesis

Post-depositional hydrothermal diagenesis is commonly observed at outcrop (Jacquemyn et al., 2014; Vandeginste et al., 2013; Beckert et al., 2015) and interpreted in the subsurface (Davies and Smith Jr, 2006; Smith Jr, 2006). Hydrothermal diagenesis produces diagenetic bodies that are discordant with strata and instead follow faults, fractures and other structures. Depositional facies may differ in their permeability, such that hydrothermal fluids can also flow laterally away from faults and fractures along relatively permeable facies belts and bodies, thus creating so-called "Christmas tree" geometries (Beckert et al., 2015). For example, outcrops of the Latemar carbonate platform in Valsorda valley exhibit such fracture-related hydrothermal diagenesis, which generate dolomite that is distributed along and nearby to fractures (Fig. 6.18, after Jacquemyn et al. (2014)).

This type of dolomitization can be represented in our method thanks to the third Gaussian random function covariance $\rho_3(h)$, which can have a different anisotropy from that of the two other Gaussian random functions covariances (Eq. 6.A.4c). An unconditional realization of such a model is shown in Figure 6.19. The third Gaussian random function is modelled independently from the two other Gaussian random functions ($\beta_{13} = \beta_{23} = 0$), so that the geometries of diagenetic dolomite bodies cut across depositional facies geometries. The truncation rule controls the extent of dolomite within each depositional facies (Fig. 6.19). Depositional facies E_3 contains more dolomite than depositional facies E_2, because the volume of dolomitized facies D_{E_3} in the truncation rule is larger that of dolomitized facies D_{E_2}. On the contrary, depositional facies E_1 is not affected by diagenesis.

The Earth model realization (Fig. 6.19) shows that depositional facies tend to be organized in shallowing-upward asymmetric cycles and diagenetic dolomite bodies cut across them. The dolomite diagenetic facies (D_{E_2} and D_{E_3}) is more abundant in depositional facies E_3 than in depositional facies E_2, and is not present at all in depositional facies E_1, as constrained by the truncation rule.

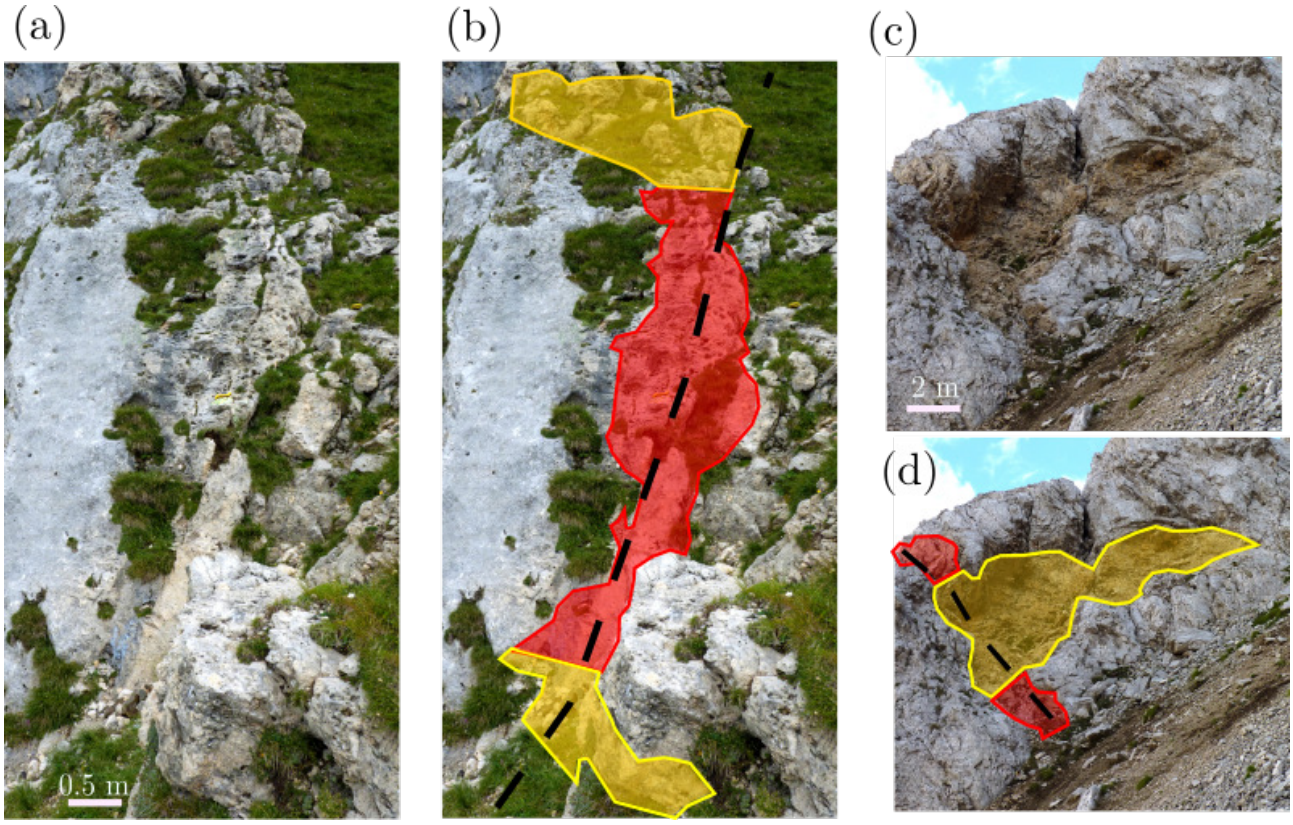

Figure 6.18: Uninterpreted (a) and (c); and interpreted (b) and (d) photographs of post-depositional hydrothermal dolomite associated with fractures in the Valsorda valley outcrops of the Latemar carbonate platform. Hydrothermal dolomite confined to the fracture area is shown in red, and hydrothermal dolomite expanding in the host rock is shown in yellow. Modified from Jacquemyn et al. (2014).

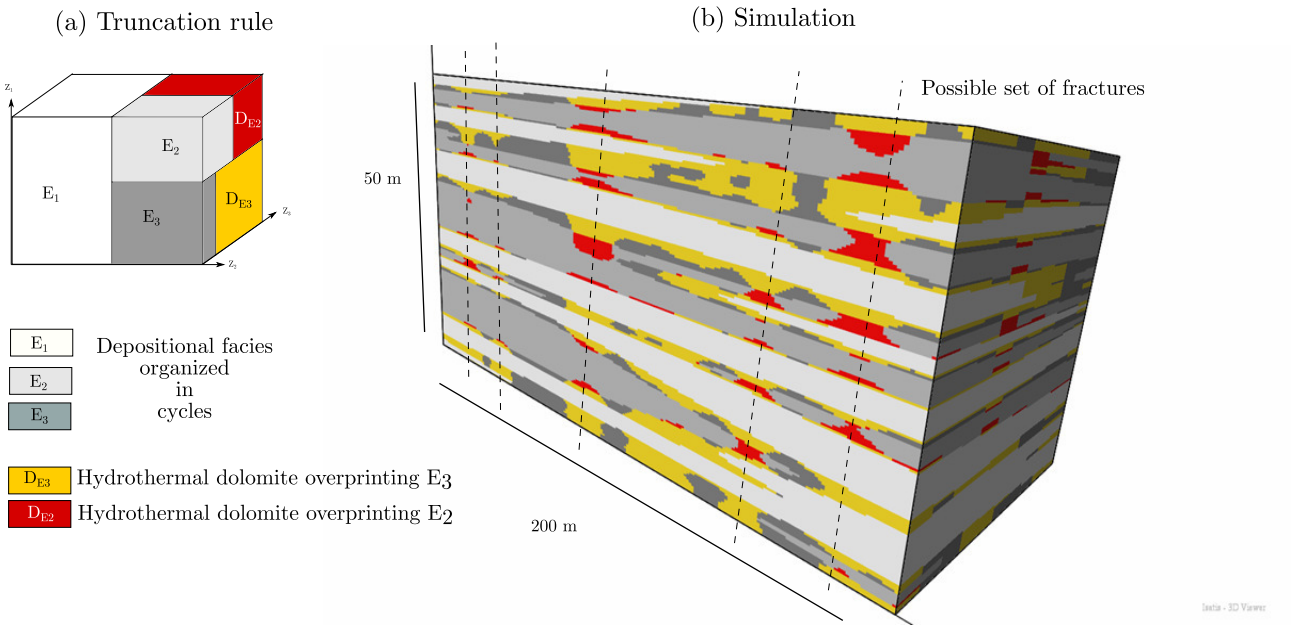

Figure 6.19: (a) Truncation rule and (b) resulting unconditional realization of Earth model of depositional facies (cf. Figure 6.8) overprinted by post-depositional hydrothermal dolomite diagenetic facies. The parameters used for the simulation are $r_1 = r_2 = (60, 60, 0.2)$ m, $r_3 = (5, 5, 5)$ m, $b_1 = b_2 = b_3 = 0$ m^{-1}, $\beta_{12} = 0.99$, $\alpha_{12} = 0.1$ m, $\beta_{13} = 0.8$, $\beta_{23} = 0$, $\alpha_{13} = \alpha_{23} = 0$ m (Eqs. 6.A.3, 6.A.4a, 6.A.4b, 6.A.4c).

6.6 Conclusion and Recommendations

The new method proposed in this paper models depositional and diagenetic facies fields with cyclic and rhythmic patterns. The method is based on a novel Pluri-Gaussian approach, using three dimensional truncation rules and Gaussian random functions shifted from each other. Qualitative information and concepts are used to construct the truncation rule, and the other parameters of the method are defined by fitting the experimental auto- and cross- transiograms. The resulting models show that a combination of lateral and vertical facies cyclicity can be used to generate aggradational and progradational facies geometries.

In addition, we model depositional facies overprinted by cross-cutting or conformable diagenesis. This is possible because the three Gaussian random functions are spatially shifted from each other, and depositional and diagenetic facies are ordered according to the cross-transiograms.

The method has also shown its capability to model non-stationary facies proportions, which is a predominant feature in datasets that contain pronounced proximal-to-distal or axial-to-marginal facies trends. In such cases, it is not appropriate to use transiograms to constrain the

parameters of the method. Instead, it is suggested to use embedded transition probabilities, because non stationarity does not significantly impact facies juxtapositions.

The method significantly improves the capability of geostatistical Earth models to represent geologically realistic facies architectures, and thus can lead to more realistic geostatistical reservoir models and more accurate hydrocarbon production forecasts.

6.A Appendix: Shifted Pluri-Gaussian Model

The model developed in this paper is an extension of that developed by Le Blévec et al. (2018). Three Gaussian random functions Z_1, Z_2, Z_3 are correlated and shifted relative to each other and truncated into facies according to a truncation rule (e.g., Figure 6.11). The first two Gaussian random functions control depositional facies while the third Gaussian random function controls diagenetic facies. A shifted version of the linear model of co-regionalization (Wackernagel, 2003) is used

$$\begin{cases} Z_1(x) = Y_1(x), \\ Z_2(x) = \beta_{12}\ Y_1(x+\alpha_{12}) + \sqrt{1-\beta_{12}^2}\ Y_2(x), \\ Z_3(x) = \beta_{13}\ Y_1(x+\alpha_{13}) + \beta_{23}\ Y_2(x+\alpha_{23}) + \sqrt{1-\beta_{13}^2-\beta_{23}^2}\ Y_3(x), \end{cases} \tag{6.A.3}$$

where $-1 < \beta_{ij} < 1$ are the correlations coefficients between $Y_i(x+\alpha_{ij})$ and $Z_j(x)$, α_{ij} being the shifts, and Y_1, Y_2, Y_3 are uncorrelated Gaussian random functions with respective covariances in three dimensions

$$\rho_1(h_x, h_y, h_z) = \exp\Big(-\frac{h_x^2}{r_{1x}^2} - \frac{h_y^2}{r_{1y}^2} - \frac{h_z^2}{r_{1z}^2}\Big)\ \cos(b_1\ h_z), \tag{6.A.4a}$$

$$\rho_2(h_x, h_y, h_z) = \exp\Big(-\frac{h_x^2}{r_{2x}^2} - \frac{h_y^2}{r_{2y}^2} - \frac{h_z^2}{r_{2z}^2}\Big)\ \cos(b_2\ h_z), \tag{6.A.4b}$$

$$\rho_3(h_x, h_y, h_z) = \exp\Big(-\frac{h_x^2}{r_{3x}^2} - \frac{h_y^2}{r_{3y}^2} - \frac{h_z^2}{r_{3z}^2}\Big)\ \cos(b_3\ h_z), \tag{6.A.4c}$$

with $r_i = (r_{ix}, r_{iy}, r_{iz})$ the scale factors in three dimensions and b_i the frequencies of the cosine functions. Therefore, the auto-covariances of the three Gaussian random functions Z_1, Z_2, Z_3 are respectively

$$\begin{cases} \rho_{Z_1}(h) = \rho_1(h), \\ \rho_{Z_2}(h) = \beta_{12}^2 \ \rho_1(h) + (1 - \beta_{12}^2) \ \rho_2(h), \\ \rho_{Z_3}(h) = \beta_{13}^2 \ \rho_1(h) + \beta_{23}^2 \ \rho_2(h) + (1 - \beta_{13}^2 - \beta_{23}^2) \ \rho_3(h), \end{cases} \tag{6.A.5}$$

and the cross-covariances between them

$$\begin{cases} \rho_{Z_1 Z_2}(h) = \beta_{12} \ \rho_1(h + \alpha_{12}), \\ \rho_{Z_1 Z_3}(h) = \beta_{13} \ \rho_1(h + \alpha_{13}), \\ \rho_{Z_2 Z_3}(h) = \beta_{12} \ \beta_{13} \ \rho_1(h + \alpha_{13} - \alpha_{12}) + \beta_{23} \ \sqrt{1 - \beta_{12}^2} \ \rho_2(h + \alpha_{23}). \end{cases} \tag{6.A.6}$$

These covariances are used to derive the thresholds of the Gaussian random functions from the proportions of the different facies. For instance, let us determine the threshold q_{d_1} of the third Gaussian random function Z_1 that controls the proportion of the facies d_1 (Fig. 6.11)

$$p_{d1} = Pr[Z_1(x) > q_1, Z_2(x) < q_3, Z_3(x) > q_{d1}], \tag{6.A.7}$$

which can be re-written by integration of the multi-variate Gaussian density $G_\Sigma(u, v, w)$

$$p_{d1} = \int_{q_1}^{\infty} \int_{-\infty}^{q_2} \int_{q_{d1}}^{\infty} G_\Sigma(u, v, w) \ du \ dv \ dw, \tag{6.A.8}$$

with Σ the covariance matrix

$$\Sigma = \begin{bmatrix} 1 & \rho_{Z_1 Z_2}(0) & \rho_{Z_1 Z_3}(0) \\ \rho_{Z_1 Z_2}(0) & 1 & \rho_{Z_2 Z_3}(0) \\ \rho_{Z_1 Z_3}(0) & \rho_{Z_2 Z_3}(0) & 1 \end{bmatrix}. \tag{6.A.9}$$

Equation 6.A.8 is then solved numerically with the algorithm of Genz (1992). The same methodology is applied to compute theoretical transiograms (Fig. 6.7). For instance, let us examine the transiogram between facies e_1 and e_2 (Fig. 6.11)

$$t_{e1e2}(h) = \frac{Pr[Z_1(x) < q_1, Z_2(x) < q_2, Z_1(x+h) < q_1, Z_2(x+h) > q_2]}{p_{e1}}, \tag{6.A.10}$$

which can be re-written by integration of Gaussian multi-variate density

$$t_{e1e2}(h) = \frac{1}{p_{e1}} \int_{-\infty}^{q_1} \int_{-\infty}^{q_2} \int_{-\infty}^{q_1} \int_{q_2}^{\infty} G_{\Sigma(h)}(u, v, w, y)\, du\, dv\, dw\, dy, \tag{6.A.11}$$

with $\Sigma_{(h)}$ the Gaussian covariance matrix

$$\Sigma(h) = \begin{bmatrix} 1 & \rho_{Z_1Z_2}(0) & \rho_{Z_1}(h) & \rho_{Z_1Z_2}(h) \\ \rho_{Z_1Z_2}(0) & 1 & \rho_{Z_2Z_1}(h) & \rho_{Z_2}(h) \\ \rho_{Z_1}(h) & \rho_{Z_2Z_1}(h) & 1 & \rho_{Z_1Z_2}(0) \\ \rho_{Z_1Z_2}(h) & \rho_{Z_2}(h) & \rho_{Z_1Z_2}(0) & 1 \end{bmatrix}. \tag{6.A.12}$$

Equation 6.A.11 is then solved numerically with the algorithm of Genz (1992) and the same methodology is applied for the other transiograms. The embedded transition probabilities are computed from the transiograms as follows

$$r_{ij} = -\frac{t'_{ij}(0)}{t'_{ii}(0)}. \tag{6.A.13}$$

Chapter 7

Discussion and Recommendations

7.1 Quantification of Cyclicity and Rhythmicity

In this thesis, the notions of facies cyclicity and facies rhythmicity have been defined and quantified. This was performed with a two-point statistical tool derived from Markov Chains, the transiogram (Carle and Fogg, 1996). Markov Chain analysis has already been used in geology to quantify facies cyclicity (e.g., Gingerich, 1969; Hattori, 1976). These authors use transition probability matrices to validate that the transitions between facies are non-random, which allows them to determine facies cycles in their case studies. More recently, a method also based on transition probabilities was developed by Burgess (2016) to quantify facies ordering and trends in facies thicknesses. In his study, the vertical successions do not show significant facies ordering, which suggests that although facies cyclicity and rhythmicity are often interpreted by geologists, they might not always be legitimate. Thus, Burgess (2016) encourages authors to quantify facies ordering in datasets before interpreting facies cyclicity. The presence of cyclicity depends obviously on the facies classification used. In this thesis, it was shown that vertical facies successions in the Latemar carbonate platform are partially cyclic when facies were grouped into facies associations representing environments of deposition. In contrast to the two approaches described above, the aim of the method developed here is not to check whether facies cyclicity is present, but to quantify the juxtapositions between facies and re-

produce them in Earth models. This is achieved by reproducing the tangents at the origin of the transiograms with Shifted Pluri-Gaussian Simulations, which are equivalent to transition probabilities between facies.

A major limitation of Markov Chains and two-point statistics is not discussed in the geological literature. These tools cannot quantify probabilities of obtaining symmetrical facies cycles of the type A-B-C-B-A or other complex cycles. In such a cycle, the facies A and B appear twice in the opposite vertical order, which would give equal transition probabilities between them in the upward and downward direction, as if they were not ordered. However, in that case, it simply means that the ordering is more sophisticated and cannot be quantified by Markov Chains or two-point statistics. This issue could be tackled by using second order Markov Chains (e.g., Shamshad et al., 2005), which quantify the probability of two successive transitions. In this case, they would be able to quantify the probability of transitions A-B-C and C-B-A and thus the probability of the full symmetrical cycle. Similarly, instead of two-point statistical tools such as the transiogram, higher-order statistics would be able to quantify such cycles. Multi-Point Statistics should be able to reproduce such cycles, but obtaining the appropriate three-dimensional training image seems difficult. Therefore, more work should be carried out in geology and geostatistics to quantify more complex orderings between facies and reproduce them in Earth models.

In geology, rhythmicity is a notion that has been quantified principally with spectral analysis in order to understand the origin of facies repetitions in the stratigraphic record (e.g., De Boer and Wonders, 1984; House, 1985; Herbert and Fischer, 1986). Here, the origin of rhythmicity is not considered but its characteristics in relation to the probability density function (pdf) of facies cycle thicknesses are investigated. Rhythmicity is quantified by pseudo-oscillations of transiograms or variograms, called hole-effects. The first step towards understanding the impact of facies cycle thicknesses on hole-effects was conducted by Jones and Ma (2001) experimentally. They noted that as the coefficient of variation for the facies thickness pdf decreases, the hole-effect is more pronounced. In my thesis, the link between hole-effects and facies thickness is formally established by using renewal processes theory (Matheron, 1968) (Appendix A). This confirms mathematically the relation observed experimentally by Jones and Ma (2001)

in the specific case of facies thickness with Gamma pdf. Further work should be carried out by using this relation (Appendix A) with a range of different pdfs in order to improve the understanding of hole-effects. Hole-effects have also been observed at the pore scale from CT scan images of rock samples (Mosser et al., 2018), which shows that they are an important aspect of geostatistics that perhaps did not receive enough attention.

The quantification of cyclicity and rhythmicity with transiograms that has been developed here can be used as a stand-alone tool to constrain other geostatistical techniques than Pluri-Gaussian Simulations. For instance, in the literature review (Chapter 2), I have shown that authors sometimes use Multi-Point Statistics with training images that do not represent the asymmetry between facies observed in a conceptual model. Computing transiograms on the training image and comparing them to those of the conceptual model or the studied data would help to ensure the consistency of the training image. Similarly, with object-based methods, computing two-point statistics of facies realisations would help to check that they honour the input data. If not, it might be because the parameters of the object-based method are ill-chosen, or that there are specific relationships between facies that the object-based method is not able to reproduce. Therefore, two-point statistical tools can be used to check the consistency of geostatistical realisations. In light of the work documented here on facies cyclicity and rhythmicity, it would be interesting to check that other geostatistical methods are able to create facies Earth models with cyclicity and rhythmicity by investigating the resulting two-point statistics.

7.2 Modelling Spatial Patterns of Depositional and Diagenetic Facies in Carbonate Reservoirs

In the literature review of this thesis (Chapter 2), it was seen that many geostatistical methods were originally designed to model siliciclastic shallow-marine reservoirs. Therefore, this research originally aimed at creating new algorithms for modelling shallow-marine carbonate reservoirs. One of the challenging aspect of carbonates is that facies geometries at inter-well

scale are poorly defined. This is an issue for object-based methods (Deutsch and Tran, 2002) or Multi-Point Statistics (Strebelle, 2002), which require respectively facies geometries and three dimensional training images. Moreover, Sequential Indicator Simulation (Alabert, 1989) models facies independently, which does not allow to account for spatial relationships between facies. On the other hand, Pluri-Gaussian Simulations (PGS) (Armstrong et al., 2011) reproduce facies contacts thanks to the truncation rule and do not require exact facies geometries. Similarly, Markov Chain transiograms (Carle and Fogg, 1996) are able to statistically reproduce the facies transition rates inferred from input data. The method proposed in this thesis combines these two approaches, and thus has great potential for modelling carbonate reservoirs.

In geostatistical modelling, it is important to make the most of the available data, for instance by quantification of measured sections that constitute input data. This can be performed with two-point statistical tools such as the variogram or the transiogram. As shown in this thesis, the transiogram is more relevant than the variogram, because of its capacity to quantify cyclicity, which is often reported in carbonate successions (e.g., Lindsay et al., 2006; Kenter et al., 2006). In the literature review (Chapter 2), most case studies of geostatistical modelling in carbonate reservoirs did not show the fit between experimental and model transiograms. In the absence of such fitting, facies geometrical properties such as facies proportions, mean thicknesses, rhythmicity and cyclicity may not be reproduced in the simulated Earth model. For this reason, the research presented here always presents the fit between experimental and modelled transiograms, which is reasonable in most case studies. As discussed above, if another modelling method is used, it is still recommended to check whether the Earth model realizations fit the experimental transiograms.

The modelling approach developed here, the Shifted PGS, is able to jointly model facies cyclicity and rhythmicity, which has not been accomplished with other geostatistical methods. Multi-Point Statistics could possibly model these concepts, but obtaining a three-dimensional training image displaying cyclicity and rhythmicity appears to be too complex. Therefore, Shifted PGS is probably the most appropriate method to model carbonate reservoirs that contain metre-scale cycles (e.g., Kenter et al., 2006; Lindsay et al., 2006). Of course, the approach is also valid for shallow-marine siliciclastic reservoirs if they contain facies cyclicity or rhythmicity. Shifted

PGS could also be improved in order to improve the fit between all the transition rates and higher-order statistics. As mentioned above, constraining high-order statistics might help in modelling more complex patterns than the cycles considered in this thesis. This could be done by using non parametric truncation rules (Deutsch and Deutsch, 2014) or high dimensional truncation rules (Maleki et al., 2016) and developing automatic procedures such as the one of Desassis et al. (2015).

In order to introduce more geological realism in carbonate Earth models, stratigraphic forward models (e.g., Burgess et al., 2001; Warrlich et al., 2008) seem a potentially fruitful tool. Such methods are interesting because they produce facies contacts and geometries that honour geological concepts such as sequence stratigraphy. However, these methods have also great limitations: the corresponding facies Earth models cannot fit hard input data such as vertical facies successions (i.e., in measured sections and wells), and the method cannot generate multiple realisations such as those that can be generated with geostatistics. Moreover, the models obtained do not have the resolution required for modelling at reservoir scale. This limits the applicability of forward stratigraphic models for modelling reservoirs. However they could be used in combination with other geostatistical methods. For instance, two-point statistics could be computed on a forward stratigraphic Earth model and then used to constrain a geostatistical simulation with Pluri-Gaussian Simulations. The contacts between facies in the forward stratigraphic Earth model could also help to define the truncation rule for the Pluri-Gaussian Simulations. Alternatively, a hierarchical or nested approach could be taken to reservoir modelling, in which a forward stratigraphic method could be used to model facies associations, and facies could then be modelled within these facies associations with a geostatistical method.

The work carried out here on pdfs of facies thicknesses has given interesting results for carbonate strata. Burgess (2008) has shown that around thirty percent of carbonate facies thickness distributions could be modelled by the exponential pdf. This means that in most cases, it might be more appropriate to use other pdfs. As the exponential pdf is related to the exponential variogram (Matheron, 1968), Earth modellers should also use other variogram models. For instance, as mentioned above, new transiogram models with hole-effects were derived from Gamma pdfs (Appendix A), creating facies rhythmicity. The Gamma pdf has not been used

previously to characterize facies successions, and this result suggests that it could be appropriate for carbonate facies successions. For further understanding of this relation, geologists and Earth modellers would need to compute thickness pdfs and experimental variograms in vertical facies successions. This approach would help in defining new variogram models for modelling carbonate reservoirs.

This research also focused on another important feature of carbonate reservoirs, diagenesis. Diagenetic facies geometries in three dimensions are often poorly constrained, but the relationships between depositional and diagenetic facies are often known, which makes Pluri-Gaussian Simulations a valid tool to model them. The method of Renard et al. (2008) provides a good basis to model diagenesis because of its flexibility. However, most case studies using the method do not show the details of the fit between experimental and model transiograms (Chapter 2). Here, I have studied in detail cross-transiograms between depositional and diagenetic facies, which ensures that their spatial relationships are modelled. Earth modellers are encouraged to compute these cross-transiograms between diagenetic and depositional facies in vertical successions in carbonate strata because they can highlight some specific relationships and ordering between depositional and diagenetic facies. The method developed here, the shifted bi-PGS, is able to reproduce such ordering between depositional and diagenetic facies, by using a spatial shift between depositional and diagenetic facies fields. This has proved to be effective to model syn-depositional diagenesis by fitting the experimental transiograms in the Latemar carbonate platform dataset.

Overall, carbonate successions presenting facies rhythmicity, cyclicity, or diagenesis are properly modelled by the method developed in this thesis, the Shifted PGS. This is also true for siliciclastic successions exhibiting similar properties. Although the method has been tested here on the modelling of outcrops, it should also obviously be used to model hydrocarbon reservoirs. Outcrops provide vertical facies successions and so do reservoir wells. The main difference is that for outcrops, the lateral extent of facies is available through cross-sections and is used to infer the parameters of the method. For reservoirs, such information might not be available directly but can potentially be retrieved from analogues.

7.3 Markov Chains Transiograms or Shifted Pluri-Gaussian Simulations?

For all the reasons mentioned above, shifted PGS appears to be a very promising method for modelling hydrocarbon reservoirs. However, I have shown in several examples that the method was not always able to reproduce exactly the experimental facies transiograms. This is true for the transiogram oscillations, but also their tangent at the origin, characterizing among other aspects facies cyclicity. This means that shifted PGS are not always able to capture facies cyclicity, especially when a high number of facies are present. This is directly due to the number of facies transiograms or transition rates, which is higher than the number of parameters. As mentioned above, this could theoretically be tackled by using more complex truncation rules (Deutsch and Deutsch, 2014).

Concerning transiogram-based methods derived from Markov Chains (Carle and Fogg, 1996), the transition rates are the main parameters. They can all be fitted so that the method exactly reproduces facies mean lengths, contacts, and thus cyclicity. This is true even when a high number of facies are present. This is a great advantage of transiogram-based methods derived from Markov Chains, especially if vertical facies successions are the main data type constraining the reservoir, and Earth modellers can simply reproduce observed facies transition rates. However, as already discussed, Markov Chain transiograms are limited at incorporating other geological notions such as non Waltherian Earth models, rhythmicity or diagenesis.

Thanks to the research developed here, PGS are now also able to model cyclicity using the spatial shift. PGS have also the possibility to use complex covariances, which results in complex transiograms. For instance, I have used here stable covariances, which can create facies models with fractal behaviour (Chiles and Delfiner, 2012). Covariances can also be summed together to create more complex models and match complex hole-effects (Mosser et al., 2018). Moreover, I have shown that using shifts with lateral components could create progradational or retrogradational facies geometries, and honour Walther's law, as with transiograms derived from Markov Chains. However, while Markov Chain transiograms necessarily honour Walther's

law, Pluri-Gaussian Simulations have more flexibility and can model different transition probabilities between facies laterally and vertically. Shifted PGS can also be made non-stationary by using an adaptive truncation rule, while Markov Chains transiograms do not easily incorporate this feature.

In terms of algorithm performance, Markov Chain transiograms can be simulated with different methods. Carle and Fogg (1996) use a co-SIS, which requires the inversion of a covariance matrix and is not efficient. On the other hand, PGS are simulated here using a fast spectral grid-free method (Shinozuka, 1971). Usually, conditioning PGS can be complex because it is composed of two steps, Gibbs sampling and kriging (Freulon and de Fouquet, 1993), but here, these steps are optimized with the screening properties of separable covariances.

Another advantage of the approach presented here is its capability to model several superimposed facies fields. This allows PGS to represent diagenesis with much flexibility because diagenetic facies can be independent from depositional facies. Although this could in theory be possible with Markov Chains transiograms, it has not yet been demonstrated.

Overall, I would conclude that shifted PGS can incorporate much more geological conceptual knowledge of the reservoir and can also reproduce the facies transiograms, as shown in this thesis. However, if the number of facies is very high and the conceptual model of the reservoir is poorly defined, it might be best to use Markov Chain transiograms and fit the facies transition rates. Earth modellers can also group facies together or use a nested approach, by first simulating facies associations with shifted PGS and then simulating facies within each facies association. If facies cut across facies associations boundaries, shifted bi-PGS could also be used to model in parallel facies and facies associations, in the same way that shifted bi-PGS model in parallel depositional and diagenetic facies.

Chapter 8

Conclusion

The geostatistical research presented in this thesis broadens the spectrum of geological concepts that can be incorporated in facies Earth models. The methods developed here are well suited for modelling carbonate reservoirs, but can also be applied to siliciclastic shallow-marine reservoirs. First, it is noted that previous geostatistical methods do not model facies cyclicity and rhythmicity although these notions are extensively observed and interpreted by geologists. In fact, these notions are not even part of the vocabulary of geostatisticians. In order to fill this gap, I first propose a quantification of facies cyclicity and facies rhythmicity based on a two-point statistical tool, the transiogram. Then, in order to reproduce these patterns in facies Earth models, I develop a new geostatistical method based on Pluri-Gaussian Simulations. The method is then extended to model diagenesis.

Facies cyclicity is defined as a facies ordering and facies rhythmicity as a repetition of facies at stratigraphic intervals of more or less constant thickness. For the quantification of these patterns, facies transiograms are used. If a vertical facies succession is cyclic, the tangents at the origin of the transiograms are different in an upward direction from a downward direction, which is also called asymmetry. Rhythmicity is controlled by oscillations of transiograms, called hole-effects. This is confirmed by the derivation of new hole-effect transiogram models from vertical facies successions thickness probability density functions (pdfs) with low coefficients of variation.

Cyclicity is then modelled by developing a novel Pluri-Gaussian Simulation method that uses a spatial shift between the Gaussian random functions. The spatial shift combined with the linear model of co-regionalization gives much flexibility in the resulting facies transiograms. The experimental transiograms of vertical facies successions can thus be fitted appropriately by the method. The shift can also be defined with a lateral component, which creates lateral cyclicity and progradational or retrogradational facies architectures that honour Walther's law. Rhythmicity is modelled with the method by building new separable covariance models with vertical hole-effects. The hole-effect covariance is a product of a Gaussian covariance and a cosine function, which gives much flexibility in fitting hole-effects of experimental transiograms. Because rhythmicity is not commonly observed laterally, the three dimensional covariance is usually not periodic in lateral directions. Gaussian random functions with such covariances are simulated with a spectral method and the conditioning to facies data is optimized thanks to the screening properties of the separable covariance model.

Diagenesis is modelled by adding a third dimension to the truncation rule of the PGS. This novel approach allows the incorporation of another facies classification for diagenetic facies, which can be independent from depositional facies. The third Gaussian random function can also be correlated to the two others, which is convenient for modelling syn-depositional diagenesis, or kept independent from them, which is more appropriate for modelling post-depositional, fracture-related diagenesis. Moreover, shifts are also used with the third Gaussian random function, which allows the Earth modeller to create an ordering between depositional and diagenetic facies. This also gives more flexibility for fitting the experimental cross-transiograms between depositional and diagenetic facies.

The geostatistical developments are applied to a variety of case studies. The main one is based on outcrop data from the Latemar carbonate platform (Italy), in the Upper Cyclic Facies interval, which features cyclicity and rhythmicity represented in the experimental transiograms computed in vertical facies successions at Cimon Forcellone and Cimon Latemar. These are accurately fitted by the proposed method, which is then used to build corresponding Earth models. This outcrop dataset also displays syn-depositional and post-depositional diagenesis, which are also modelled. The siliciclastic Upper Cretaceous Spring Canyon Member of the

Blackhawk Formation, which is exposed in the Book Cliffs (Utah) is also modelled with the method. It contains a proximal-to-distal facies trend resulting in non-stationary facies proportions. In this case, data quantification is performed with embedded transition rates which are less influenced by non-stationarity while the latter is modelled with an adaptive truncation rule. The method is thus well suited to be incorporated in workflows for predicting resource recovery of shallow-marine subsurface reservoirs.

Bibliography

Adams EW, Grotzinger JP, Watters WA, Schrder S, McCormick DS, Al-Siyabi HA (2005) Digital characterization of thrombolite-stromatolite reef distribution in a carbonate ramp system (terminal Proterozoic, Nama Group, Namibia). AAPG bulletin 89(10):1293–1318

Aigner T, Braun S, Palermo D, Blendinger W (2007) 3d geological modelling of a carbonate shoal complex: reservoir analogue study using outcrop data. First Break p 65

Alabert F (1989) Non-Gaussian data expansion in the earth sciences. Terra Nova 1(2):123–134

Alabert F, Modot V (1992) Stochastic models of reservoir heterogeneity: Impact on connectivity and average permeabilities. In: SPE Annual Technical Conference and Exhibition, 4-7 October, Washington, D.C, Society of Petroleum Engineers

Allard D, D'or D, Froidevaux R (2011) An efficient maximum entropy approach for categorical variable prediction. European Journal of Soil Science 62(3):381–393

Amour F, Mutti M, Christ N, Immenhauser A, Agar SM, Benson GS, Tomás S, Alway R, Kabiri L (2012) Capturing and modelling metre-scale spatial facies heterogeneity in a Jurassic ramp setting (Central High Atlas, Morocco). Sedimentology 59(4):1158–1189

Apanasovich TV, Genton MG (2010) Cross-covariance functions for multivariate random fields based on latent dimensions. Biometrika 97(1):15–30

Armstrong M (1992) Positive definiteness is not enough. Mathematical geology 24(1):135–143

Armstrong M, Galli A, Beucher H, Loc'h G, Renard D, Doligez B, Eschard R, Geffroy F (2011) PluriGaussian simulations in geosciences. Berlin, Springer Science & Business Media

Astrakova A, Oliver DS, Lantuéjoul C (2015) Truncation map estimation based on bivariate probabilities and validation for the truncated pluriGaussian model. arXiv preprint arXiv:150801090

Barbier M, Hamon Y, Doligez B, Callot JP, Floquet M, Daniel JM (2012) Stochastic joint simulation of facies and diagenesis: a case study on early diagenesis of the Madison Formation (Wyoming, USA). Oil & Gas Science and Technology–Revue dIFP Energies nouvelles 67(1):123–145

Bartok P, Reijers T, Juhasz I (1981) Lower Cretaceous Cogollo Group, Maracaibo Basin, Venezuela: sedimentology, diagenesis, and petrophysics. AAPG Bulletin 65(6):1110–1134

Bathurst RG (1972) Carbonate sediments and their diagenesis, developments in sedimentology, vol 12. Elsevier

Beckert J, Vandeginste V, John CM (2015) Exploring the geological features and processes that control the shape and internal fabrics of late diagenetic dolomite bodies (Lower Khuff equivalent–Central Oman Mountains). Marine and Petroleum Geology 68:325–340

Beucher H, Renard D (2016) Truncated Gaussian and derived methods. Comptes Rendus Geoscience 348(7):510–519

Braun S (2003) Quantitative analysis of carbonate sandbodies: outcrop analog study from an epicontinental basin (Triassic Germany), URL `http://agris.fao.org/agris-search/search.do?recordID=AV20120118005`, universität Tübingen

Burgess P, Wright V, Emery D (2001) Numerical forward modelling of peritidal carbonate parasequence development: implications for outcrop interpretation. Basin Research 13(1):1–16

Burgess PM (2008) The nature of shallow-water carbonate lithofacies thickness distributions. Geology 36(3):235–238

Burgess PM (2016) Identifying ordered strata: Evidence, methods, and meaning. Journal of Sedimentary Research 86(3):148–167

Carle SF, Fogg GE (1996) Transition probability-based indicator geostatistics. Mathematical geology 28(4):453–476

Carle SF, Fogg GE (1997) Modeling spatial variability with one and multidimensional continuous-lag Markov Chains. Mathematical Geology 29(7):891–918

Carrera MFL, Barbier M, Le Ravalec M (2018) Accounting for diagenesis overprint in carbonate reservoirs using parametrization technique and optimization workflow for production data matching. Journal of Petroleum Exploration and Production Technology pp 1–15

Carrillat A, Sharma SK, Grossmann T, Iskenova G, Friedel T, et al. (2010) Geomodeling of giant carbonate oilfields with a new multipoint statistics workflow. In: Abu Dhabi International Petroleum Exhibition and Conference, Society of Petroleum Engineers

Catuneanu O, Galloway WE, Kendall CGSC, Miall AD, Posamentier HW, Strasser A, Tucker ME (2011) Sequence stratigraphy: methodology and nomenclature. Newsletters on stratigraphy 44(3):173–245

Chiles JP, Delfiner P (2012) Geostatistics: modeling spatial uncertainty, vol 497. John Wiley & Sons, Hoboken

Cisne JL (1986) Earthquakes recorded stratigraphically on carbonate platforms. Nature 323(6086):320

Davies GR, Smith Jr LB (2006) Structurally controlled hydrothermal dolomite reservoir facies: An overview. AAPG bulletin 90(11):1641–1690

De Boer P, Wonders A (1984) Astronomically induced rhythmic bedding in Cretaceous pelagic sediments near Moria (Italy). Milankovitch and climate pp 177–190

Desassis N, Renard D, Beucher H, Petiteau S, Freulon X (2015) A pairwise likelihood approach for the empirical estimation of the underlying variograms in the pluriGaussian models. arXiv preprint arXiv:151002668

Deutsch C, Tran T (2002) Fluvsim: a program for object-based stochastic modeling of fluvial depositional systems. Computers & Geosciences 28(4):525–535

Deutsch JL, Deutsch CV (2014) A multidimensional scaling approach to enforce reproduction of transition probabilities in truncated pluriGaussian simulation. Stochastic environmental research and risk assessment 28(3):707–716

Doligez B, Hamon Y, Barbier M, Nader F, Lerat O, Beucher H, et al. (2011) Advanced workflows for joint modelling of sedimentological facies and diagenetic properties. impact on reservoir quality. In: SPE Annual Technical Conference and Exhibition, Society of Petroleum Engineers

D'Or D, Allard D, Biver P, Froidevaux R, Walgenwitz A (2008) Simulating categorical random fields using the multinomial regression approach. In: Geostats 2008 proceedings of the eighth international geostatistics congress, vol 1, pp 59–68

D'Or D, David E, Walgenwitz A, Pluyaud P, Allard D (2017) Non stationary pluriGaussian simulations with auto-adaptative truncation diagrams using the cart algorithm. In: 79th EAGE Conference and Exhibition 2017

Doveton JH (1994) Theory and applications of vertical variability measures from Markov Chain analysis. AAPG Special Volumes

Dubrule O (1983) Cross validation of kriging in a unique neighborhood. Journal of the International Association for Mathematical Geology 15(6):687–699

Dubrule O (2017) Indicator variogram models: Do we have much choice? Mathematical Geosciences 49(4):441–465

Dunham RJ (1962) Classification of carbonate rocks according to depositional textures. AAPG Special Volumes

Egenhoff SO, Peterhänsel A, Bechstädt T, Zühlke R, Grötsch J (1999) Facies architecture of an isolated carbonate platform: tracing the cycles of the Latemar (Middle Triassic, northern Italy). Sedimentology 46(5):893–912

Emery X (2010) On the existence of mosaic and indicator random fields with spherical, circular, and triangular variograms. Mathematical Geosciences 42(8):969–984

Emery X, Lantuéjoul C (2006) Tbsim: A computer program for conditional simulation of three-dimensional Gaussian random fields via the turning bands method. Computers & Geosciences 32(10):1615–1628

Emery X, Arroyo D, Peláez M (2014) Simulating large Gaussian random vectors subject to inequality constraints by Gibbs sampling. Mathematical Geosciences 46(3):265–283

Fisher A (1964) The Lofer cyclothems of the alpine Triassic. Bulletin Kansas Geological Survey 169:107–149

Freulon X, de Fouquet C (1993) Conditioning a Gaussian model with inequalities. In: Geostatistics Troia '92, Springer, pp 201–212

Galli A, Le Loch G, Geffroy F, Eschard R (2006) An application of the truncated pluri-Gaussian method for modeling geology. AAPG Special Volumes

Gari J (2008) Développements en géologie numérique d'affleurement et modélisation stratigraphique 3d: exemple de la marge carbonatée du bassin sud-provençal au crétacé supérieur (se, france). PhD thesis, Aix-Marseille 1

Genz A (1992) Numerical computation of multivariate normal probabilities. Journal of computational and graphical statistics 1(2):141–149

Genz A, Bretz F, Miwa T, Mi X, Leisch F, Scheipl F, Hothorn T (2019) mvtnorm: multivariate normal and t distributions. URL `https://CRAN.R-project.org/package=mvtnorm`, r package version 1.0-7

Gingerich PD (1969) Markov analysis of cyclic alluvial sediments. Journal of sedimentary research 39(1)

Ginsburg RN (1957) Early diagenesis and lithification of shallow-water carbonate sediments in south Florida. Special Publications of SEPM 5

Gneiting T, Kleiber W, Schlather M (2010) Matérn cross-covariance functions for multivariate random fields. Journal of the American Statistical Association 105(491):1167–1177

Goldhammer R, Dunn P, Hardie L (1990) Depositional cycles, composite sea-level changes, cycle stacking patterns, and the hierarchy of stratigraphic forcing: examples from Alpine Triassic platform carbonates. Geological Society of America Bulletin 102(5):535–562

Goldhammer R, Lehmann P, Dunn P (1993) The origin of high-frequency platform carbonate cycles and third-order sequences (Lower Ordovician El Paso Gp, west Texas): constraints from outcrop data and stratigraphic modeling. Journal of Sedimentary Research 63(3)

Grotzinger JP (1986a) Cyclicity and paleoenvironmental dynamics, Rocknest platform, northwest Canada. Geological Society of America Bulletin 97(10):1208–1231

Grotzinger JP (1986b) Evolution of Early Proterozoic passive-margin carbonate platform, Rocknest Formation, Wopmay orogen, Northwest Territories, Canada. Journal of Sedimentary Research 56(6)

Hamon Y, Deschamps R, Joseph P, Doligez B, Schmitz J, Lerat O (2016) Integrated workflow for characterizing and modeling a mixed sedimentary system: The Ilerdian Alveolina Limestone Formation (Graus–Tremp Basin, Spain). Comptes Rendus Geoscience 348(7):520–530

Hampson GJ, Storms JE (2003) Geomorphological and sequence stratigraphic variability in wave-dominated, shoreface-shelf parasequences. Sedimentology 50(4):667–701

Harris PM (1994) Satellite images of carbonate depositional settings: Examples of reservoir-and exploration-scale geologic facies variation. 11, Amer Assn of Petroleum Geologists

Hattori I (1976) Entropy in Markov Chains and discrimination of cyclic patterns in lithologic successions. Journal of the International Association for Mathematical Geology 8(4):477–497

Herbert TD, Fischer AG (1986) Milankovitch climatic origin of mid-Cretaceous black shale rhythms in central Italy. Nature 321(6072):739

Hinnov LA, Goldhammer RK (1991) Spectral analysis of the Middle Triassic Latemar limestone. Journal of Sedimentary Research 61(7)

Hönig MR, John CM (2015) Sedimentological and isotopic heterogeneities within a Jurassic carbonate ramp (UAE) and implications for reservoirs in the Middle East. Marine and Petroleum Geology 68:240–257

House MR (1985) A new approach to an absolute timescale from measurements of orbital cycles and sedimentary microrhythms. Nature 315(6022):721

Jacquemyn C, El Desouky H, Hunt D, Casini G, Swennen R (2014) Dolomitization of the Latemar platform: Fluid flow and dolomite evolution. Marine and Petroleum Geology 55:43–67

Jacquemyn C, Huysmans M, Hunt D, Casini G, Swennen R (2015) Multi-scale three-dimensional distribution of fracture-and igneous intrusion-controlled hydrothermal dolomite from digital outcrop model, Latemar platform, Dolomites, northern Italy. AAPG Bulletin 99(5):957–984

Janson X, Madriz DD (2012) Geomodelling of carbonate mounds using two-point and multi-point statistics. Geological Society, London, Special Publications 370(1):229–246

Johnson NM, Dreiss SJ (1989) Hydrostratigraphic interpretation using indicator geostatistics. Water Resources Research 25(12):2501–2510

Jones TA, Ma YZ (2001) Teacher's aide: geologic characteristics of hole-effect variograms calculated from lithology-indicator variables. Mathematical Geology 33(5):615–629

Jordan Jr CF (1973) Carbonate facies and sedimentation of patch reefs off Bermuda. AAPG Bulletin 57(1):42–54

Journel A, Froidevaux R (1982) Anisotropic hole-effect modeling. Mathematical Geology 14(3):217–239

Jung A, Aigner T (2012) Carbonate geobodies: hierarchical classification and database–a new workflow for 3d reservoir modelling. Journal of Petroleum Geology 35(1):49–65

Jung A, Aigner T, Palermo D, Nardon S, Pontiggia M (2012) A new workflow for carbonate reservoir modelling based on mps: shoal bodies in outcrop analogues (Triassic, sw Germany). Geological Society, London, Special Publications 370(1):277–293

Kamola DL, Huntoon JE (1995) Repetitive stratal patterns in a foreland basin sandstone and their possible tectonic significance. Geology 23(2):177–180

Kendall M OJ Stuart A (1994) Vol. 1: Distribution theory. Arnold, London

Kenter J, Harris P, Collins J, Weber L, Kuanysheva G, Fischer D (2006) Late Visean to Bashkirian platform cyclicity in the central Tengiz buildup, Precaspian Basin, Kazakhstan: Depositional evolution and reservoir development. AAPG Special Volumes

Koehrer BS, Heymann C, Prousa F, Aigner T (2010) Multiple-scale facies and reservoir quality variations within a dolomite body–outcrop analog study from the Middle Triassic, sw German Basin. Marine and Petroleum Geology 27(2):386–411

Koltermann CE, Gorelick SM (1996) Heterogeneity in sedimentary deposits: A review of structure-imitating, process-imitating, and descriptive approaches. Water Resources Research 32(9):2617–2658

Krumbein WC, Dacey MF (1969) Markov Chains and embedded Markov Chains in geology. Journal of the International Association for Mathematical Geology 1(1):79–96

Lakzaie A, Ghasemalaskari MK, Vaziri M, et al. (2009) Reservoir facies modeling using intelligent data gathering in an iranian carbonate field. In: EUROPEC/EAGE Conference and Exhibition, Society of Petroleum Engineers

Langlais V, Beucher H, Renard D (2008) In the shade of the truncated Gaussian simulation. In: Proceedings of the eighth international geostatistics congress, Santiago, Chile, pp 799–808

Lantuéjoul C (1994) Non conditional simulation of stationary isotropic multiGaussian random functions. In: Geostatistical Simulations, Springer, pp 147–177

Lantuéjoul C (2002) Geostatistical simulation: models and algorithms. Springer Science & Business Media

Larsen AL, Ulvmoen M, Omre H, Buland A (2006) Bayesian lithology/fluid prediction and simulation on the basis of a Markov-Chain prior model. Geophysics 71(5):R69–R78

Le Blévec T, Dubrule O, John CM, Hampson GJ (2016) Building more realistic 3-d facies indicator models. In: SPE (ed) International Petroleum Technology Conference, Bangkok, Thailand

Le Blévec T, Dubrule O, Hampson G, John C (2017a) Towards a better understanding of the facies indicator variogram. In: 79th EAGE Conference and Exhibition 2017

Le Blévec T, Dubrule O, John CM, Hampson GJ (2017b) Modelling asymmetrical facies successions using pluri-Gaussian simulations. In: Geostatistics Valencia 2016, Springer, pp 59–75

Le Blévec T, Dubrule O, John CM, Hampson GJ (2018) Geostatistical modelling of cyclic and rhythmic facies architectures. Mathematical Geosciences URL `https://doi.org/10.1007/s11004-018-9737-y`

Le Blévec T, Dubrule O, John CM, Hampson GJ (in review) Earth modelling of cyclic depositional facies and diagenesis facies architectures. AAPG Bulletin

Li B, Zhang H (2011) An approach to modeling asymmetric multivariate spatial covariance structures. Journal of Multivariate Analysis 102(10):1445–1453

Li W (2007) Markov Chain random fields for estimation of categorical variables. Mathematical Geology 39(3):321–335

Lindsay RF, Cantrell DL, Hughes GW, Keith TH, Mueller III HW, Russell SD (2006) Ghawar Arab-D reservoir: widespread porosity in shoaling-upward carbonate cycles, Saudi Arabia. AAPG Special Volumes

Ma YZ, Jones TA (2001) Teacher's aide: Modeling hole-effect variograms of lithology-indicator variables. Mathematical Geology 33(5):631–648

Ma YZ, Seto A, Gomez E (2009) Depositional facies analysis and modeling of the Judy Creek reef complex of the Upper Devonian Swan Hills, Alberta, Canada. AAPG bulletin 93(9):1235–1256

Maharaja A (2008) Tigenerator: object-based training image generator. Computers & Geosciences 34(12):1753–1761

Maleki M, Emery X, Cáceres A, Ribeiro D, Cunha E (2016) Quantifying the uncertainty in the spatial layout of rock type domains in an iron ore deposit. Computational Geosciences 20(5):1013–1028

Masetti D, Neri C, Bosellini A (1991) Deep-water asymmetric cycles and progradation of carbonate platforms governed by high-frequency eustatic oscillations (Triassic of the Dolomites, Italy). Geology 19(4):336–339

Matérn B (1986) Spatial variation, volume 36 of Lecture Notes in Statistics. Springer-Verlag, Berlin

Matheron G (1968) Processus de renouvellement purs. Course document Ecole des Mines de Paris

Matheron G (1989) The internal consistency of models in geostatistics. In: Quantitative Geology and Geostatistics, Springer, pp 21–38

Matheron G, Beucher H, de Fouquet C, Galli A, Ravenne C (1988) Simulation conditionnelle à trois faciès dans une falaise de la formation du Brent. Sciences de la Terre, Série Informatique Géologique 28:213–249

Middleton GV (1973) Johannes Walther's law of the correlation of facies. Geological Society of America Bulletin 84(3):979–988

Moore CH (2001) Carbonate reservoirs: porosity, evolution and diagenesis in a sequence stratigraphic framework, vol 55. Elsevier

Mosser L, Le Blvec T, Dubrule O (2018) Reconstruction of three-dimensional porous media: Statistical or deep learning approach? In: Statistical data science, pp 125–139

Obermaier M, Ritzmann N, Aigner T (2015) Multi-level stratigraphic heterogeneities in a Triassic shoal grainstone, Oman Mountains, Sultanate of Oman: Layer-cake or shingles? GeoArabia 20(2):115–142

Oliver DS (2003) Gaussian cosimulation: modelling of the cross-covariance. Mathematical Geology 35(6):681–698

Omre H (1987) Bayesian kriging-Merging observations and qualified guesses in kriging. Mathematical Geology 19(1):25–39

Palermo D, Aigner T, Nardon S, Blendinger W (2010) Three-dimensional facies modeling of carbonate sand bodies: Outcrop analog study in an epicontinental basin (Triassic, southwest Germany). AAPG bulletin 94(4):475–512

Parks KP, Bentley LR, Crowe AS (2000) Capturing geological realism in stochastic simulations of rock systems with Markov statistics and simulated annealing. Journal of Sedimentary Research 70(4):803–813

Parquer MN, Collon P, Caumon G (2017) Reconstruction of channelized systems through a conditioned reverse migration method. Mathematical Geosciences 49(8):965–994

Peterhänsel A, Egenhoff SO (2008) Lateral variabilities of cycle stacking patterns in the Latemar, Triassic, Italian Dolomites. SEPM Spec Publ 89:217–229

Philip J (1993) Late Cretaceous carbonate-siliciclastic platforms of provence, southeastern france. Memoirs-American Association of Petroleum Geologists pp 375–375

Pontiggia M, Ortenzi A, Ruvo L, et al. (2010) New integrated approach for diagenesis characterization and simulation. In: North Africa Technical Conference and Exhibition, Society of Petroleum Engineers

Pratt BR, James NP (1986) The St George Group (Lower Ordovician) of western Newfoundland: tidal flat island model for carbonate sedimentation in shallow epeiric seas. Sedimentology 33(3):313–343

Preto N, Hinnov LA, Hardie LA, De Zanche V (2001) Middle Triassic orbital signature recorded in the shallow-marine Latemar carbonate buildup (Dolomites, Italy). Geology 29(12):1123–1126

Purkis S, Vlaswinkel B, Gracias N (2012) Vertical-to-lateral transitions among Cretaceous carbonate facies, a means to 3-d framework construction via Markov analysis. Journal of Sedimentary Research 82(4):232–243

Pyrcz MJ, Deutsch CV (2014) Geostatistical reservoir modeling. Oxford, Oxford university press

Qi L, Carr TR, Goldstein RH (2007) Geostatistical three-dimensional modeling of oolite shoals, St. Louis Limestone, southwest Kansas. AAPG bulletin 91(1):69–96

Rameil N (2008) Early diagenetic dolomitization and dedolomitization of Late Jurassic and earliest Cretaceous platform carbonates: a case study from the Jura Mountains (NW Switzerland, E France). Sedimentary Geology 212(1-4):70–85

Read J, Goldhammer R (1988) Use of Fischer plots to define third-order sea-level curves in Ordovician peritidal cyclic carbonates, Appalachians. Geology 16(10):895–899

Renard D, Beucher H (2012) 3d representations of a uranium roll-front deposit. Applied Earth Science 121(2):84–88

Renard D, Beucher H, Doligez B (2008) Heterotopic bi-categorical variables in pluriGaussian truncated simulations. In: Proceedings of the Eighth International Geostatistics Congress Geostats, Citeseer, pp 289–298

Renard D, Bez N, Desassis N, Beucher H, Ors F, Laporte F (2015) Rgeostats: The geostatistical package [version: 11.0. 3]. mines paristech

Ruf M, Aigner T (2004) Facies and poroperm characteristics of a carbonate shoal (Muschelkalk, South German Basin): a reservoir analogue investigation. Journal of Petroleum Geology 27(3):215–239

Ruiu J, Caumon G, Viseur S (2016) Modeling channel forms and related sedimentary objects using a boundary representation based on non-uniform rational b-splines. Mathematical Geosciences 48(3):259–284

Schlumberger (2018) Carbonate reservoirs. URL `https://www.slb.com/services/technical_challenges/carbonates.aspx`, 2018-06-01

Sena CM, John CM (2013) Impact of dynamic sedimentation on facies heterogeneities in Lower Cretaceous peritidal deposits of central east oman. Sedimentology 60(5):1156–1183

Shamshad A, Bawadi M, Hussin WW, Majid T, Sanusi S (2005) First and second order Markov Chain models for synthetic generation of wind speed time series. Energy 30(5):693–708

Sharp I, Gillespie P, Morsalnezhad D, Taberner C, Karpuz R, Vergés J, Horbury A, Pickard N, Garland J, Hunt D (2010) Stratigraphic architecture and fracture-controlled dolomitization of the Cretaceous Khami and Bangestan groups: an outcrop case study, Zagros Mountains, Iran. Geological Society, London, Special Publications 329(1):343–396

Shinozuka M (1971) Simulation of multivariate and multidimensional random processes. The Journal of the Acoustical Society of America 49(1B):357–368

Smith Jr LB (2006) Origin and reservoir characteristics of Upper Ordovician Trenton–Black River hydrothermal dolomite reservoirs in New York. AAPG bulletin 90(11):1691–1718

Strasser A (1988) Shallowing-upward sequences in Purbeckian peritidal carbonates (lowermost Cretaceous, Swiss and French Jura Mountains). Sedimentology 35(3):369–383

Strebelle S (2002) Conditional simulation of complex geological structures using multiple-point statistics. Mathematical Geology 34(1):1–21

Taylor KG, Gawthorpe RL, Fannon-Howell S (2004) Basin-scale diagenetic alteration of shoreface sandstones in the Upper Cretaceous Spring Canyon and Aberdeen Members, Blackhawk Formation, Book Cliffs, Utah. Sedimentary Geology 172(1-2):99–115

Taylor TR, Giles MR, Hathon LA, Diggs TN, Braunsdorf NR, Birbiglia GV, Kittridge MG, Macaulay CI, Espejo IS (2010) Sandstone diagenesis and reservoir quality prediction: Models, myths, and reality. AAPG bulletin 94(8):1093–1132

Tucker M (1985) Shallow-marine carbonate facies and facies models. Geological Society, London, Special Publications 18(1):147–169

Tucker ME, Wright VP (2009) Carbonate sedimentology. John Wiley & Sons

Van Wagoner JC, Mitchum R, Campion K, Rahmanian V (1990) Siliciclastic sequence stratigraphy in well logs, cores, and outcrops: concepts for high-resolution correlation of time and facies. AAPG methods in exploration series, 0743-0531 ; no 7

Vandeginste V, John CM, van de Flierdt T, Cosgrove JW (2013) Linking process, dimension, texture, and geochemistry in dolomite geobodies: A case study from Wadi Mistal (northern Oman) linking process, dimension, texture, and geochemistry in dolomite geobodies. AAPG bulletin 97(7):1181–1207

Venables WN, Ripley BD (2013) Modern applied statistics with S-PLUS. Springer Science & Business Media

Verrill AE (1907) The Bermuda islands. part 4, geology and paleontology. Trans Connecticut Academy Arts Sciences 12:316

Wackernagel H (2003) Multivariate geostatistics: an introduction with applications. Springer Science & Business Media

Wang L, Wong P, Shibli S, et al. (1998) Modelling porosity distribution in the A'nan Oilfield: Use of geological quantification, neural networks and geostatistics. In: SPE International Oil and Gas Conference and Exhibition in China, Society of Petroleum Engineers

Warrlich G, Bosence D, Waltham D, Wood C, Boylan A, Badenas B (2008) 3d stratigraphic forward modelling for analysis and prediction of carbonate platform stratigraphies in exploration and production. Marine and Petroleum Geology 25(1):35–58

White CD, Novakovic D, Dutton SP, Willis BJ (2003) A geostatistical model for calcite concretions in sandstone. Mathematical Geology 35(5):549–575

Wilkinson BH, Drummond CN, Rothman ED, Diedrich NW (1997) Stratal order in peritidal carbonate sequences. Journal of Sedimentary research 67(6)

Wilson JL (2012) Carbonate facies in geologic history. Springer Science & Business Media

Appendix A

Understanding Hole-Effects, Link Between Indicator Covariance and Thickness pdf

In this appendix, I relate facies thickness probability density functions (pdfs) with corresponding indicator covariances. The aim is to understand how thickness pdfs' produce indicator covariances with hole-effects. The relation is developed using the theory of renewal processes (Matheron, 1968), in the particular case of two facies alternating with each other along a direction, with independent thickness pdfs. Under this assumption, Matheron (1968) derives the following expression

$$\chi(\lambda) = \frac{p\ (1-p)}{\lambda} - \frac{1}{m_0 + m_1} \frac{(1-\Phi_0(\lambda))(1-\Phi_1(\lambda))}{\lambda^2(1-\Phi_0(\lambda)\Phi_1(\lambda))}. \tag{A.1}$$

$\chi(\lambda)$ is the Laplace transform of the indicator covariance model, p is the proportion of the first facies, $(1-p)$ is the proportion of the second facies, m_0 and m_1 are respectively the two facies mean thicknesses, and $\Phi_0(\lambda)$ and $\Phi_1(\lambda)$ the Laplace transform of their thickness pdfs. In this appendix, I consider facies with the same thickness pdf $\Phi(\lambda)$ (Laplace transform), and thus

same mean length m, and proportions $p = 1 - p = 1/2$, giving

$$\chi(\lambda) = \frac{1}{4\ \lambda} - \frac{1}{2m}\ \frac{(1-\Phi(\lambda))^2}{\lambda^2(1-\Phi(\lambda)^2)}. \tag{A.2}$$

Applying the inverse Laplace transform to this expression gives a covariance model corresponding to the chosen thickness pdf. As shown by Matheron (1968), if an exponential pdf with mean a is used for the thickness pdf, this formula results in an exponential covariance $c(h)$ for the facies

$$c(h) = \frac{1}{4}\ \exp\Big(-\frac{2h}{a}\Big) \tag{A.3}$$

This is the classic exponential covariance model that can be derived from Markov Chains (Carle and Fogg, 1996) and is used widely with SIS. An exponential distribution is also a Gamma distribution

$$g_k(x) = \frac{1}{\Gamma(k)\ a^k}\ x^{k-1}\ e^{-\frac{x}{a}} \tag{A.4}$$

of order $k = 1$ and coefficient of variation $1/\sqrt{k} = 1$. Thus, exponential covariances are associated with thickness pdfs which have a coefficient of variation equal to 1. Matheron (1968) shows that if the order of the Gamma distribution is 2 for the thickness pdf, the inverse Laplace transform of Eq. (A.2) results in the covariance model

$$c(h) = \frac{1}{4}\ \exp\Big(-\frac{h}{a}\Big)\ \cos\Big(\frac{h}{a}\Big), \tag{A.5}$$

which is pseudo-periodic. However, as the corresponding oscillations attenuate strongly, it is not called hole-effect. It still suggests that by decreasing the coefficient of variation ($k = 1/\sqrt{2}$), pseudo-periodicity arises. In order to confirm this conjecture, I apply the inverse Laplace transform to Eq. (A.2) with Gamma distributions of increasing order (and thus decreasing coefficient of variation). For a Gamma distribution of order 3, I obtain the covariance model

$$c(h) = \frac{1}{36}\ \left(\exp\Big(-\frac{2h}{a}\Big) + 8\ \exp\Big(-\frac{2h}{a}\Big)\ \cos\Big(\frac{\sqrt{3}h}{2a}\Big)\right), \tag{A.6}$$

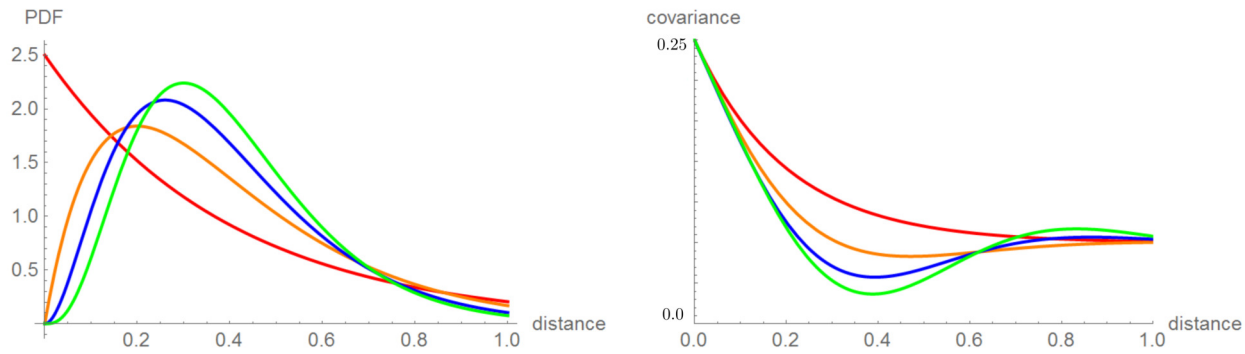

Figure A.1: Facies thickness pdf (left) and corresponding covariances (right) using Eq. (A.2). Each curve corresponds to a different covariance model, red is Eq. (A.3), orange is Eq. (A.5), blue is Eq. (A.6), and green is Eq. (A.7).

and for a Gamma distribution of order 4, I obtain the covariance

$$c(h) = \frac{1}{8}\, e^{-\frac{h}{a}}\, \cos\left(\frac{h}{\sqrt{2}a}\right)\left(2\cosh\left(\frac{h}{\sqrt{2}a}\right) + \sqrt{2}\sinh\left(\frac{h}{\sqrt{2}a}\right)\right). \tag{A.7}$$

Figure A.1 shows that these covariances have a more pronounced hole-effect. Moreover, Fig. A.1 highlights that as the coefficient of variation decreases (the pdf are more skewed), the corresponding covariance hole-effect increases. This helps understand the hole-effect: a lower variability of facies thicknesses creates oscillations of the covariances.

The functions of Eq. A.6 and Eq. A.7 are new one dimensional indicator covariance models. They show that hole-effects result from a reduction in coefficient of variations of facies thicknesses. The hole-effect thus characterizes facies rhythmicity: repetition of facies at interval of thicknesses with low variations.